Development of a Self-Heating Consolidation Procedure for 3D-Printed Continuous Wire Polymer Composite Laminates

Thomas John Barbuio

A Thesis Submitted to the Faculty of Graduate Studies in Partial Fulfillment of the Requirements for the Degree of Master of Applied Science

Graduate Program in Mechanical Engineering

Lassonde School of Engineering

York University

Toronto, Ontario, Canada

NOVEMBER 2025

Abstract

The voids in 3D-printed continuous wire polymer composites (CWPCs) reduce the wire-polymer adhesion, which can decrease their strength and stiffness and their in-part sensing accuracy. This thesis shows the development, implementation and effects of a consolidation procedure to reduce the voids in unidirectional and cross-ply 3D-printed CWPC laminates. The consolidation procedure used resistive heating combined with hot-pressing to reduce the internal voids. Image processing of sample cross sections proved the void content in consolidated samples were 91.6% lower compared to unprocessed, while flexural tests found 5% and 12% higher flexural strength and stiffness respectively. Next, the effects of the consolidation procedure were tested on the uniaxial tensile properties of unidirectional and cross-ply 3D-printed CWPC samples, showing promising results for transverse reinforced CWPC samples. The results of the two studies performed showed that the consolidation procedure significantly reduces the void content of the samples, and thus positively impacts the mechanical properties.

Dedication

To Nonna Maria, Nonno Guglielmo, Nonno Giovanni (“con i baffi”), and Nonna Ada.

“Never Tell Me The Odds” — Han Solo

Leigh Brackett & Lawrence Kasdan, *Star Wars: The Empire Strikes Back*

Acknowledgements

Firstly, I would like to thank my supervisors, Dr. Garrett Melenka and Dr. Roger Kempers, for whom I am grateful for giving me this opportunity and the chance to work on such an interesting project. to begin with. Their combined supervision and support allowed me the opportunity to gain technical skills in a variety of fields and intellectually grow in a way I did not know I could.

Thank you to the Lassonde mechanical engineering department's graduate program coordinator, technicians, and staff for all of their help on the day-to-days during my time.

Thank you to my past and present lab mates from both the Melenka Lab and TF Lab, whose drive, knowledge, and positive attitude were inspiring to be around. The opportunities for learning, collaboration, and research discussions where everyone brought their respective expertise was incredibly rewarding. I am honoured to have been a part of such great teams for the last two years. A specific thank you to Calvin, Shauvik, Tak, Tristan, for the many late nights and weekends in the lab and the dinners at Shoeless Joe's. Your impact on this journey remains to this day.

Thank you to my Mom, who taught me to always strive to be the best version of myself, my Dad, who taught me that hard work and a can-do attitude goes a longer way than you can realize, and my sister, who had infectious positivity throughout the process. Thank you all for believing in me.

Table of Contents

List of Figures

List of Tables

List of Abbreviations

AFT	Additive Fusion Technology
AFP	Automated Fibre Placement
Al	Aluminum
AM	Additive Manufacturing
ANOVA	Analysis of Variance
ATL	Automated Tape Layering
CAD	Computer-Aided Design
CF	Carbon Fibre
CFRPC	Continuous Fibre-Reinforced Polymer Composite
CLPT	Classical Laminate Plate Theory
Cu	Copper
CWPC	Continuous Wire Polymer Composite
DIC	Digital Image Correlation
DISC	Discrete In-Situ Consolidation
DSC	Differential Scanning Calorimetry
FDM	Fused Deposition Modelling
FEA	Finite Element Analysis
FFF	Fused Filament Fabrication
FOV	Field of View
fps	Frames Per Second
F_{vf}	Fibre Volume Fraction

HIP	Hot Isostatic Pressing
MWCNT	Multiwalled Carbon Nanotube
PA12	Polyamide 12
PEEK	Poly Ether Ether Ketone
PEKK	Poly Ether Ketone Ketone
PETG	Polyethylene Terephthalate Glycol
PLA	Polylactic Acid
PPS	Polyphenylene Sulfide
ROI	Region of Interest
SLA	Stereolithography
STL	Standard Triangle Language
TPU	Thermoplastic Polyurethane
UTM	Universal Testing Machine
UTS	Ultimate Tensile Strength
V_{vf}	Void Volume Fraction
W_{vf}	Wire Volume Fraction

List of Variables

Q	Thermal Energy Output
R	Resistance
T	Time
V	Applied Voltage
T_0	Desired Temperature of Sample's Centre
T_i	Initial Temperature of Sample's Centre
T_{platen}	Temperature of Aluminum Platen
Bi	Biot Number
τ	Fourier Number
L_s	Length of Sample's Edge to Sample's Centre
α	Thermal Diffusivity
C_p	Specific Heat Capacity of Composite
m	Mass of Sample
Q_{platen}	Thermal Energy From the Platen Through the Sample by Conduction
P_{RH}	Electrical Power by Resistive Heating
A_s	Cross-Sectional Area of Sample
A_w	Area of Wires in Sample's Cross-Section
A_v	Area of Voids in Sample's Cross-Section
l_s	Nominal Length of Sample
l_w	Measured Length of Wire
n_w	Number of Wires in Cross-Sectional Image

V_{vf}	Void Volume Fraction
W_{vf}	Wire Volume Fraction
h	Height of Sample Under Flexural Loading
I	Area Moment of Inertia
L	Length of Support Span
M	Bending Moment
y	Distance from Sample Edge to the Neutral Axis
δ	Displacement of the Point of Maximum Deflection
ε	Flexural Strain
σ	Flexural Stress
W_f	Weight Fraction
ΔH_{cc}	Enthalpy of Cold Crystallization
ΔH°_f	Theoretical Enthalpy of Fusion
ΔH_m	Enthalpy of Melting
X_C	Crystallinity of Polymer Matrix
D_w	Wire Diameter
l	Nominal Sample Length
l_w	Wire Length
t	Measured Sample Thickness
w	Measured Sample Width

Chapter 1 - Introduction

1.1. Research Motivation

Composite materials consist of two or more materials, typically a fibre and a polymer matrix, to provide a lightweight alternative to metals without compromising strength. In the early to mid 1950s, fibreglass was new and was used as a substitute for metals for vehicle bodies in the automotive and theme park industries [1], [2]. As the composite materials industry has grown, composites have been applied to other fields, with more advanced fibres such as carbon fibre replacing the use of traditional fibreglass. Current examples of composite materials include carbon fibre bicycle frames and aircraft wings [3], [4]. A challenge in the manufacturing of composite materials is to produce geometrically complex parts repeatably. Traditional techniques such as autoclave molding and hand layup have been used in industries such as aerospace and marine for reliable composite manufacturing for more than 40 years [5], [6]. While these traditional techniques are reliable and still used today, the high production costs and the limits of what geometries these composite manufacturing processes can produce hinders the application of composite materials. In line with the fourth industrial revolution, the automation of manufacturing by 3D printing is a significant step to advancing the manufacturing of materials other than polymers to a new realm of possibilities [7]. A report from 2018 expects the market for the additive manufacturing of composite materials to be higher than $9 billion by the year 2028 [8]. Therefore, the use of 3D printing to manufacture composite materials, specifically continuous fibre reinforced polymer composites, has become a heavily researched topic to better understand the use-cases and material properties of 3D-printed continuous fibre composite materials [9-11]. The 3D printing of composite materials has been achieved by several

commercial desktop and industrial-sized 3D printers [12], [13]. Typically, these printers are equipped with a dual-extrusion system, which has two separate nozzles: one for the matrix material and one for the fibre. Dual-extruder, commercial 3D printer designs allow limited choice in fibre placement. Single nozzle co-extrusion, which deposits the fibre and matrix simultaneously, allows for the placement of fibres in each raster.

Carbon fibre is commonly used in continuous fibre printing with various thermoplastic reinforcement materials such as nylon, polyetheretherketone (PEEK), and polylactic acid (PLA) [10], [11], [14]. Recent studies in literature have used metal wires as the reinforcement material in customized single nozzle co-extrusion and custom built dual-extrusion desktop 3D printers [15-18]. The introduction of a metal wire instead of a synthetic fibre such as carbon fibre has been referred to as continuous wire polymer composite (CWPC) 3D printing. The 3D printing of CWPCs has introduced the implementation of properties such as strain sensing with a continuous copper wire for structural health monitoring, and resistive heating of a continuous nickel-chromium wire for composite panel de-icing [16], [19].

However, it is noted across the literature that significant void content is found, particularly surrounding the continuous wire, decreasing the wire-polymer adhesion, and therefore decreasing the mechanical properties and sensing accuracy. Voids cause internal stress concentrations, leading to cracks within the parts which will lead to premature failure. As such, void reduction is an important concept in composite manufacturing, as the presence of voids can be detrimental to composite material performance. In traditional composite manufacturing, voids are often reduced during composite manufacturing, typically by applying heat and pressure to fill in void content, such as in compression molding and automated fibre placement (AFP). Studies have reduced the voids present in 3D-printed polymer composites in a number of ways, both

during printing and in post-processing techniques with varying success [20], [21]. Regardless of the technique, the fundamental concept is the same for semi-crystalline polymers. The polymer is heated above its glass transition, where it is viscous and can be re-molded, but below its actual melting point and pressure is applied fill in the voids. This heating has been performed externally, through either conduction or convection depending on the method, but the presence of the continuous wire allows an opportunity to use the reinforcement wire itself to uniformly reheat the polymers matrix.

There is also a lack of understanding of the effects of perpendicular or alternating lamina orientations on the mechanical properties of CWPCs, as most studies only print the rasters unidirectionally, parallel to the direction of loading. Composite materials are non-homogenous, anisotropic materials. This means the mechanical performance of the material is dependant on the layup of the reinforcement material. When a composite material is going to experience loads in one direction only, it is suitable to lay up the reinforcement material unidirectionally. However, this is infrequently the case. Composites are used in applications which often undergo combined loading, or loading from multiple directions, so the reinforcement orientations is often varied layer-by-layer to accommodate for combined loading. A basic example of this is a cross-ply, where the orientation of the direction of the fibres in each lamina alternates between 0° (parallel) and 90° (perpendicular).

1.2. Thesis Objectives

The objectives of this thesis are to determine the material strength of CWPCs as a result of reduced void content and to determine the material strength of multidirectional CWPC laminates to increase their applications. To reduce the void content, a consolidation procedure was

developed which utilized hot-pressing using instrumented aluminum platens and resistive heating of the continuous reinforcement wire. The effects of this consolidation procedure were determined using optical microscopy and image processing to quantify the change in void volume fraction, while three-point flexural testing quantified the change in the flexural strength and stiffness. The next objective was achieved by 3D printing unidirectional in the 0° and 90° directions, and cross-ply CWPC laminates. The uniaxial tensile properties were found for both consolidated and non-consolidated samples of each layup configuration. The elastic modulus from testing for both consolidated and non-consolidated samples were compared to the apparent laminate stiffness calculated using classical laminate plate theory to show the samples where voids were reduced were closer to the analytical laminate stiffness.

1.3. Thesis Outline

This thesis consists of 5 chapters and an appendix section. Chapter 2 provides a review of the literature, which outlines the fundamental understandings of composite manufacturing, specifically 3D printing and void reduction techniques used in traditional composite manufacturing methods, the 3D printing of CWPCs and the void content observed in the literature, void reduction techniques on 3D-printed polymer and polymer composite parts, and their effectiveness. Resistive heating and its applications are also outlined.

The focus of Chapter 3 is on the initial development of the consolidation procedure for void reduction and its effects on flexural properties was studied. Analytical modelling of the sample heating was performed to determine the consolidation parameters. Unidirectional CWPC samples were 3D printed for three-point flexural testing using PLA as the matrix, nickel-chromium (NiCr) as the continuous wire reinforcement. Optical microscope images and

image processing tools were used to quantify the V_{vf} of unprocessed, hot-pressed and consolidated samples to determine the improvements of void reduction due to the uniform internal heating of the samples by Joule heating. The flexural strength and flexural modulus of unprocessed, hot-pressed and consolidated samples were compared using statistical analysis. Chapter 3 is currently under review with the peer-reviewed journal "Journal of Composite Materials" as "Self-Heating Consolidation Method for 3D-Printed Continuous Wire Polymer Composites".

The focus of Chapter 4 is on the tensile testing of unidirectional and cross-ply CWPC laminates. CWPCs were 3D printed with the same materials used in Chapter 3. A new consolidation rig was custom built to improved on the shortcomings of the one used previously for repeatability and reliability. Each laminate layup configuration was consolidated to determine the effects of consolidation on the mechanical properties. Uniaxial tensile testing was performed paired with digital image correlation (DIC) to determine the mechanical properties of the layup configurations, and the effectiveness of the consolidation procedure on different layup configurations. Classical laminate plate theory calculations for the apparent laminate stiffness were compared to the experimental results for the elastic modulus. Optical microscopy is also used to view the void content of non-consolidated and consolidated samples of each layup configuration. Appendix A shows the process for building the consolidation setup used in Chapter 4. Chapter 4 will be submitted to a peer-reviewed journal as "Mechanical Properties of Cross-Ply and Unidirectional 3D-Printed Continuous Wire Polymer Composites".

Chapter 5 outlines the conclusions found from the previous two chapters by discussing the overlaps and the potential areas of application. It then discusses future work and potential areas

of expansion for future research including higher melt temperature polymer materials and stronger fibre materials or ways to improve the consolidation procedure.

1.4. References

[1] “Corvette Body Materials - - Vette Magazine.” Accessed: Aug. 05, 2025. [Online]. Available: https://www.motortrend.com/how-to/vemp-1108-corvette-body-materials

[2] “Celebrating 55 Years of Disneyland With Dumbo the Flying Elephant.” Accessed: Aug. 05, 2025. [Online]. Available: https://www.smithsonianmag.com/smithsonian-institution/celebrating-55-years-of-disneyland-with-dumbo-the-flying-elephant-66710/

[3] “BRIDGE Bike Works - North American Made Carbon Bikes.” Accessed: Apr. 10, 2025. [Online]. Available: https://www.bridgebikeworks.com/?srsltid=AfmBOooGmSIqeN3Xs5nZ3i--cSoqyUU0mTdPyih2Fd55vLA_hRSR1nV_

[4] “Composites: Airbus continues to shape the future | Airbus.” Accessed: Apr. 10, 2025. [Online]. Available: https://www.airbus.com/en/newsroom/news/2017-08-composites-airbus-continues-to-shape-the-future

[5] K. Balasubramanian, M. T. H. Sultan, and N. Rajeswari, “Manufacturing techniques of composites for aerospace applications,” in Sustainable Composites for Aerospace Applications, Elsevier, 2018, pp. 55–67. doi: 10.1016/B978-0-08-102131-6.00004-9.

[6] J. Summerscales, “Composites manufacturing for marine structures,” in Marine Applications of Advanced Fibre-Reinforced Composites, Elsevier Inc., 2016, pp. 19–55. doi: 10.1016/B978-1-78242-250-1.00002-8.

[7] U. M. Dilberoglu, B. Gharehpapagh, U. Yaman, and M. Dolen, “The Role of Additive Manufacturing in the Era of Industry 4.0,” Procedia Manuf, vol. 11, pp. 545–554, Jan. 2017, doi: 10.1016/J.PROMFG.2017.07.148.

[8] “Composites Additive Manufacturing Market To Surpass $9 Billion in 2028.” Accessed: Aug. 27, 2025. [Online]. Available: https://additivemanufacturingresearch.com/news/composites-additive-manufacturing-market/

[9] G. W. Melenka, B. K. O. Cheung, J. S. Schofield, M. R. Dawson, and J. P. Carey, “Evaluation and prediction of the tensile properties of continuous fiber-reinforced 3D printed structures,” Compos Struct, 2016, doi: 10.1016/j.compstruct.2016.07.018.

[10] N. van de Werken, P. Koirala, J. Ghorbani, D. Doyle, and M. Tehrani, “Investigating the hot isostatic pressing of an additively manufactured continuous carbon fiber reinforced PEEK composite,” Addit Manuf, vol. 37, p. 101634, 2021, doi: 10.1016/j.addma.2020.101634.

[11] M. A. Saleh, S. Olcun, M. Karam, R. Kempers, and G. W. Melenka, “High stiffness 3D-printed continuous pitch carbon fiber reinforced polymer composites,” J Compos Mater, vol. 58, no. 16, pp. 1873–1886, Jul. 2024, doi: 10.1177/00219983241249526.

[12] “Industrial Additive Manufacturing Platform | Markforged.” Accessed: Jan. 22, 2025. [Online]. Available: https://markforged.com/

[13] “Anisoprint - Continuous fiber 3D printing for manufacturing of optimal composites.” Accessed: Jan. 22, 2025. [Online]. Available: https://anisoprint.com/

[14] I. Zhilyaev et al., “Experimental and numerical analysis of the consolidation process for additive manufactured continuous carbon fiber-reinforced polyamide 12 composites,” Front Mater, vol. 9, Dec. 2022, doi: 10.3389/fmats.2022.1068261.

[15] Y. Ibrahim, G. W. Melenka, and R. Kempers, “Fabrication and tensile testing of 3D printed continuous wire polymer composites,” Rapid Prototyp J, vol. 24, no. 7, pp. 1131–1141, Oct. 2018, doi: 10.1108/RPJ-11-2017-0222.

[16] M. A. Saleh, R. Kempers, and G. W. Melenka, “A comparative study on the electromechanical properties of 3D-Printed rigid and flexible continuous wire polymer composites for structural health monitoring,” Sensors and Actuators A, vol. 328, p. 112764, 2021, doi: 10.1016/j.sna.2021.112764.

[17] C. Thompson, C. González, and J. LLorca, “Material extrusion fabrication of continuous metal wire-reinforced polymer–matrix composites,” Composites Communications, vol. 50, p. 102024, Oct. 2024, doi: 10.1016/J.COCO.2024.102024.

[18] Á. García de la Camacha, J. Sánchez del Río, and J. LLorca, “Additive manufacturing of quasi-isotropic wire-reinforced metal-polymer composite laminates,” Rapid Prototyp J, vol. 31, no. 7, pp. 1449–1460, 2025, doi: 10.1108/RPJ-11-2024-0467.

[19] Y. Ibrahim, R. Kempers, and A. Amirfazli, “3D printed electro-thermal anti-or de-icing system for composite panels,” Cold Reg Sci Technol, 2019, doi: 10.1016/j.coldregions.2019.102844.

[20] Y. Asano, M. Ueda, M. Yamawaki, R. Matsuzaki, A. Le Duigou, and M. Castro, “Layer-wise compaction 3D printing: void reduction and interfacial enhancement for continuous carbon fiber–reinforced thermoplastics,” Advanced Composite Materials, pp. 1–15, Feb. 2025, doi: 10.1080/09243046.2025.2459672.

[21] N. Elderfield and J. C. H. Wong, “Discrete in-situ consolidation of additively manufactured continuous fiber-reinforced polymer composites,” Compos Part A Appl Sci Manuf, vol. 171, Aug. 2023, doi: 10.1016/j.compositesa.2023.107562.

Chapter 2 - Literature Review

2.1. Introduction

3D printing has rapidly changed the manufacturing industry since its conception by Hideo Kodama in 1981 [1]. In 1983, stereolithography (SLA) was created, and the patent for SLA 3D printing was filed the following year [2]. Later, in 1989, fused deposition modeling (FDM) technology was first patented by Stratasys Ltd. [3]. 3D printing has gained popularity in several industries from aerospace to dentistry [4], [5]. 3D printing will continue to grow as the technology improves, because of its adaptability to accommodate printing many different materials with vastly different properties for a variety of applications, including rechargeable lithium metal batteries, corneal tissue, and concrete for houses [6-8]. Desktop 3D printing using fused filament fabrication (FFF) technology has found a large market with hobbyists and commercial users, with an expected growth of $21 billion by 2030 [9]. Reasons for the growth in desktop FFF 3D printing specifically has to do with affordability of the printers themselves, low cost and versatility of filament materials, ease of use, and space-saving it provides.

Composite materials have been used to manufacture many different parts and structures including aircraft wings, bicycle frames, and concrete reinforced with steel rebar due to their high strength to weight ratio [10-12]. Composite materials consist of a reinforcement material and a matrix material, with thermoset polymers such as epoxy typically used as the matrix. Traditional composite manufacturing technologies include hand lay-up, autoclave molding, and vacuum bagging. These techniques can be costly, time-consuming, and constrain the geometry of parts. This has led to a research focus on composite material additive manufacturing (AM), including technologies such as automated fibre placement (AFP) and 3D printing. The 3D

printing of composite materials can be complex but allows for the automated manufacturing of parts that traditional composite manufacturing techniques could not and also allows for different reinforcement and matrix materials to be used, with companies such as Markforged and Anisoprint manufacturing 3D printers that can print continuous fibres [13], [14]. Composite manufacturing techniques typically involve a process to reduce the voids, as voids can decrease the mechanical properties of composite materials significantly [15]. Recent research has focused on the 3D printing of continuous wire polymer composites (CWPCs) which use a thermoplastic matrix material and a continuous metal wire as the reinforcement. While these continuous metal wires in the 3D-printed samples offer significant improvements in the mechanical properties of the 3D-printed parts as expected, the presence of voids in CWPCs are an issue that have yet to be addressed.

The aim of this work is to develop and implement a consolidation procedure, which combines the basic principles of hot-pressing and the Joule effect, or resistive heating. The developed procedure is performed to quantify the void reduction, then determine the mechanical properties on 3D-printed CWPC samples. The implementation of resistive heating on the continuous wire in the samples is used for void reduction in this work, however it has other applications such as external surface heating, higher temperature matrix curing with low power, and shape memory behaviour. This chapter will focus on the background knowledge of important topics to this work including 3D printing technologies, composite manufacturing, research on CWPCs, and the effectiveness of different void reduction techniques used on 3D-printed polymer and 3D-printed composite parts.

2.2. Fundamentals of FFF 3D Printing

3D printing is the term used to describe additive manufacturing (AM) processes that deposit a material layer-by-layer onto a build plate [16]. Arguably the most common type of 3D printing, FFF, typically starts from a computer aided design (CAD) model, which is saved as a standard triangle language (STL) file, then put into a slicing software. The slicing software then outputs a GCode for the printer to read, which dictates movements required to fabricate each layer of the solid model. While a slicing software provides multiple options for print orientation, infill, and other print settings, custom GCode may be required when specific raster orientation or non-planar printing is required [17].

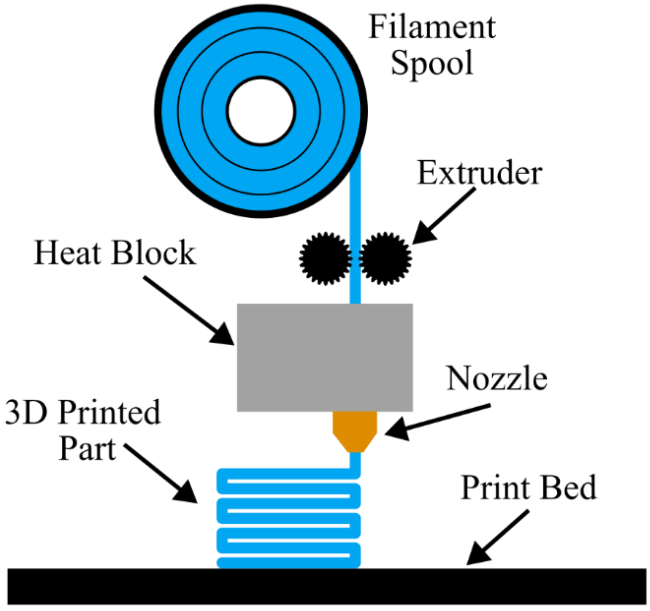

Figure 2-1: 3D printing working principles of fused filament fabrication showing the filament fed into the heat block to deposit the molten polymer onto the print bed

FFF 3D printing uses spools of thermoplastic filament materials. Thermoplastics with relatively low printing temperatures, such as polylactic acid (PLA) can be printed around 180-220°C in open desktop 3D printers easily. While higher printing-temperature thermoplastics such as

polyetheretherketone (PEEK) which typically prints around 390-450°C [18], require enclosures for temperature control to successfully 3D print. FFF printing uses an extruder to feed the filament into a heat block, which heats the polymer to its melting temperature. The molten filament in the heat block is extruded through the nozzle onto a print bed, where the deposited polymer rasters are then rapidly cooled. The print head moves in a specific pattern layer-by-layer to make the final part (Figure 2-1). FFF 3D printing is a simple and cost-effective method to manufacture thermoplastic parts. However, printing parameters such as build orientation and extrusion rate can affect mechanical properties of printed parts [19]. Another shortcoming is FFF 3D printing results in voids between rasters and lower resolution of final products (Figure 2-2). These are caused by the rapid cooling of the filament during printing and nozzle sizes used, which typically range from 0.2 – 1.0 mm. This makes FFF 3D printing most suited to rapid prototyping and relatively low-strength polymer parts.

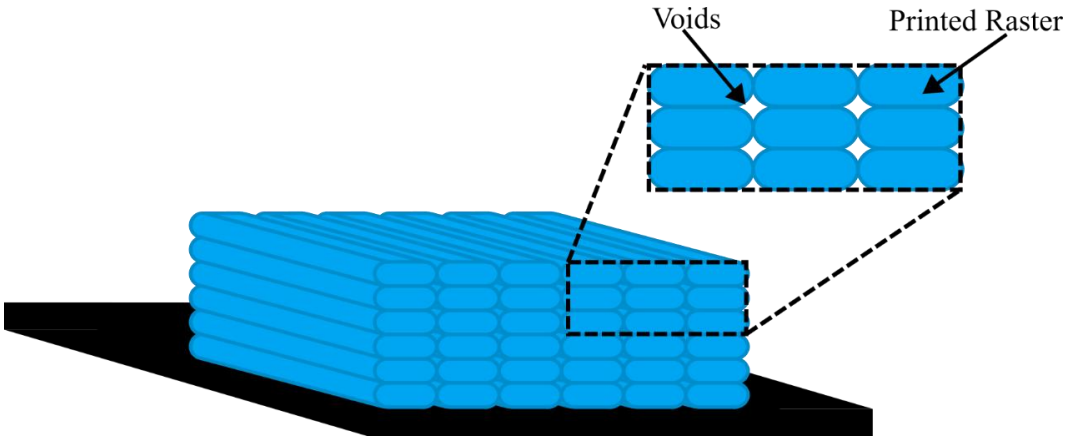

Figure 2-2: Close-up view of a portion of the cross-section of a 3D-printed object showing the voids that form between rasters due to the nature of the FFF 3D printing process

2.3. Composite Materials and Manufacturing

Composite materials are used in various industries, often replacing metal parts where component strength needs to remain, but the overall weight of the system needs to be reduced, due to their

high strength-to-weight ratios [20], [21]. A composite material is a heterogeneous material that comprises of two or more materials used together to optimize the benefits of each. Composites typically consist of a reinforcement material such as a synthetic or natural fibre, such as carbon, glass, aramid, jute, and coir fibres, and a binding matrix material such as an epoxy or thermoplastic polymer to bond the loose fibres and make a functional part. The reinforcement fibres in composites are classified as continuous or discontinuous, and their alignment can have a significant effect on the strength of the component. Short fibres are often randomly oriented and are used for low strength parts under combined loading. Their discontinuity causes the stress distribution within the composite part to be distributed to the matrix material more than continuous fibre composites. Continuous fibres are aligned in a specific pattern to meet the loading conditions based on the application, they can be unidirectional in specific load cases, or they can be laid up in different directions, which stack to make a multidirectional laminate. Figure 2-3 shows a visual representation of a variety of discontinuous and continuous fibre alignments.

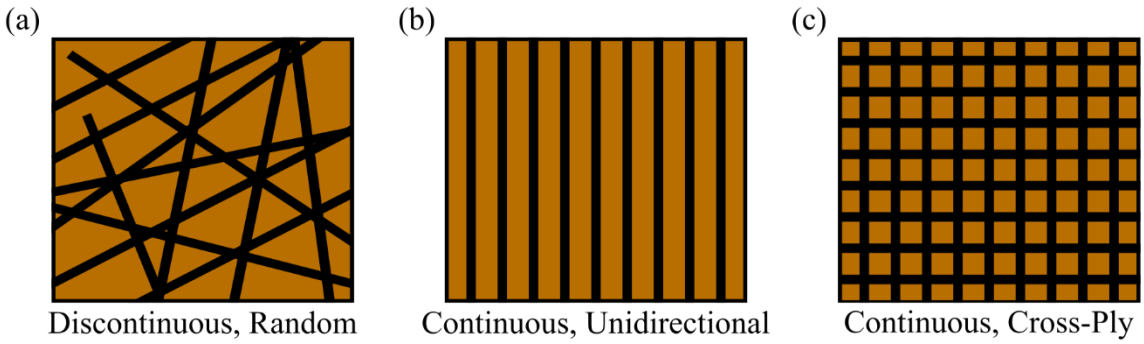

Figure 2-3: Comparison of fibre alignment showcasing (a) discontinuous fibres randomly aligned (b) continuous fibres aligned unidirectionally, and (c) continuous fibres aligned in a cross-ply

The heterogeneity of composite materials results in anisotropic nature, meaning a given composite laminate has different mechanical properties depending on the loading direction,

unlike metals for example, which are homogenous and isotropic. Therefore, the structural integrity of a composite is subject to the loading conditions, the layup and orientation of the fibres, the ratio of fibre to matrix, and the presence of porosity (voids), in the material. Voids act as stress concentrations under loading, causing cracking, delamination between the fibre and matrix, and ultimately failure of the composite part. A study by Liu *et al.* [22] found that voids can decrease the tensile and flexural strengths of carbon fibre (CF)/epoxy prepreg laminates by 14% and 22% for void content increases of 2.6% and 3.2%, respectively. Void volume fraction (V_{vf}) in composite materials should be below 1% for high precision applications such as aerospace, with other guidelines outlining below 2% or below 5% for less critical applications [23], [24].

Autoclave molding is a technique commonly used to minimize voids when manufacturing composite parts, using a heated chamber with controlled pressure. Autoclave molding has high power requirements, is time consuming, and limits the size of the parts that are able to be produced. Analytical modeling has been used to improve the autoclave molding parameters to lower costs and manufacturing time related to the manufacturing process, reducing the need for trial-and-error in autoclave composite manufacturing [25]. Other composite manufacturing methods are therefore desirable when autoclave molding is impractical. Common composite manufacturing techniques, such as compression molding and automated fibre placement, are often used instead of autoclave molding to achieve comparably low void content while having lower associated costs and manufacturing times.

2.3.1. Compression Molding

Compression molding is an out-of-autoclave process, providing a variety of options in material choice including both thermoset and thermoplastic matrix materials, and continuous or discontinuous synthetic and natural fibres [26], [27]. Custom positive and negative molds are machined for each part required to be compression molded (Figure 2-4). Pre-laid fibres and liquid matrices or prepregs are preheated to above the melting temperature (T_m) of the polymer matrix, where they are then placed in a mold above the matrix's glass transition temperature (T_g). The top mold is lowered and applies a set pressure for an allotted time based on the materials being used. Once the compression stage ends, the molds are cooled below the T_g, so the matrix is no longer in a viscous state, and the parts are removed [21]. The main compression molding parameters are temperature, pressure and molding time, which can significantly vary the mechanical properties of the part [28]. Compression molding is an effective way to manufacture composite parts at a high output. The compression molding parameters applied can yield varying void content, but it is an effective way to keep voids within the <1% - 5% V_{vf} guideline [20], [29-32].

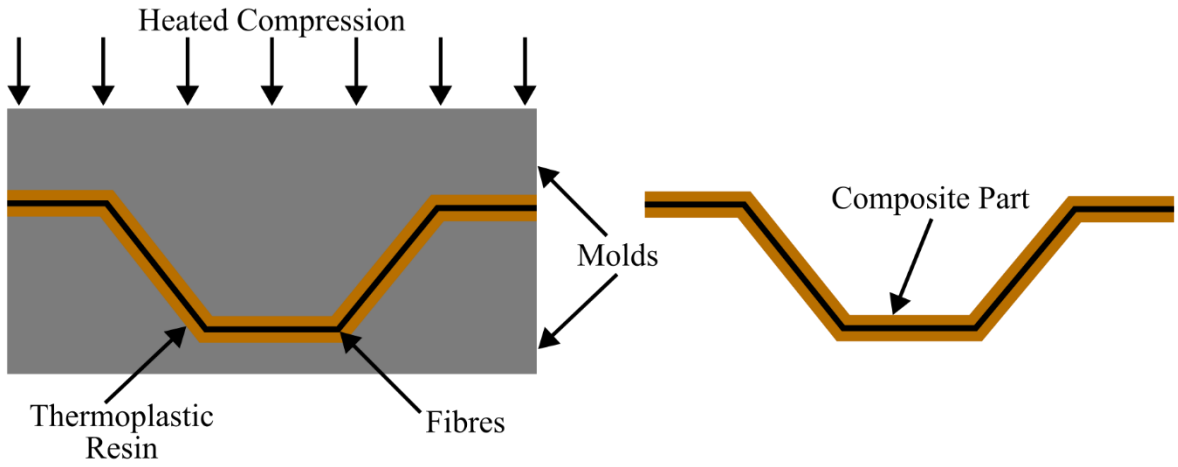

Figure 2-4: The process and working principle of compression molding for thermoplastic composite manufacturing

2.3.2. Automated Fibre Placement

Automated Fibre Placement (AFP) is an additive manufacturing method of depositing thermoset or thermoplastic matrix composite materials in a predetermined layup using a large apparatus either in a gantry format or multi-axis robotic arm [33]. Prepreg tows or tapes are fed into the system and heated using a heating element, where a compaction roller is used to consolidate the heated tows as they are deposited on the substrate (see Figure 2-5). AFP is often used to manufacture composite laminates for aerospace applications [33-35]. As such, it is required that the total void content remain below 1%. While AFP fabricates high precision laminates in a fraction of the time compared to autoclave molding, the resulting void volume fraction is highly dependant on the consolidation force and heat applied during deposition of the tows [36]. Post processing techniques have since been used to reduce voids in composite laminates manufactured by AFP, such as vacuum-bag-only or compression molding post-processing [37-40].

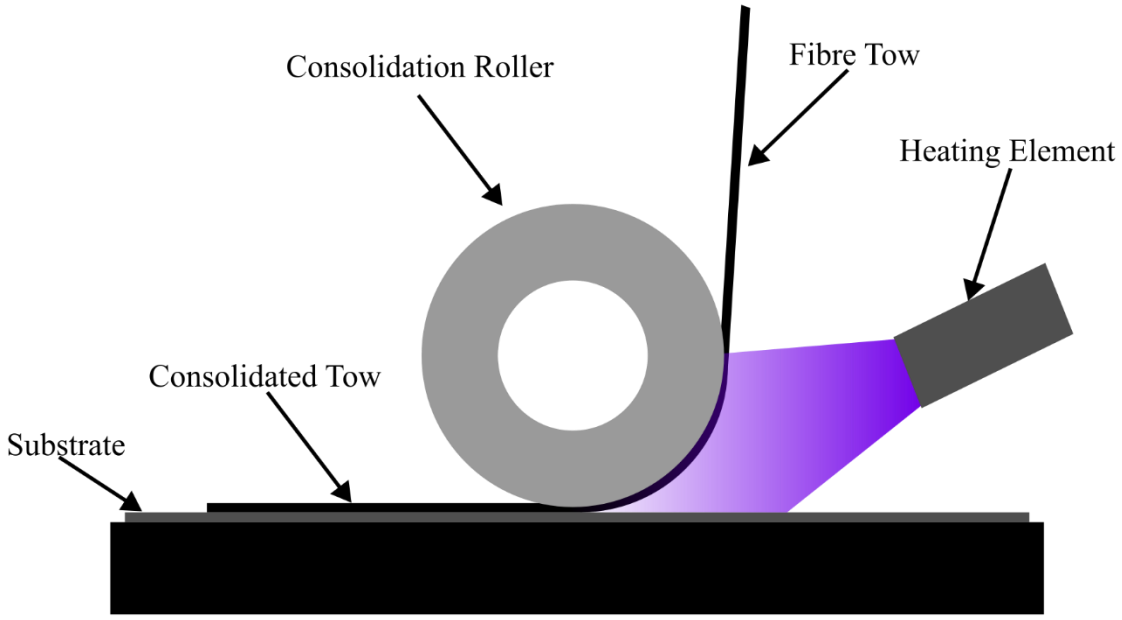

Figure 2-5: The process and working principle of AFP for additive manufacturing of composite laminates

2.4. 3D Printing of Composite Materials

Short fibres, continuous fibres, and metal powder fillers have been used to 3D print composite materials to significantly increase the strength and stiffness of regular 3D-printed thermoplastics [41-47]. Continuous fibre reinforced composite materials manufactured through more traditional methods such as hand layup and compression molding exhibit higher strength and stiffness than short fibre composites. The same applies to 3D-printed continuous fibre reinforced composite materials [48]. 3D printing allows for complex and intricate geometries to be printed, which would have been difficult to manufacture using traditional techniques [49-51]. Short fibre-reinforced filament is commercially available and can be extruded through the single nozzle of a common FFF printer, while continuous fibre 3D printing typically requires sophisticated or modified equipment. Continuous fibre composites can be 3D printed using a dual-extrusion system, where one nozzle deposits the polymer matrix, while the other deposits

the continuous fibre, which is what is typically seen in commercial continuous fibre 3D printers [43].

Co-extrusion is also possible either as dual nozzle systems or single nozzle systems. Dual nozzle systems involved separate nozzles for the reinforcement and polymer matrix, where one nozzle follows directly behind the other to deposit material directly on top. Single nozzle co-extrusion systems involve the polymer matrix and reinforcement material being fed into the same extruder and then deposited together through one nozzle. Single nozzle co-extrusion of the polymer matrix and continuous fibre materials are often more difficult due to limitations of fibre size for proper impregnation but can be done with a modified print head [52], [53].

A study by Pappas *et al.* [42] found that continuous carbon fibre reinforcement in 3D-printed continuous CF/PLA composites can increase the flexural strength of standard 3D-printed PLA samples by 52% and have a roughly 35% higher flexural strength compared to short fibre reinforced composites. They found that there were larger voids present in continuous fibre reinforced samples, due to poor fibre impregnation of the continuous fibres, causing low adhesion between the PLA matrix and the continuous carbon fibre reinforcement. Wang *et al.* [52] modeled the impregnation behaviour between the reinforcement and matrix materials. Their conducted experiments determined good fibre-matrix adhesion will increase the mechanical properties of 3D-printed composite materials. The fibre-matrix adhesion of 3D-printed composite materials can vary depending on the printing parameters and setup used to manufacture continuous fibre samples [52], [53].

Continuous carbon fibre reinforced 3D-printed composites are frequently investigated due to their superior mechanical properties [54-56]. The continuous nature of the carbon also allows for

further use cases such as shape memory behaviour composite materials, thermal properties and electronics [57-59]. Robotic arm 3D printing of continuous carbon fibre composites has also been performed in recent literature due to the expanded geometrical capabilities of the robotic arm [60-63]. Eichenhofer *et al.* [64] developed an additive manufacturing technique called "continuous lattice fabrication", to print continuous carbon fibre reinforced CF/PA12 comingled yarn material into truss structures. They use a robotic arm to print in multiple axes at one time, in order to develop truss member supported sandwich panels.

In traditional composite manufacturing techniques, the fibre layup plays a crucial role in the mechanical properties of the composite part. The orientation of the fibres in continuous fibre composites is often strategically placed depending on the expected loading conditions of the final structure. When 3D printing composite materials, this is also an incredibly important factor, as the print orientation can significantly affect the mechanical properties of the structure after printing. Fibres and rasters oriented parallel to the loading direction outperform those that are not [65], but unidirectional fibres are not always applicable as most structures experience some form of combined loading. This outlines the importance of consideration of the raster orientation when preparing the GCode in the 3D printing of composite materials [66]. Hamzah *et al.* [46] 3D printed ABS-$ZnFe_2O_4$ powder filled composite materials with 0°, 45°, and 90° raster orientations. They found that increasing the powder filler content within samples increased the tensile properties, and the highest tensile strength was achieved by 0° raster-orientated samples. Powder-filled 3D-printed composites share more similarities to short fibre composites, in that their orientation within the matrix is often random, making it difficult to properly align the reinforcement to increase the strength. However, the researchers' findings support the fact that

printed raster orientations parallel or perpendicular to the loading direction of 3D-printed objects has a significant role to play in the strength of 3D-printed specimens.

Chacón *et al.* [67] studied how varying the build orientation, layer thickness and fibre volume content effected the mechanical properties of 3D-printed composite materials. Non-reinforced nylon samples were compared with continuous carbon, glass, and Kevlar fibre reinforced nylon samples to determine the effects of printing parameters on the tensile and flexural properties. They showed that as with typical 3D-printed samples, properties like build orientation and layer thickness significantly affect both the tensile and flexural strength and stiffness of the 3D-printed continuous fibre reinforced samples. They also show that increasing the fibre volume fraction can have the most significant effect on the mechanical properties depending on the print orientation, while layer thickness had the least significant effect. The authors note the presence of voids increases when increasing the fibre volume fraction, as this can decrease the fibre-polymer bonding and the interlayer adhesion of the samples.

The presence of voids in 3D-printed composite parts also plays a significant role in the strength of the material, as the addition of fibres and raster orientation can increase the void content, ultimately hindering 3D-printed composite performance. Christ *et al.* [68] FFF 3D printed multiwalled strain sensors from a custom multiwalled carbon nanotube/thermoplastic polyurethane (MWCNT)/(TPU) filament with varying MWCNT contents. They successfully fabricated the MWCNT/TPU filament and performed tensile and cyclic loading tests to determine mechanical properties. Using micrographs, voids were observed in the 3D-printed samples compared to the extruded samples. There was a 14.4% decrease in elastic modulus in the printed results compared to the extruded samples as a result.

2.5. 3D-Printed Continuous Wire Polymer Composites

Continuous fibre 3D-printed composites provide substantial improvement to the strength and stiffness of 3D-printed parts. Some studies in literature have opted for an alternative to synthetic fibres and used a continuous wire such as copper (Cu) or nickel-chromium (NiCr) instead as the reinforcement material in FFF 3D-printed composites, referred to as continuous wire polymer composites (CWPCs). The use of a continuous metal wire reinforcement increases strength and stiffness, improves thermal properties, and allows for resistance measurement and applying a voltage to the samples for use in multiple applications. Ibrahim *et al.* [69] modified the aluminum heat block of a desktop 3D printer to have two inlets (one for the PLA matrix and one for the metal wire) and one outlet for the extruded wire-reinforced polymer raster (Figure 2-6). They printed unidirectional CWPCs with a continuous metal reinforcement wire embedded within each deposited raster as a result of the co-extrusion system. Results from Ibrahim *et al.* [70] showed that continuous NiCr wire reinforcement with a 0.7% nominal wire volume fraction (W_{vf}) increased the tensile strength of the samples by 30%. A subsequent study by Ibrahim *et al.* [71], showed a 20% increase in flexural strength when reinforcing CF-PETG with a NiCr wire, with a 1.7% W_{vf}. They then were able to show that CWPCs that reinforce PLA with copper wire improved the thermal conductivity of PLA [72]. Research in the field of continuous wire printing has since increased. Thompson *et al.* [73] and García de la Camacha *et al.* [74] used aluminum 1050 to reinforce PLA. They used a custom multi print-head 3D printer with a cutting mechanism on the continuous wire print-head to maintain continuity within each layer, while choosing which layers would be reinforced with the continuous aluminum 1050 wire. García de la Camacha *et al.* [74] noted that decreased adhesion between the wires and polymer matrix caused a 6.7% and 56.7% lower longitudinal and transverse elastic modulus than the rule of

mixtures predicted. Mishra *et al.* [75] reinforced a blend of recycled and pure ABS with a continuous brass wire using a single custom volcano nozzle. Hamidi *et al.* [76] used a continuous 0.1778 mm 302/304 stainless steel wire to reinforce dogbone PLA samples in a concentric pattern, which yielded a 69 MPa tensile strength. They then used this combined with a silicone elastomer to simulate the properties of bone in a 3D-printed joint mechanism.

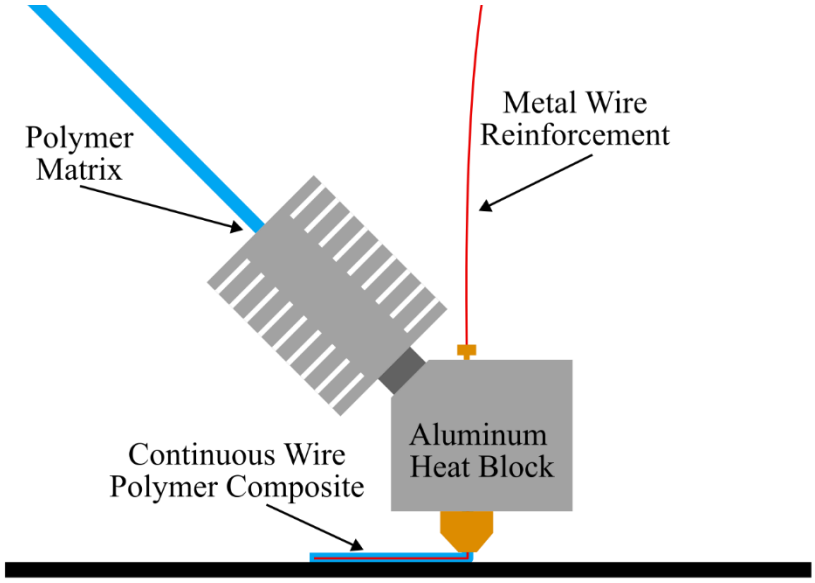

Figure 2-6: Co-extrusion of continuous wire and polymer matrix through one heat block and nozzle for the 3D printing of a CWPC raster

The reinforcement of a continuous metal wire has allowed for practical applications to be explored, aside from strengthening the parts. A scaled-up concept by Li *et al.* [77] used a 15 mm diameter nozzle to 3D print a geopolymer reinforced with a 1.2 mm diameter steel micro-cable to 3D print reinforced concrete. The resistance change within the sample, when under mechanical or thermal loads, allows for the possibility of in-part sensing. Saleh *et al.* [78-80] used copper wires to allow for in-part strain measurement for structural health monitoring applications. By monitoring the change in resistance in the sample under loading, the gauge factor was determined for the CWPC sample, with this gauge factor effectively acting as its own strain

gauge. They used Cu and NiCr as reinforcement materials and PLA and TPU as matrix materials to determine the applications of both rigid and flexible sensors. The continuous wire of the sample allows for the sensing of not only strain but also heat flux [81]. The metal wire can also be used as a heat source, where a voltage can be applied to induce resistive heating for use as de-icing panels, or for shape memory behaviour [82], [83].

A consistent issue within CWPC samples is high void content, up to 24% (Table 2-1). While the voids can be reduced by changing the size of the nozzle or changing printing parameters, co-extrusion and the introduction of the continuous metal wire results in voids embedded within the samples, mainly surrounding the wires and between rasters. The voids can result in internal stress concentrations and decreased adhesion between the polymer raster and metal wire reinforcement. This decreased adhesion between the wire and raster can decrease the accuracy in structural health monitoring and sensing applications. All CWPC studies discussed have identified voids in the samples, however none have attempted to reduce said voids to this point.

Most CWPC studies have focused on unidirectional reinforcement of the wire. However, composite materials often require lamina layups with fibres oriented in different directions to design for combined loading. Most testing of CWPCs has consisted of tensile testing, which results in only longitudinal properties. Flexural and transverse properties, however, are more heavily affected by void content within samples.

Table 2-1: Summary of different 3D-printed continuous wire polymer composites in literature and their void content

Author	Materials Used	Testing	V_{vf} %
Ibrahim *et al.* [70]	Cu/PLA, NiCr/PLA	Tensile	1.63%
Ibrahim *et al.* [71]	NiCr/PLA	Flexural	7.12%
Thompson *et al.* [73]	Al 1050/PLA	Tensile	16%, 24%
García de la Camacha *et al.* [74]	AL 1050/PLA	Tensile	0.7%, 0.8%, 1.0%
Hamidi *et al.* [76]	302/304 Stainless Steel/PLA	Tensile	22%
Saleh *et al.* [78]	Cu/PLA, NiCr/PLA	Tensile	2.01%, 2.15%
Saleh *et al.* [79]	Cu/PLA, Cu/TPU	Tensile	6.3%, 4.25%
Thompson *et al.* [84]	Mg/PLDL, Mg/PLDL-PEO	Tensile	2%, 4.1%

2.6. Effects of Voids in Polymer and Composite 3D Printing

The anisotropic behaviour in 3D-printed samples is caused by the voids that occur during the manufacturing process, which can vary in shape and size depending on the layer orientations [85-87]. Voids can be reduced by altering the printing parameters such as nozzle temperature, nozzle size, flow rate, and build orientation [19], [88], [89], though FFF 3D printing will never yield 0% void content due to the nature of the printing process. Fayazbakhsh *et al.* [90] investigated the effects of raster orientation by intentionally placing voids in 3D-printed samples. They showed that samples with no intentional defects were strongest when rasters were in the direction of loading and weakest when rasters were perpendicular to the loading direction, with mean tensile strengths of 57.7 MPa and 30.8 MPa, respectively. The intentional voids also played a significant role in the tensile strength of the 3D-printed specimens, with a 12.4% and 6.1% reduction in tensile strength and modulus for defects in the loading direction, and a 20.5% and 9.6% reduction in tensile strength and modulus for defects perpendicular to the loading direction. Their study showed that defects and raster orientation perpendicular to the direction of loading had a more significant effect on mechanical properties than those that were parallel to the

direction of loading, as the rasters were essentially being pulled apart from each other because of less effective bonding resulting from the manufacturing process of 3D printing.

The presence of voids in polymer composites can negatively affect the flexural, transverse and interlaminar shear strength, regardless of manufacturing techniques [91-93]. As the fibre material is the stronger of the two materials within a composite structure, it is typically laid up parallel to the loading direction, so it carries the majority of the load. Voids decrease the adhesion between the fibres and matrix, causing the loading distribution to the fibres to fail, resulting in the part to crack and delaminate. Fibre orientations perpendicular or at an angle relative to the loading direction, often required for combined loading applications, increase the material weakness by forcing the matrix material, the weaker of the two, to carry the majority of the load. If porosity is present within the matrix, this will act as stress concentrations and cause failure even sooner. When there is improper adhesion between the matrix and fibres, the load is not transferred to the fibres as intended, this causes internal cracking and delamination. Tang *et al.* [94] used finite element analysis (FEA) to determine up to 25% decrease in transverse and shear strength is a result of void content up to 2% for unidirectional AS24 CF composites.

3D-printed polymer composites are no different, as the introduction of fibres in the matrix during 3D printing can cause voids in the parts. This can have a negative effect on mechanical properties. While high fibre volume fraction (F_{vf}) is desirable, a higher fibre content can yield higher void content, having the opposite effect on the mechanical properties. A study by Eren *et al.* [95] 3D printed CF/Onyx samples on a Markforged Mark 2 continuous fibre FFF 3D printer. They found that samples with increased fibre volume fraction experienced lower compressive modulus and proportional limit due to a significant porosity density. While FFF 3D printing provides an opportunity to meet composite manufacturing applications that other composite AM

such as AFP and automated tape layering (ATL) can not, the voids produced as a result of the printing process hinders the technologies' potential to fill the gap. A method for void reduction is necessary in order to apply continuous fibre 3D printing to industry in a significant way.

2.7. Techniques for Void Reduction in 3D-Printed Polymer and Polymer Composite Parts

Reducing void content in 3D-printed polymer and composite parts can significantly improve the mechanical properties. As such, different consolidation techniques have been a focus in recent literature. Some processes are performed after printing and can be simple such as the annealing of 3D-printed polymer and composite samples [89], [96-98]. One study by Xiang *et al.* [96] found that heat treatment increased pores due to polymer swelling when heated, indicating annealing is more difficult to control.

Hot-pressing or compression molding after the fabrication of 3D-printed parts can also be effective in significantly removing void content while maintaining the shape and size of the 3D-printed parts [99]. Zhilyaev *et al.* [20] used the additive fusion technology (AFT) system developed by 9T Labs. In their study, the system printed multiple continuous fibre-reinforced polyamide 12 (PA12) preforms. These preforms were compression molded together using the AFT process to manufacture a helicopter door hinge. CT analysis determined the porosity in the helicopter door hinge decreased from 35% to 0.17%. A study by Valverde *et al.* [100] observed the change in thickness when performing compaction of carbon fibre-reinforced thermoplastic tapes. Compaction was performed using a custom rig to test the compaction of specimens.

Cross-ply CF/PPS (Polyphenylene Sulfide) and CF/PEEK tape layups were compacted at varying temperatures above their respective melting temperatures. Significant matrix squeeze-out

was observed as a result of compacting above the melting temperature of the thermoplastic matrices.

A study by van de Werken *et al.* [101] 3D printed 42% F_{vf} AS4C CF/PEEK samples using a 5-axis robotic arm and performed flexural, short beam shear, tensile and compression tests to compare samples that underwent hot isostatic pressing (HIP) to those that did not. Unidirectional samples were placed under HIP at various temperatures between the T_g of the PEEK matrix (143°C) and heat deflection temperature of the composite (340°C), with results showing that higher HIP temperature resulted in a larger decrease in void content. Tensile, compressive, flexural and interlaminar shear strength were all greatest when the HIP temperature was at 250°C and decreased when approaching the heat deflection temperature of the composite. In a subsequent study using FEA, Kashfi *et al.* [102] found that the flexural modulus, flexural strength and interlaminar shear strength increased most due to the 52% decrease in void content.

Some work focuses on an in-situ consolidation approach to close voids as samples are printed [103-106]. Ueda *et al.* [107] used a custom 3D printing apparatus with a built-in compaction roller for 3D compaction printing. Continuous carbon fibre compaction printed samples were compared to samples 3D printed on a continuous-fibre 3D printer. They found that compaction printing resulted in a 70% decrease in void content. This change resulted in an increase in tensile strength, flexural strength, and flexural modulus of 33%, 62% and 26%, respectively. Hot-pressed 3D-printed samples yielded comparable flexural properties to the compaction printed samples. Asano *et al.* [108] used a similar in-situ layer-wise compaction printing process and found that the flexural modulus and strength increased by 32.6% and 11.2% after voids were decreased by 8.2%.

A study by Elderfield *et al.* [109] used a custom 3D printer to manufacture CF/PA12 short beam shear samples with a discrete in-situ consolidation (DISC) technique. They compared 3D-printed, DISC 3D-printed, and 3D-printed/compression molded samples and showed that void content in the samples were 40.4%, 4.3% and 3.8% respectively. While their developed DISC procedure yielded a higher void content, they noted that voids from the compression molding were larger on average. Their processing showed that a significant decrease in void content showed a significant increase in short beam shear strength. The use of their DISC content showed promising results in 3D printing complex geometries, such as cylindrical and cylindrical lattice structures by using a mandrel as the print surface with the DISC process. The DISC process increases the use cases for 3D printing continuous carbon fibre parts by closing voids in the manufacturing process, without the part geometry restrictions from compression molding.

The studies discussed show effective void reduction techniques, with most decreasing the void content to below 5%, as desired in composite materials. Table 2-2 outlines the consolidation methods for continuous fibre 3D-printed samples used by the studies that quantified the void content before and after their respective consolidation methods.

Table 2-2: Summary of different void reduction methods and their effectiveness in reducing void content in 3D-printed continuous-reinforced composite parts

Author	Materials Used	Voids Before	Void Reduction Method	Voids After
Xiang *et al.* [96]	CF/Onyx	~15%	Annealing/ Heat-Treatment	~13%, ~19%
van de Werken *et al.* [101]	CF/PEEK	11.8%	Hot Isostatic Pressing	8%, 6.9%, 5.2%
Zhilyaev *et al.* [20]	CF/PA12	3.5%	Additive Fusion Technology	0.17%
Ueda *et al.* [107]	CF/Nylon	10%	3D-Compaction Printing	3%
Asasno *et al.* [108]	CF/Nylon	11%	3D-Compaction Printing	4.5%, 2.8%
Elderfield *et al.* [109]	CF/PA12	40.4%	DISC, Compression Molding	4.3%, 3.8%

2.8. Resistive Heating

The Joule effect is a phenomenon that occurs when heat generates as a result of an electric current passing through a resistive object. The application of this phenomenon can be referred to as Joule heating, resistance/resistive heating, and ohmic heating depending on the application [110], [111]. Resistive heating allows for fast, uniform heating at low power. The efficient self-heating it provides has made it of interest in recent studies within the composite material field. The 3D printing of composite materials allows broader potential for self-heating composites of various shapes and sizes. Recent advancements include heating of 3D-printed carbon black composites [112], [113], self-curing composite tooling [114], efficient railway vehicle heating [115], and inducing shape memory behaviour in composite parts reinforced with carbon fibres and nickel-chromium wires [116]. Resistive heating has implemented on CWPCs

in separate studies for the de-icing of composite panels, and to induce shape memory behaviour after flexural deformation [82], [83].

$$Q = \frac{V^2 t}{R} \quad \text{(Eq. 2-1)}$$

Where Q is the thermal energy output from the resistive heating, V is the voltage applied, R is the resistance across the element, and t is the resistive heating time.

A study by Reese *et al.* [117] observed a significant improvement in the manufacturing of recycled CF/PA6 textiles by applying Joule heating to reduce cycle time and power requirements of matrix curing. The V_{vf} of the Joule heating procedure with and without a vacuum were calculated using DIN EN ISO 2564 to be about 3% and 1%, respectively. To determine the effectiveness of the Joule heating method developed, flexural tests were performed according to DIN EN ISO 178. Flexural strength results of Joule heating with vacuum samples were comparable to hot-pressed samples.

A study by Cortés *et al.* [118] 3D printed a multiwalled carbon nanotube and graphene nanoplatelet-reinforced epoxy bottom layer for the de-icing of wind turbine blades. An epoxy/PCL blend was used as the top layer. They heated one sample by applying resistive heating at 30 V to the bottom layer and one using convection. After 2.9 minutes, the resistive heating had completely melted the ice, while natural convection at a 25°C room temperature had not exceeded 0°C after 20 minutes. The top epoxy/PCL layer displayed self-healing properties as it was heated. Heating efficiency of the resistive heating showed 90% efficiency from the resistive heating compared to 68% efficiency from natural convection in an oven set to 120°C.

2.9. Gaps in the Literature

The ability to 3D print composite materials has provided a new means of manufacturing with an increased potential for geometrically complex composite designs to be manufactured without costly and space consuming systems. 3D-printed continuous wire polymer composites have been used to significantly increase the strength and stiffness of 3D-printed thermoplastic materials such as PLA and TPU, with relatively low wire volume fractions. Applications of CWPCs aside from increasing strength and stiffness include in-part sensing by tracking resistance change within the reinforcement wire for structural health monitoring or heat flux sensing, inducing shape memory behaviour and de-icing through resistive heating of the continuous wire [78-83]. However, the printing process results in significant void volume fraction within the samples. Voids within these samples are in two main locations within the cross-section of the samples: at the wire-polymer interface and between polymer rasters. These voids decrease the strength and stiffness and decrease the sensing accuracy.

Current methods of consolidation of 3D-printed polymer and 3D-printed polymer composite parts focus on the heating of samples by external convection or conduction. Post processing such as annealing can cause non-uniform heating of parts or even swelling, depending on heat losses and the convective heat transfer coefficient of the system used to anneal the parts. AFT requires custom molds for each part. Requiring custom molds or custom printing apparatuses can increase the costs, while still not being applicable to certain parts with intricate designs. In-situ methods such as DISC and adding a compaction roller to a 3D printer can significantly reduce the void content as the samples are printed, but this is limited to specific geometries. Resistive heating allows for uniform in-part heating by applying a voltage across two ends of a continuous fibre

reinforcement. In CWPCs resistive heating has been used to induce shape memory behaviour and apply in-part heating for de-icing purposes.

2.10. Proposed Study

To address the gaps in the literature, the proposed study aims to develop a post-processing consolidation procedure for CWPC samples by combining the principles of hot-pressing of composite materials and resistive heating, with the goal of reducing void volume fraction to within common composite standards and increase the strength and stiffness of the samples. Chapter 3 outlines the development of this procedure and how the uniform self-heating by resistive heating improves upon external heating of the sample by conduction. Analytical models of the transient conduction and resistive heating of the CWPC samples were developed and validated. Image processing from optical microscope images were used to quantify the void volume fraction of samples that underwent no post-processing treatment, hot-pressing only and the full consolidation procedure. Three-point flexural tests were performed to determine the flexural strength and stiffness of the samples. Chapter 4 aims to characterize unidirectional samples with plies in the 0° and 90° direction, and cross-ply layup CWPC samples. The consolidation procedure was used again, with a custom built consolidation setup for better repeatability. Tensile testing was performed and DIC was used to analyze the strain fields during loading. The mechanical properties were compared to classical laminate plate theory (CLPT). Optical microscopy was performed to view longitudinal and transverse cross-sections of the samples. Through these studies, the author aims to propose a method for more effective and efficient consolidation of CWPC samples, and to characterize different layups to address the mostly unidirectional characterization in current literature. Both studies follow the goal that void

reduction or alternate layup configurations can be used to expand the use cases for CWPC printing and allow for new materials to be used.

2.11. References

[1] H. Kodama, “Automatic method for fabricating a three-dimensional plastic model with photo-hardening polymer,” Rev. Sci. Instrum, vol. 52, pp. 1770–1773, 1981, doi: 10.1063/1.1136492.

[2] “Our Story | 3D Systems.” Accessed: Apr. 13, 2025. [Online]. Available: https://www.3dsystems.com/our-story

[3] “The complete history of 3D printing - UltiMaker.” Accessed: Apr. 13, 2025. [Online]. Available: https://ultimaker.com/learn/the-complete-history-of-3d-printing/

[4] A. H. Alami et al., “Additive manufacturing in the aerospace and automotive industries: Recent trends and role in achieving sustainable development goals,” Ain Shams Engineering Journal, vol. 14, no. 11, p. 102516, Nov. 2023, doi: 10.1016/J.ASEJ.2023.102516.

[5] A. Dawood, B. M. Marti, V. Sauret-Jackson, and A. Darwood, “3D printing in dentistry,” British Dental Journal 2015 219:11, vol. 219, no. 11, pp. 521–529, Dec. 2015, doi: 10.1038/sj.bdj.2015.914.

[6] S. Zhou, I. Usman, Y. Wang, and A. Pan, “3D printing for rechargeable lithium metal batteries,” Energy Storage Mater, vol. 38, pp. 141–156, Jun. 2021, doi: 10.1016/J.ENSM.2021.02.041.

[7] A. Isaacson, S. Swioklo, and C. J. Connon, “3D bioprinting of a corneal stroma equivalent,” Exp Eye Res, vol. 173, pp. 188–193, Aug. 2018, doi: 10.1016/J.EXER.2018.05.010.

[8] “BOD2 - 3D Construction Printer | Printerra.” Accessed: Apr. 13, 2025. [Online]. Available: https://printerra.ca/bod2-3d-construction-printer/

[9] “A 3D Printer On Every Desk? Why Companies Are Buying More 3D Printers.” Accessed: Apr. 13, 2025. [Online]. Available: https://www.forbes.com/sites/carolynschwaar/2024/05/02/a-3d-printer-on-every-desk-why-companies-are-buying-more-3d-printers/

[10] “Composites: Airbus continues to shape the future | Airbus.” Accessed: Apr. 10, 2025. [Online]. Available: https://www.airbus.com/en/newsroom/news/2017-08-composites-airbus-continues-to-shape-the-future

[11] “BRIDGE Bike Works - North American Made Carbon Bikes.” Accessed: Apr. 10, 2025. [Online]. Available: https://www.bridgebikeworks.com/?srsltid=AfmBOooGmSIqeN3Xs5nZ3i--cSoqyUU0mTdPyih2Fd55vLA_hRSR1nV_

[12] P. A. Claisse, “Civil Engineering Materials,” Butterworth-Heinemann, 2016, ch. 17.

[13] “Industrial Additive Manufacturing Platform | Markforged.” Accessed: Jan. 22, 2025. [Online]. Available: https://markforged.com/

[14] “Anisoprint - Continuous fiber 3D printing for manufacturing of optimal composites.” Accessed: Jan. 22, 2025. [Online]. Available: https://anisoprint.com/

[15] I. M. Daniel and Ori. Ishai, Engineering mechanics of composite materials. Oxford University Press, 2006.

[16] M. Amran et al., “3D-printable alkali-activated concretes for building applications: A critical review,” Constr Build Mater, vol. 319, p. 126126, Feb. 2022, doi: 10.1016/J.CONBUILDMAT.2021.126126.

[17] A. Gleadall, “FullControl GCode Designer: Open-source software for unconstrained design in additive manufacturing,” Addit Manuf, vol. 46, p. 102109, Oct. 2021, doi: 10.1016/J.ADDMA.2021.102109.

[18] S. J. Park, J. E. Lee, J. Park, N. K. Lee, Y. Son, and S. H. Park, “High-temperature 3D printing of polyetheretherketone products: Perspective on industrial manufacturing applications of super engineering plastics,” Mater Des, vol. 211, p. 110163, Dec. 2021, doi: 10.1016/J.MATDES.2021.110163.

[19] J. M. Chacón, M. A. Caminero, E. García-Plaza, and P. J. Núñez, “Additive manufacturing of PLA structures using fused deposition modelling: Effect of process parameters

on mechanical properties and their optimal selection," Mater Des, vol. 124, pp. 143–157, Jun. 2017, doi: 10.1016/J.MATDES.2017.03.065.

[20] I. Zhilyaev et al., "Experimental and numerical analysis of the consolidation process for additive manufactured continuous carbon fiber-reinforced polyamide 12 composites," Front Mater, vol. 9, Dec. 2022, doi: 10.3389/fmats.2022.1068261.

[21] J. M. Lee, C. J. Lee, B. M. Kim, and D. C. Ko, "Design of prepreg compression molding for manufacturing of CFRTP B-pillar reinforcement with equivalent mechanical properties to existing steel part," International Journal of Precision Engineering and Manufacturing, vol. 21, no. 3, pp. 545–556, Mar. 2020, doi: 10.1007/S12541-019-00265-Z/FIGURES/22.

[22] L. Liu, B. M. Zhang, D. F. Wang, and Z. J. Wu, "Effects of cure cycles on void content and mechanical properties of composite laminates," Compos Struct, vol. 73, no. 3, pp. 303–309, Jun. 2006, doi: 10.1016/J.COMPSTRUCT.2005.02.001.

[23] I. Tretiak, L. F. Kawashita, and S. R. Hallett, "Manufacturing composite laminates with controlled void content through process control," Journal of Reinforced Plastics and Composites, vol. 43, no. 1–2, pp. 16–29, Jan. 2024, doi: 10.1177/07316844231154585.

[24] S. R. Ghiorse, "Effect of void content on the mechanical properties of carbon/epoxy laminates," S.A.M.P.E. Quarterly, vol. 24, no. 2, pp. 54–59, Jan. 1993, [Online]. Available: http://uoft.me/copvfair

[25] C. Blackwell, P. Simacek, R. Crane, S. Yarlagadda, and S. G. Advani, "A model for the autoclave consolidation of prepregs during manufacturing of complex curvature parts," International Journal of Material Forming, vol. 16, no. 6, Nov. 2023, doi: 10.1007/s12289-023-01784-x.

[26] J. Jaafar, J. P. Siregar, C. Tezara, M. H. M. Hamdan, and T. Rihayat, "A review of important considerations in the compression molding process of short natural fiber composites," International Journal of Advanced Manufacturing Technology, vol. 105, no. 7–8, pp. 3437–3450, Dec. 2019, doi: 10.1007/S00170-019-04466-8/FIGURES/16.

[27] A. Levy and P. Hubert, “Interstrand void content evolution in compression moulding of randomly oriented strands (ROS) of thermoplastic composites,” Compos Part A Appl Sci Manuf, vol. 70, pp. 121–131, Mar. 2015, doi: 10.1016/J.COMPOSITESA.2014.11.017.

[28] C. A. Grubb, D. J. Keffer, C. D. Webb, M. Kardos, H. Mainka, and D. P. Harper, “Paper fiber-reinforced polypropylene composites from nonwoven preforms: A study on compression molding optimization from a manufacturing perspective,” Compos Part A Appl Sci Manuf, vol. 185, p. 108339, Oct. 2024, doi: 10.1016/J.COMPOSITESA.2024.108339.

[29] M. John and R. V. Prakash, “Void content measurement in fiber reinforced plastic composites by X-ray computed tomography,” Materials Science Forum, vol. 928 MSF, pp. 38–44, 2018, doi: 10.4028/WWW.SCIENTIFIC.NET/MSF.928.38.

[30] E. Barocio et al., “Compression molding of hybrid continuous and discontinuous fiber reinforced thermoplastics for enhancing strength characteristics,” Society for the Advancement of Material and Process Engineering - North America, Apr. 2023. doi: 10.33599/SJ.v59no5.03.

[31] G. Kim, E. Barocio, S. Choi, M. Eichenhofer, J. Kalman, and R. B. Pipes, “Structural upcycling of thermoplastic composite recyclates through continuous fiber printed preforms,” Polym Compos, 2025, doi: 10.1002/PC.29547.

[32] A. C. M. Q. S. Santos, F. M. Monticeli, H. Ornaghi, L. F. de P. Santos, and M. O. H. Cioffi, “Porosity characterization and respective influence on short-beam strength of advanced composite processed by resin transfer molding and compression molding,” Polymers and Polymer Composites, vol. 29, no. 8, pp. 1353–1362, Oct. 2021, doi: 10.1177/0967391120968452.

[33] M. J. Donough, Shafaq, N. A. St John, A. W. Philips, and B. Gangadhara Prusty, “Process modelling of In-situ consolidated thermoplastic composite by automated fibre placement – A review,” Compos Part A Appl Sci Manuf, vol. 163, p. 107179, Dec. 2022, doi: 10.1016/J.COMPOSITESA.2022.107179.

[34] E. Oromiehie, B. Gangadhara Prusty, P. Compston, and G. Rajan, “Automated fibre placement based composite structures: Review on the defects, impacts and inspections techniques,” Compos Struct, 2019, doi: 10.1016/j.compstruct.2019.110987.

[35] A. Brasington, C. Sacco, J. Halbritter, R. Wehbe, and R. Harik, “Automated fiber placement: A review of history, current technologies, and future paths forward,” Composites Part C: Open Access, vol. 6, p. 100182, Oct. 2021, doi: 10.1016/J.JCOMC.2021.100182.

[36] H. Sun, R. Godin, A. Dong, S. V Hoa, H. Salek, and D. Ric Godin, “Effect of process parameters on the quality of laminates made by automated fiber placement (AFP) using out-of-autoclave (OOA) prepregs,” in ECCM17 - 17th European Conference on Composite Materials, Munich, Germany, Jun. 2016.

[37] J. N. Swamy, W. J. B. Grouve, S. Wijskamp, and R. Akkerman, “Vacuum-bag-only consolidation of C/PEKK fiber placed preforms with engineered gas evacuation channels,” Journal of Thermoplastic Composite Materials, vol. 37, no. 4, pp. 1309–1326, Apr. 2024, doi: 10.1177/08927057231177571.

[38] J. N. Swamy, W. J. B. Grouve, S. Wijskamp, and R. Akkerman, “An experimental study on filling of gaps and void pockets during vacuum-bag-only consolidation of fiber placed preforms,” Journal of Thermoplastic Composite Materials, vol. 38, no. 3, pp. 1089–1106, Mar. 2025, doi: 10.1177/08927057241259745/ASSET/EF2B123C-A896-4871-B921-15A54EE14C6A/ASSETS/IMAGES/LARGE/10.1177_08927057241259745-FIG17.JPG.

[39] J. G. Kirchhoff, N. T. Heathman, T. Yap, P. Koirala, T. B. Hudson, and M. Tehrani, “Interlaminar bonding in thermoplastic composites: A comparative analysis of laser AFP and post-processing,” Compos B Eng, vol. 294, p. 112156, Apr. 2025, doi: 10.1016/J.COMPOSITESB.2025.112156.

[40] T. Yap et al., “In-plane properties of an in-situ consolidated automated fiber placement thermoplastic composite,” Compos Part A Appl Sci Manuf, vol. 188, p. 108525, Jan. 2025, doi: 10.1016/j.compositesa.2024.108525.

[41] P. Wang et al., “Preparation of short CF/GF reinforced PEEK composite filaments and their comprehensive properties evaluation for FDM-3D printing,” Compos B Eng, vol. 198, p. 108175, Oct. 2020, doi: 10.1016/J.COMPOSITESB.2020.108175.

[42] J. M. Pappas, A. R. Thakur, M. C. Leu, and X. Dong, “A comparative study of pellet-based extrusion deposition of short, long, and continuous carbon fiber-reinforced polymer composites for large-scale additive manufacturing,” Journal of Manufacturing Science and Engineering, Transactions of the ASME, vol. 143, no. 7, Jul. 2021, doi: 10.1115/1.4049646.

[43] G. W. Melenka, B. K. O. Cheung, J. S. Schofield, M. R. Dawson, and J. P. Carey, “Evaluation and prediction of the tensile properties of continuous fiber-reinforced 3D printed structures,” Compos Struct, 2016, doi: 10.1016/j.compstruct.2016.07.018.

[44] M. A. Saleh, S. Olcun, M. Karam, R. Kempers, and G. W. Melenka, “High stiffness 3D-printed continuous pitch carbon fiber reinforced polymer composites,” J Compos Mater, vol. 58, no. 16, pp. 1873–1886, Jul. 2024, doi: 10.1177/00219983241249526.

[45] B. Akhoundi, A. H. Behravesh, and A. Bagheri Saed, “An innovative design approach in three-dimensional printing of continuous fiber–reinforced thermoplastic composites via fused deposition modeling process: In-melt simultaneous impregnation,” Proc Inst Mech Eng B J Eng Manuf, vol. 234, no. 1–2, pp. 243–259, Jan. 2020, doi: 10.1177/0954405419843780/ASSET/IMAGES/LARGE/10.1177_0954405419843780-FIG20.JPEG.

[46] K. A. Hamzah et al., “Effect of the printing orientation on the mechanical properties and thermal and electrical conductivity of ABS-ZnFe2O4 composites,” J Mater Eng Perform, vol. 28, no. 9, pp. 5860–5868, Sep. 2019, doi: 10.1007/S11665-019-04313-7/FIGURES/16.

[47] B. Tyagi, · Rajkumar Velu, and A. Raj, “Failure analysis and statistical validation of fused filament fabricated PETG composite for transtibial prosthetics,” Progress in Additive Manufacturing 2025, pp. 1–26, May 2025, doi: 10.1007/S40964-025-01113-5.

[48] J. Naranjo-Lozada, H. Ahuett-Garza, P. Orta-Castañón, W. M. H. Verbeeten, and D. Sáiz-González, “Tensile properties and failure behavior of chopped and continuous carbon fiber

composites produced by additive manufacturing," Addit Manuf, vol. 26, pp. 227–241, Mar. 2019, doi: 10.1016/J.ADDMA.2018.12.020.

[49] H. Gharehbaghi, A. M. Shojaei, M. Sadeghzadeh, and A. Farrokhabadi, "Residual stiffness and strength analysis of fatigue behavior in a 3D-printed honeycomb structure of continuous glass fiber-reinforced polylactic acid (PLA) composite," Composites Part C: Open Access, vol. 16, p. 100552, Mar. 2025, doi: 10.1016/J.JCOMC.2024.100552.

[50] U. Fasel, D. Keidel, L. Baumann, G. Cavolina, M. Eichenhofer, and P. Ermanni, "Composite additive manufacturing of morphing aerospace structures," Manuf Lett, vol. 23, pp. 85–88, Jan. 2020, doi: 10.1016/J.MFGLET.2019.12.004.

[51] P. Cheng et al., "A novel dual-nozzle 3D printing method for continuous fiber reinforced composite cellular structures," Composites Communications, vol. 37, p. 101448, Jan. 2023, doi: 10.1016/J.COCO.2022.101448.

[52] F. Wang, G. Wang, F. Ning, and Z. Zhang, "Fiber-matrix impregnation behavior during additive manufacturing of continuous carbon fiber reinforced polylactic acid composites," Addit Manuf, vol. 37, p. 101661, 2021, doi: 10.1016/j.addma.2020.101661.

[53] K. Wang et al., "Novel application of dual-nozzle 3D printer for enhanced in-situ impregnation 3D printing of dry continuous fiber reinforced composites," Compos Part A Appl Sci Manuf, vol. 183, p. 108231, Aug. 2024, doi: 10.1016/J.COMPOSITESA.2024.108231.

[54] M. Araya-Calvo et al., "Evaluation of compressive and flexural properties of continuous fiber fabrication additive manufacturing technology," Addit Manuf, vol. 22, pp. 157–164, Aug. 2018, doi: 10.1016/J.ADDMA.2018.05.007.

[55] Y. Chen, A. Klingler, K. Fu, and L. Ye, "3D printing and modelling of continuous carbon fibre reinforced composite grids with enhanced shear modulus," Eng Struct, vol. 286, Jul. 2023, doi: 10.1016/j.engstruct.2023.116165.

[56] F. Liu, E. Ferraris, and J. Ivens, "Mechanical investigation and microstructure performance of a two-matrix continuous carbon fibre composite fabricated by 3D printing," J Manuf Process, vol. 79, pp. 383–393, Jul. 2022, doi: 10.1016/J.JMAPRO.2022.04.050.

[57] S. S. Kumar, J. S. Akmal, and M. Salmi, “4D printing of shape memory polymer with continuous carbon fiber,” Progress in Additive Manufacturing, vol. 9, no. 6, pp. 1985–1995, Dec. 2023, doi: 10.1007/S40964-023-00553-1/TABLES/2.

[58] S. Olcun, Y. Ibrahim, C. Isaacs, M. Karam, A. Elkholy, and R. Kempers, “Thermal conductivity of 3D-printed continuous pitch carbon fiber composites,” Additive Manufacturing Letters, vol. 4, p. 100106, 2023, doi: 10.1016/j.addlet.2022.100106.

[59] M. K. Idris, P. Naderi, G. W. Melenka, and G. Grau, “Damage location sensing in carbon fiber composites using extrusion printed electronics,” Functional Composites and Structures, vol. 3, no. 4, Dec. 2021, doi: 10.1088/2631-6331/AC3731.

[60] C. Ghnatios and K. Fayazbakhsh, “Warping estimation of continuous fiber-reinforced composites made by robotic 3D printing,” Addit Manuf, vol. 55, Jul. 2022, doi: 10.1016/j.addma.2022.102796.

[61] S. Olcun, A. Elkholy, and R. Kempers, “High thermal conductivity continuous pitch carbon fiber 3D printed using a 6-axis robot arm,” Progress in Additive Manufacturing, vol. 9, no. 6, pp. 2189–2198, Dec. 2024, doi: 10.1007/S40964-024-00568-2/FIGURES/7.

[62] H. Kwon, M. Eichenhofer, T. Kyttas, and B. Dillenburger, “Digital Composites: Robotic 3D printing of continuous carbon fiber-reinforced plastics for functionally-graded building components,” In: Willmann, J., Block, P., Hutter, M., Byrne, K., Schork, T. (eds) Robotic Fabrication in Architecture, Art and Design 2018. ROBARCH 2018. Springer, Cham., pp. 363–376, Aug. 2019, doi: 10.1007/978-3-319-92294-2_28.

[63] S. Miri, J. Kalman, J. P. Canart, J. Spangler, and K. Fayazbakhsh, “Tensile and thermal properties of low-melt poly aryl ether ketone reinforced with continuous carbon fiber manufactured by robotic 3D printing,” International Journal of Advanced Manufacturing Technology, vol. 122, no. 2, pp. 1041–1053, Sep. 2022, doi: 10.1007/S00170-022-09983-7/FIGURES/9.

[64] M. Eichenhofer, J. C. H. Wong, and P. Ermanni, “Continuous lattice fabrication of ultra-lightweight composite structures,” Addit Manuf, vol. 18, pp. 48–57, Dec. 2017, doi: 10.1016/J.ADDMA.2017.08.013.

[65] M. Iragi, C. Pascual-González, A. Esnaola, C. S. Lopes, and L. Aretxabaleta, “Ply and interlaminar behaviours of 3D printed continuous carbon fibre-reinforced thermoplastic laminates; effects of processing conditions and microstructure,” Addit Manuf, vol. 30, p. 100884, Dec. 2019, doi: 10.1016/J.ADDMA.2019.100884.

[66] T. Heitkamp et al., “Stress-adapted fiber orientation along the principal stress directions for continuous fiber-reinforced material extrusion,” Progress in Additive Manufacturing, vol. 8, pp. 541–559, 2023, doi: 10.1007/s40964-022-00347-x.

[67] J. M. Chacón, M. A. Caminero, P. J. Núñez, E. García-Plaza, I. García-Moreno, and J. M. Reverte, “Additive manufacturing of continuous fibre reinforced thermoplastic composites using fused deposition modelling: Effect of process parameters on mechanical properties,” Compos Sci Technol, vol. 181, Sep. 2019, doi: 10.1016/j.compscitech.2019.107688.

[68] J. F. Christ, N. Aliheidari, A. Ameli, and P. Pötschke, “3D printed highly elastic strain sensors of multiwalled carbon nanotube/thermoplastic polyurethane nanocomposites,” Mater Des, vol. 131, pp. 394–401, Oct. 2017, doi: 10.1016/J.MATDES.2017.06.011.

[69] Y. Ibrahim, G. W. Melenka, and R. Kempers, “Additive manufacturing of Continuous Wire Polymer Composites,” Manuf Lett, vol. 16, pp. 49–51, Apr. 2018, doi: 10.1016/J.MFGLET.2018.04.001.

[70] Y. Ibrahim, G. W. Melenka, and R. Kempers, “Fabrication and tensile testing of 3D printed continuous wire polymer composites,” Rapid Prototyp J, vol. 24, no. 7, pp. 1131–1141, Oct. 2018, doi: 10.1108/RPJ-11-2017-0222.

[71] Y. Ibrahim, G. W. Melenka, and R. Kempers, “Flexural properties of three-dimensional printed continuous wire polymer composites,” Materials Science and Technology (United Kingdom), vol. 35, no. 12, pp. 1471–1482, Aug. 2019, doi: 10.1080/02670836.2019.1630085.

[72] Y. Ibrahim and R. Kempers, “Effective thermal conductivity of 3D-printed continuous wire polymer composites,” Progress in Additive Manufacturing, vol. 7, no. 4, pp. 699–712, Aug. 2022, doi: 10.1007/S40964-021-00256-5/FIGURES/12.

[73] C. Thompson, C. González, and J. LLorca, “Material extrusion fabrication of continuous metal wire-reinforced polymer–matrix composites,” Composites Communications, vol. 50, p. 102024, Oct. 2024, doi: 10.1016/J.COCO.2024.102024.

[74] Á. García de la Camacha, J. Sánchez del Río, and J. LLorca, “Additive manufacturing of quasi-isotropic wire-reinforced metal-polymer composite laminates,” Rapid Prototyp J, vol. 31, no. 7, pp. 1449–1460, 2025, doi: 10.1108/RPJ-11-2024-0467.

[75] V. Mishra, J. Kumar, S. Negi, and S. Kar, “3D printing of continuous metal fiber-reinforced recycled ABS with varying fiber loading,” Rapid Prototyp J, vol. 30, no. 8, pp. 1610–1623, Aug. 2024, doi: 10.1108/RPJ-02-2024-0087/FULL/PDF.

[76] A. Hamidi and Y. Tadesse, “Single step 3D printing of bioinspired structures via metal reinforced thermoplastic and highly stretchable elastomer,” Compos Struct, vol. 210, pp. 250–261, Feb. 2019, doi: 10.1016/J.COMPSTRUCT.2018.11.019.

[77] Z. Li, L. Wang, and G. Ma, “Mechanical improvement of continuous steel microcable reinforced geopolymer composites for 3D printing subjected to different loading conditions,” Compos B Eng, vol. 187, p. 107796, Apr. 2020, doi: 10.1016/J.COMPOSITESB.2020.107796.

[78] M. A. Saleh, R. Kempers, and G. W. Melenka, “3D printed continuous wire polymer composites strain sensors for structural health monitoring,” Smart Mater Struct, 2019, doi: 10.1088/1361-665X/aafdef.

[79] M. A. Saleh, R. Kempers, and G. W. Melenka, “A comparative study on the electromechanical properties of 3D-Printed rigid and flexible continuous wire polymer composites for structural health monitoring,” Sensors and Actuators A, vol. 328, p. 112764, 2021, doi: 10.1016/j.sna.2021.112764.

[80] M. A. Saleh, R. Kempers, and G. W. Melenka, “Fatigue behavior and electromechanical properties of additively manufactured continuous wire polymer composites for structural health

monitoring," Fatigue Fract Eng Mater Struct, vol. 45, no. 9, pp. 2630–2645, Sep. 2022, doi: 10.1111/ffe.13778.

[81] M. A. Saleh, A. Elkholy, G. W. Melenka, and R. Kempers, "Heat flux measurement using 3D-printed continuous wire polymer composite sensors," Case Studies in Thermal Engineering, vol. 42, p. 102739, Feb. 2023, doi: 10.1016/J.CSITE.2023.102739.

[82] Y. Ibrahim, R. Kempers, and A. Amirfazli, "3D printed electro-thermal anti-or de-icing system for composite panels," Cold Reg Sci Technol, 2019, doi: 10.1016/j.coldregions.2019.102844.

[83] B. Akhoundi, "An evaluation of the shape-memory behavior and mechanical properties of polylactic acid/Ni80Cr20 continuous wire composite produced by extrusion-based additive manufacturing and in-melt simultaneous impregnation method," Journal of Reinforced Plastics and Composites, vol. 43, no. 13–14, pp. 783–797, Jul. 2024, doi: 10.1177/07316844231197036.

[84] C. Thompson, C. González, and J. LLorca, "Additively-manufactured Mg wire-reinforced PLDL-matrix composites for biomedical applications," J Mech Behav Biomed Mater, vol. 153, p. 106496, May 2024, doi: 10.1016/J.JMBBM.2024.106496.

[85] J. F. Rodríguez, J. P. Thomas, and J. E. Renaud, "Mechanical behavior of acrylonitrile butadiene styrene fused deposition materials modeling," Rapid Prototyp J, vol. 9, no. 4, pp. 219–230, 2003, doi: 10.1108/13552540310489604.

[86] M. Somireddy, C. V. Singh, and A. Czekanski, "Analysis of the material Behavior of 3D printed laminates via FFF," Exp Mech, vol. 59, no. 6, pp. 871–881, Jul. 2019, doi: 10.1007/S11340-019-00511-5/FIGURES/9.

[87] Y. Tao et al., "A review on voids of 3D printed parts by fused filament fabrication," Journal of Materials Research and Technology, vol. 15, pp. 4860–4879, Nov. 2021, doi: 10.1016/J.JMRT.2021.10.108.

[88] J. F. Rodriguez, J. P. Thomas, and J. E. Renaud, "Characterization of the mesostructure of fused-deposition acrylonitrile-butadiene-styrene materials," Rapid Prototyp J, vol. 6, no. 3, pp. 175–185, 2000, doi: 10.1108/13552540010337056.

[89] B. Akhoundi, M. Nabipour, F. Hajami, and D. Shakoori, “An Experimental Study of Nozzle Temperature and Heat Treatment (Annealing) Effects on Mechanical Properties of High-Temperature Polylactic Acid in Fused Deposition Modeling,” Polym Eng Sci, vol. 60, no. 5, May 2020, doi: 10.1002/pen.25353.

[90] K. Fayazbakhsh, M. Movahedi, and J. Kalman, “The impact of defects on tensile properties of 3D printed parts manufactured by fused filament fabrication,” Mater Today Commun, vol. 18, pp. 140–148, Mar. 2019, doi: 10.1016/J.MTCOMM.2018.12.003.

[91] M. Mehdikhani, L. Gorbatikh, I. Verpoest, and S. V. Lomov, “Voids in fiber-reinforced polymer composites: A review on their formation, characteristics, and effects on mechanical performance,” J Compos Mater, vol. 53, no. 12, pp. 1579–1669, May 2019, doi: 10.1177/0021998318772152/ASSET/IMAGES/LARGE/10.1177_0021998318772152-FIG20.JPEG.

[92] J. Patou, E. De Luycker, and G. Bernhart, “Influence of void content on the mechanical properties of carbon/PPS laminates,” in ECCM17 - 17th European Conference on Composite Materials, Munich, Jun. 2016. Accessed: Oct. 02, 2024. [Online]. Available: https://www.researchgate.net/publication/317527441_INFLUENCE_OF_VOID_CONTENT_ON_THE_MECHANICAL_PROPERTIES_OF_CARBONPPS_LAMINATES

[93] G. Chabaud, M. Castro, C. Denoual, and A. Le Duigou, “Hygromechanical properties of 3D printed continuous carbon and glass fibre reinforced polyamide composite for outdoor structural applications,” Addit Manuf, vol. 26, pp. 94–105, Mar. 2019, doi: 10.1016/J.ADDMA.2019.01.005.

[94] Z. Tang, L. Guo, Z. Li, K. Huang, T. Zheng, and R. Sun, “A comparative study of void characteristics on the mechanical response of unidirectional composites,” Mechanics of Materials, vol. 174, p. 104456, Nov. 2022, doi: 10.1016/J.MECHMAT.2022.104456.

[95] Z. Eren, C. A. Burnett, D. Wright, and Z. Kazancı, “Compressive characterisation of 3D printed composite materials using continuous fibre fabrication,” 2023, doi: 10.1016/j.ijlmm.2023.05.002.

[96] J. Xiang et al., “Effect of heat-treatment on compressive response of 3D printed continuous carbon fiber reinforced composites under different loading directions,” J Appl Polym Sci, vol. 140, no. 3, p. e53330, Jan. 2023, doi: 10.1002/APP.53330.

[97] M. Y. Ali, G. K. M. Rao, and B. A. Prasad, “Experimental investigation of influence of post-processing variables on mechanical strength and surface quality of 3D printed carbon fiber reinforced polylactic acid samples,” Progress in Additive Manufacturing 2025, pp. 1–13, Feb. 2025, doi: 10.1007/S40964-025-01023-6.

[98] S. Valvez, P. N. B. Reis, and J. A. M. Ferreira, “Effect of annealing treatment on mechanical properties of 3D-Printed composites,” Journal of Materials Research and Technology, vol. 23, pp. 2101–2115, Mar. 2023, doi: 10.1016/J.JMRT.2023.01.097.

[99] H. Mei, Z. Ali, Y. Yan, I. Ali, and L. Cheng, “Influence of mixed isotropic fiber angles and hot press on the mechanical properties of 3D printed composites,” Addit Manuf, vol. 27, pp. 150–158, May 2019, doi: 10.1016/J.ADDMA.2019.03.008.

[100] M. A. Valverde, J. P. H. Belnoue, R. Kupfer, L. F. Kawashita, M. Gude, and S. R. Hallett, “Compaction behaviour of continuous fibre-reinforced thermoplastic composites under rapid processing conditions,” Compos Part A Appl Sci Manuf, vol. 149, Oct. 2021, doi: 10.1016/j.compositesa.2021.106549.

[101] N. van de Werken, P. Koirala, J. Ghorbani, D. Doyle, and M. Tehrani, “Investigating the hot isostatic pressing of an additively manufactured continuous carbon fiber reinforced PEEK composite,” Addit Manuf, vol. 37, p. 101634, 2021, doi: 10.1016/j.addma.2020.101634.

[102] M. Kashfi, M. Tehrani, and M. Tehrani, “Effects of void content on flexural properties of additively manufactured polymer composites,” 2021, doi: 10.1016/j.jcomc.2021.100173.

[103] X. Sun, M. Mazur, and C.-T. Cheng, “An interlaced toolpath strategy for void reduction in material extrusion additive manufacturing,” Progress in Additive Manufacturing 2025, pp. 1–17, May 2025, doi: 10.1007/S40964-025-01163-9.

[104] A. Uşun, B. B. Vatandaş, and R. Gümrük, “Enhanced mechanical properties of continuous carbon fiber reinforced polyether-ether-ketone composites via infrared preheating and

high fiber volume fraction," Addit Manuf, vol. 89, p. 104289, Jun. 2024, doi: 10.1016/J.ADDMA.2024.104289.

[105] T. Yiwen, T. Yuegang, Z. Fan, and Z. Jun, "Laser assisted rapid 3D printing of continuous carbon fiber reinforced plastics: Simulation, characterization, and properties," Polym Compos, vol. 44, no. 6, pp. 3084–3094, Jun. 2023, doi: DOI:10.1002/pc.27303.

[106] Z. Ouyang, L. Yang, Z. Pi, Z. Wang, C. Yan, and Y. Shi, "Robot-assisted laser additive manufacturing for high-strength/low-porosity continuous fiber-reinforced thermoplastic composites," Compos Sci Technol, vol. 247, p. 110397, Mar. 2024, doi: 10.1016/J.COMPSCITECH.2023.110397.

[107] M. Ueda et al., "3D compaction printing of a continuous carbon fiber reinforced thermoplastic," Compos Part A Appl Sci Manuf, vol. 137, Oct. 2020, doi: 10.1016/j.compositesa.2020.105985.

[108] Y. Asano, M. Ueda, M. Yamawaki, R. Matsuzaki, A. Le Duigou, and M. Castro, "Layer-wise compaction 3D printing: void reduction and interfacial enhancement for continuous carbon fiber–reinforced thermoplastics," Advanced Composite Materials, pp. 1–15, Feb. 2025, doi: 10.1080/09243046.2025.2459672.

[109] N. Elderfield and J. C. H. Wong, "Discrete in-situ consolidation of additively manufactured continuous fiber-reinforced polymer composites," Compos Part A Appl Sci Manuf, vol. 171, Aug. 2023, doi: 10.1016/j.compositesa.2023.107562.

[110] H. Jouhara et al., "Thermoelectric generator (TEG) technologies and applications," International Journal of Thermofluids, vol. 9, p. 100063, Feb. 2021, doi: 10.1016/J.IJFT.2021.100063.

[111] S. Bruschi and A. Ghiotti, "3.03 Hot Stamping," in Comprehensive Materials Processing: Thirteen Volume Set, vol. 3, Elsevier, 2014, pp. V3-27-V3-54. doi: 10.1016/B978-0-08-096532-1.00303-4.

[112] L. Roumy, F. Touchard, D. Marchand, T. Quynh, T. Hoang, and F. Martinez-Hergueta, “Durability of Joule effect of 3D printed carbon black/polylactic acid: Electrical cyclic tests and analytical modelling,” Int J Fatigue, vol. 173, 2023, doi: 10.1016/j.ijfatigue.2023.107677.

[113] A. Georgopoulou, P. Diethelm, M. Wagner, R. Spolenak, and F. Clemens, “Soft self-regulating heating elements for thermoplastic elastomer-based electronic skin applications,” https://home.liebertpub.com/3dp, vol. 11, no. 2, pp. E828–E838, Apr. 2024, doi: 10.1089/3DP.2022.0242.

[114] “JEC Composites Web TV | PENTAXIA: Self-Curing Isothermal Composite Tooling for Low-Energy and Large-Scale Applications.” Accessed: Apr. 28, 2025. [Online]. Available: https://www.jeccomposites.tv/Composites-Exchange-1707130976/pentaxia-self-curing-isothermal-composite-tooling-for-low-energy-and-large-scale-applications/

[115] J. Park, D. Kang, and H. S. Kim, “Thermal characteristics of resistive heating composite panels for the interior parts of railway vehicles,” Advanced Composite Materials, Jan. 2025, doi: 10.1080/09243046.2024.2352892.

[116] C. Zeng, L. Liu, W. Bian, Y. Liu, and J. Leng, “4D printed electro-induced continuous carbon fiber reinforced shape memory polymer composites with excellent bending resistance,” Compos B Eng, vol. 194, p. 108034, Aug. 2020, doi: 10.1016/J.COMPOSITESB.2020.108034.

[117] J. Reese, M. Vorhof, G. Hoffmann, K. Böhme, and C. Cherif, “Joule heating of dry textiles made of recycled carbon fibers and PA6 for the series production of thermoplastic composites,” J Eng Fiber Fabr, vol. 15, 2020, doi: 10.1177/1558925020905828.

[118] A. Cortés, A. Esperanza, J. Gómez-Sánchez, X. F. Sanchez-Romate, S. G. Prolongo, and A. Jiménez-Suárez, “Combining de-icing and self-healing for wind blades through an innovative multilayer coating approach,” Polym Compos, Apr. 2024, doi: 10.1002/PC.29252.

Chapter 3 - Self-Heating Consolidation Method for 3D-Printed Continuous Wire Polymer Composites

3.1. Introduction

Additive manufacturing (AM) has filled a significant gap in the composite manufacturing industry which allows geometrically complex composite parts to be fabricated consistently. In particular, fused filament fabrication (FFF) allows for the manufacturing of geometrically complex composite parts in a cost-effective manner. Short-fibre thermoplastic filaments, such as polyethylene terephthalate glycol (PETG), nylon, or polyetheretherketone (PEEK) reinforced with short carbon or glass fibres have been printed using commercial and desktop FFF 3D printers [1-3]. Companies such as Markforged, 9T Labs, and Anisoprint make dual-extrusion 3D printers that print high strength-to-weight ratio thermoplastic parts reinforced with continuous carbon, glass, or aramid fibres. However, these printers can come with high initial costs [4-6]. Due to their high strength and ease of manufacturing, there has been a significant increase in research on continuous fibre-reinforced 3D-printed parts, both using industrial printers and custom machines in an effort to address current high costs. The use cases of continuous fibre 3D-printed parts that have been studied includes studies on increased strength [7-11], 4D printing of shape memory polymers [12], sensing applications [13], and improved thermal properties [14].

Recent studies have substituted metal wires as the reinforcement material for increased strength, using modified desktop 3D printers. The electrically conductive metal wires also enable sensing capabilities. Similar to continuous fibre composites, these metal-wire-reinforced 3D-printed parts

exhibit high strength compared with their thermoplastic counterparts while providing different functionalities such as in-part heating, sensing applications, and shape memory behaviour. Ibrahim *et al.* [15] developed a method of co-extruding continuous metal wire and polymer matrix using a modified Prusa i3 MK3. They then performed three-point bend tests on continuous wire polymer composites (CWPCs), testing multiple filament materials reinforced with NiCr wire. Ultimate flexural strength improvements up to 20.2% were found in CWPC samples compared with the non-reinforced 3D-printed samples [16]. In subsequent studies, the author used nickel chromium (NiCr) wires due to their high electrical resistance to fabricate CWPC de-icing panels [17] and continuous copper wires for improved thermal conductivity of 3D-printed parts [18]. Using the same manufacturing method, Saleh *et al.* [19] used continuous copper and NiCr wires for structural health monitoring by taking in-part strain measurements during tensile testing. Thompson *et al.* [20] built a printer with separate wire and polymer print heads to reinforce polylactic acid (PLA) samples with aluminum wire in a stacking sequence. This study saw a significant increase in the tensile stiffness and strength of the materials with 25% wire volume fraction. A study performed by Akhoundi [21] found that applying a constant voltage through the continuous NiCr wire reinforcement of 3D-printed samples resulted in uniform heating of the sample and shape memory behaviour. While previous work in continuous metal wire composite 3D printing has shown significant improvements in strength, previous studies have also identified voids in their samples, mainly surrounding the continuous wire reinforcement due to the nature of the manufacturing method. This decreased adhesion between the polymer raster and the wire reinforcement material can cause decreased strength and stiffness, as well as decreased accuracy in applications involving sensing. Void volume fractions in literature have been found to be between 2.01% and 24% [16], [19], [20], [22].

The presence of voids in composite materials is known to have a negative effect on mechanical properties such as flexural strength, transverse strength, and interlaminar shear strength by decreasing the adhesion between the fibres and matrix which act as stress concentrations under loading [23-25]. A detailed finite element study by Tang *et al.* found that 2% void content in unidirectional AS24 carbon fibre composites can cause a 25% decrease in transverse and shear strength [26]. Voids are common in both polymer and polymer composite 3D-printed parts and can be affected by printing properties such as raster orientation and infill density [2]. However, they still yield high void content, resulting in a need for more further void reduction techniques. Previous studies have used different post-processing heat treatment methods on 3D-printed composite materials, and these have reduced voids between printed layers [30-32]. A study performed by Valvez *et al.* [30] studied the annealing effects of non-reinforced, discontinuous carbon-fibre-reinforced, and discontinuous-Kevlar-reinforced PETG samples. Samples were annealed at varying temperatures above the glass transition temperature (T_g) in an oven, and they displayed 10.2%, 31.8%, and 11.1% increases in flexural strength, and 17.6%, 61.1%, and 62.6% increases in flexural modulus, respectively. In-situ methods for layer-by-layer consolidation have also been performed on continuous fibre 3D-printed composites. Some in-situ consolidation methods include alternating the printing path [31], infrared laser curing the deposited layer [25], or using custom print-heads with a laser to keep the polymer matrix heated, and a consolidation roller following the printing nozzle to compact the continuous reinforced raster as it is printed [32], [33]. Asano *et al.* [34] performed layer-wise compaction on 3D-printed nylon samples reinforced with continuous carbon fibre. They found the compaction roller decreased the porosity in samples from 11% to 2.8%. Their compaction rolling process yielded a 32.6% and 11.2% increase in flexural modulus and strength, respectively.

Post-processing techniques have also proven to be effective, mainly using compression molding or hot-pressing techniques. A study conducted by van de Werken *et al.* [35] tested the hot isostatic pressing (HIP) of 42% fibre volume fraction carbon fibre/PEEK composites which were 3D printed using a 5-axis robot arm. Their study showed a significant decrease in void content at several elevated temperatures between the glass transition and heat deflection temperatures of PEEK and the composite, respectively. The study found that flexural and interlaminar shear strength improved for HIP temperatures closer to the glass transition temperature but decreased the closer the HIP processing temperature got to the heat deflection temperature. A subsequent finite element analysis (FEA) study by Kashfi *et al.* [36] found that a 52% decrease in void fraction percentage due to HIP resulted in the most significant increases in flexural modulus, flexural strength, and interlaminar shear strength.

Unidirectional reinforced CWPCs are most often fabricated and tensile tested. However, flexural, shear and transverse properties are more significantly affected by voids, due to the loading distribution between fibre and matrix under non-tensile loads. This study aims to develop a consolidation procedure, combining the principles of resistive heating and hot-pressing for composite manufacturing and the reduction of voids in 3D-printed continuous wire-reinforced samples. A thermal model was created and validated to estimate the consolidation procedure parameters. Image processing was utilized to assess the effect of the procedure developed on the cross-section of unidirectional reinforced CWPCs by quantifying the void and wire volume fractions. Three-point flexural tests were performed as well to determine the flexural strength and stiffness of the CWPCs.

3.2. Materials & Methodology

3.2.1. Materials and Sample Fabrication

A modified FFF 3D printer (Prusa i3 MK2, Prusa Research, Prague, Czech Republic) co-extruded continuous wire reinforcement in each deposited polymer raster through a single commercial 1 mm diameter hardened-steel tip nozzle (CM2 1.0 mm nozzle - RepRap (V6), Microswiss LLC., Minnesota, United States), as seen in Figure 3-1. The print head used was the same one used by Ibrahim *et al.* [15], [16], so a nozzle diameter of 1 mm was chosen as it was roughly 10 times larger than the diameter of the wire used in this study. The layer height, or extrusion height, was chosen as 0.5 mm, since it is common in 3D printing to use a layer height that is half of the nozzle diameter for good bed adhesion.

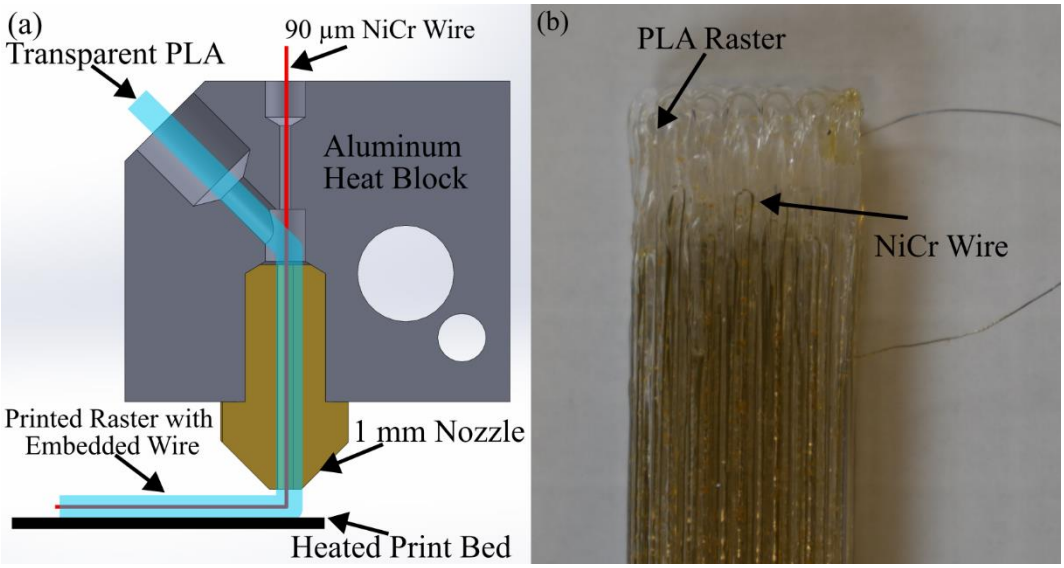

Figure 3-1: (a) Modified print head design for co-extrusion of continuous wire and polymer raster and (b) sample with visible wires printed unidirectionally embedded in polymer rasters

The polymer used was transparent PLA filament (1.75 mm Transparent PLA, Eryone, China), while a continuous 0.09 mm diameter ML polyamide enamel coated NiCr resistance wire (39

AWG Evanohm Alloy S Wire, Carpenter Technology Corporation, Pennsylvania, United States) was used for the reinforcement material. The wires were pre-measured to obtain repeatable lengths in the samples. Each end of the wire was extended out from the printed sample to allow for connections during the consolidation procedure. A custom GCode was generated using an open-source GCode design program (FullControl GCode Designer, Loughborough, England) to customize the path of the print head (Figure 3-2) [37]. Preliminary sample printing trial and error was performed by varying printing parameters such as flow rate, nozzle temperature and printing speed to determine the parameters that yielded the optimal results. The printing parameters used for the study can be seen in Table 3-1.

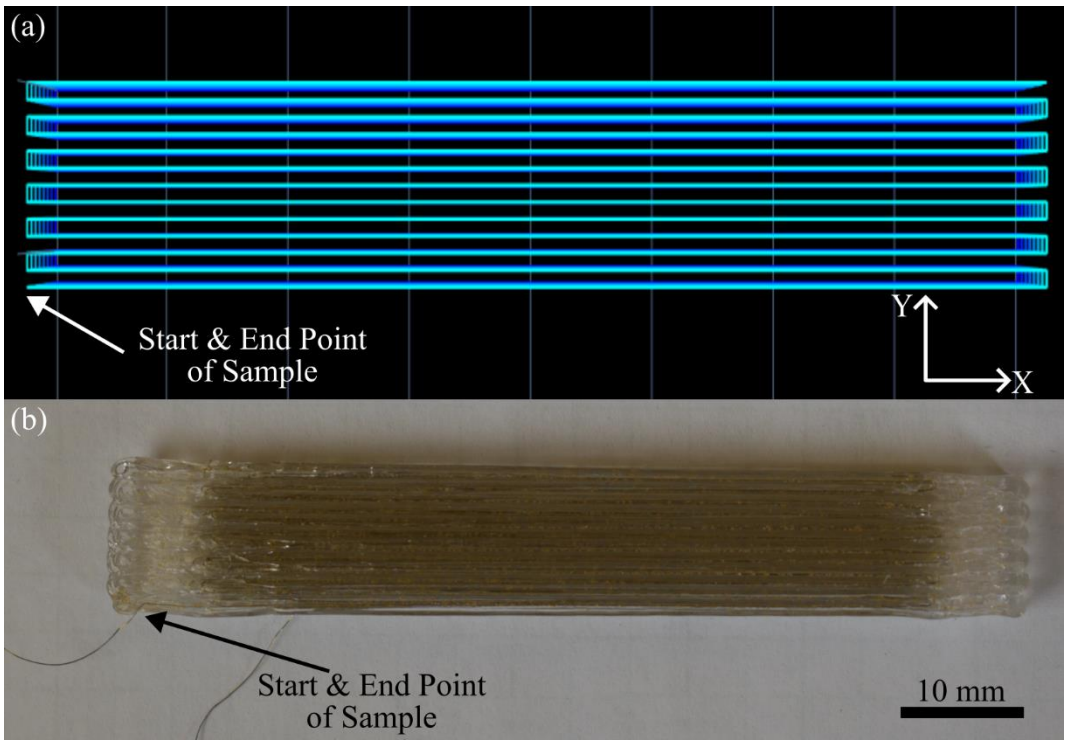

Figure 3-2: Printed continuous wire polymer composites: (a) display of toolpath from FullControl GCode and (b) printed unprocessed sample

Table 3-1: Sample printing parameters

Printing Parameter	Value
Nozzle Temperature	200°C
Bed Temperature	50°C
Printing Speed	6 mm/s
Fan Speed	60%
Flow Rate	90%
Extrusion Width	1.0 mm
Extrusion Height (Layer Thickness)	0.5 mm
Number of Layers	8
Nozzle Diameter	1 mm
Wire Diameter	0.09 mm

After printing, excess PLA was removed from the extended wire ends, and the electrical resistance of the reinforcement wire of each sample was measured using a digital multimeter (NTK028, Neoteck, China). A total of 33 samples (Table 3-2) were printed with nominal dimensions of 80 mm long x 13 mm wide x 4 mm thick, according to the ASTM D7264 standard [38]. Nine samples were used to validate the conduction and resistive heating thermal analytical models, and the consolidation procedure incorporated both. Three samples were allocated to each model validation. Samples for testing were split into three sample types: sample type A for unprocessed samples, sample type B for samples that were only hot-pressed, and sample type C for samples that underwent the full consolidation procedure. Of the eight samples of each type, five were used for three-point bend tests, and three were used for optical microscopy.

Table 3-2: Testing matrix; showing testing procedure, sample type, and no. of samples

Testing Procedure	Sample Type	No. of Samples
Analytical Model Validation	Conduction Model	3
	Resistive Heating Model	3
	Consolidation (Conduction + Resistive Heating)	3
Three-Point Flexural Test	Sample Type A – Unprocessed	5
	Sample Type B – Hot-Pressed	5
	Sample Type C – Consolidated	5
Optical Microscopy	Sample Type A – Unprocessed	3
	Sample Type B – Hot-Pressed	3
	Sample Type C – Consolidated	3
Total		33

3.2.2. Consolidation Procedure

To reduce voids, samples were first heated to a temperature above the glass transition temperature (T_g) of the PLA using two aluminum platens mounted to a 3 kN load cell, and then uniformly compressed. Type B samples underwent hot-pressing, where they were heated above T_g by 1D transient conduction only. Type C samples underwent the consolidation procedure developed in this study. The consolidation procedure heated samples above T_g by applying 1D transient conduction, combined with resistive heating of the continuous reinforcement wire for uniform internal heating (Figure 3-3).

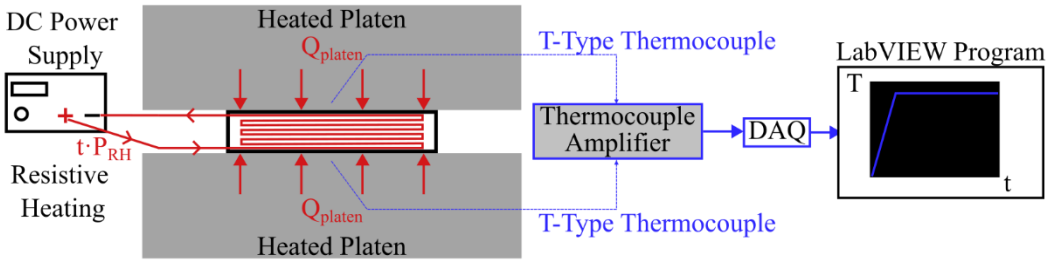

Figure 3-3: Schematic of the heating step of CWPC samples through 1D conduction from heated platens and resistive heating of the continuous wire from an external power supply, outputting thermocouple data from platens to LabVIEW program for consistent temperature vs time readings

3.2.2.1. PLA Filament Characterization Using DSC Analysis

PLA is a thermoplastic semi-crystalline polymer; therefore, it has both a T_g and a melting temperature (T_m). In order to reshape and improve the bond between rasters while preventing significant sample deformation, samples were heated to an equilibrium temperature above their T_g but below their T_m. Differential scanning calorimetry (DSC) was performed according to ASTM D3418-21 [39] to determine the T_g of the polymer matrix using a differential scanning calorimeter (Discovery DSC 250, TA Instruments, Delaware, United States). Three samples with masses of 10.3 mg, 10.6 mg, and 10.3 mg, were tested in a nitrogen atmosphere with a flow rate of 50 mL/min. To remove the thermal history, samples were heated to 215°C at 20 °C/min, kept isothermal for 5 min, cooled to 0°C at 20 °C/min, and then kept isothermal for another 5 min. The samples were then heated a second time to 215°C at a rate of 20 °C/min.

The normalized heat flow vs temperature graph for the second heat cycle was plotted for all three samples (see Figure 3-4). The extrapolated onset and end temperatures were approximated for each graph, and the midpoint temperature was determined as the glass transition temperature, as outlined in ASTM 3418. The average T_g and T_m of the three samples was 58°C and 168°C, respectively.

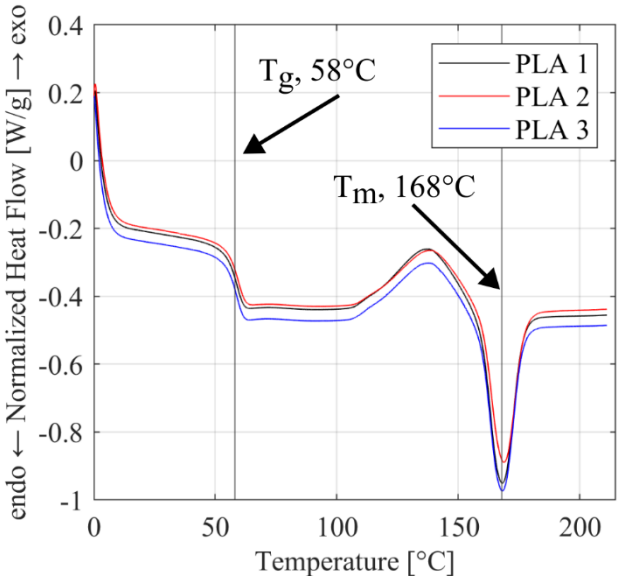

Figure 3-4: DSC second heat cycle results for three PLA filament samples showing glass transition and melting temperatures

3.2.2.2. Consolidation Procedure Outline

Instrumented aluminum platens were mounted to a 3 kN load cell universal testing machine (UTM; ElectroPuls E3000, Instron, Massachusetts, United States). A consolidation procedure was developed and performed to heat the polymer matrix to above its T_g; then, voids in the samples were filled by applying a controlled compression force using the heated aluminum plates mounted in the UTM. Heating of the samples was performed by conduction between the aluminum platens and resistive heating by passing a constant voltage through the continuous NiCr wire reinforcement. The aluminum platens were fastened to the top grips and load cell of the UTM and heated to 70°C, which is 12°C above the calculated T_g of the PLA matrix. Both the hot-pressing and consolidation procedures consisted of the same steps; timing differed based on the thermal modelling and testing results.

In the first step of both procedures, samples were placed on the bottom plate, and the top plate was lowered until it made contact with the top of the sample. The top plate was held at this

position for 120 s during hot-pressing and 45 s during consolidation. During the consolidation procedure, a constant 90 V was supplied for the 45 s from a 120 V DC power supply (6655A, Hewlett Packard, California, United States) connected to the ends of the continuous wire in the samples. Analytical models for the 1D transient conduction temperature response and resistive heating were developed. The time required to heat samples to the glass transition temperature was determined from the results of the analytical model validation testing. To ensure thermal equilibrium through the thickness of samples for both hot-pressing and the consolidation procedure, the samples were heated for longer than the thermal model testing required. After thermal equilibrium was reached and the sample was at the glass transition temperature, 2.8 MPa of compression force, the maximum force applicable by the UTM, was applied and held for 15 s. After compression, the top plate was lifted, and the sample was removed and allowed to cool to room temperature.

3.2.3. Thermal Modelling of Consolidation Procedure

Thermal modelling was performed to determine the time required to heat the samples to the desired temperature before compression. A 1D transient heat conduction model was developed for the temperature response of the centre of a plane wall during hot-pressing and Ohm's law was used to determine the time required to heat the sample to the desired temperature by resistive heating. Equating the thermal energy from the platens and the resistive heating during the consolidation procedure allowed for faster sample heating. The desired temperature of the centre of the sample was 65°C, chosen because it was above T_g, but well below T_m. The initial temperature of the centre of the sample was taken as room temperature, 20°C. The specified constant surface temperature assumption was applied, which assumed that from time t = 0 s, the surface temperature of the sample was held constant at, in this case, the temperature of the

platen, 70°C. Figure 5 shows the schematic of the full heating step of the consolidation procedure, including 1D conduction from the platens and the energy generated from the resistive heating.

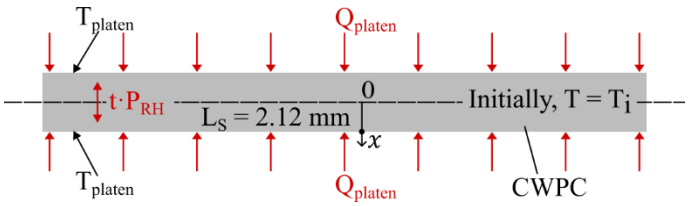

Figure 3-5: Heating step of the consolidation procedure, showing the temperatures of the platens and the initial sample centre temperature, with the thermal energy from the platens by 1D transient conduction and resistive heating energy generation within the sample

A 1D conduction model was used to determine the time required to heat the samples to the desired temperature. The dimensionless temperature response at the sample centre is given by the one-term approximation for a plane wall [40]

$$\frac{T_0 - T_{platen}}{T_i - T_{platen}} = A_1 e^{{\lambda_1}^2 \tau} \qquad \text{(Eq. 3-1)}$$

where T_0 is the desired temperature of the centre of the sample after heating, T_{platen} is the temperature of the surface of the sample, T_i is the initial temperature of the centre of the sample; A_1 and λ_1 are tabulated constants based on the Biot number (Bi), 1.2732 and 1.5708 rad, respectively [40]. Bi is the ratio of convection at the surface of the sample to the conduction within it. A specified surface temperature assumption is used because the top and bottom of the sample are in contact with the heated platens from time t = 0 s and therefore Bi is approximated to be infinity. The Fourier number, represented by τ, is used to determine the conduction through the sample relative to the heat stored in the sample. The one-term approximation is valid for a Fourier number greater than 0.2.

The relation given in (Eq. 2-1) is used to determine the value of the dimensionless time, or Fourier number τ. The equation for τ is rearranged to find the time t, required to heat the sample through the centre to the desired 65°C using [40]

$$t = \frac{\tau {L_S}^2}{\alpha} \quad \text{(Eq. 3-2)}$$

where the Fourier number is a dimensionless value that gives the relationship between the thermal diffusivity of the PLA matrix α = 0.058E-06 m^2/s [41], L_S is the average measured distance between the surface of the plate in contact with the sample and the sample's centre 2.12 mm and t is the time it takes for the sample centre to reach T_0.

The fraction of thermal energy through the sample by 1D conduction is given by [40]

$$\frac{Q_{platen}}{mC_p\left(T_{platen} - T_i\right)} = 1 - \frac{T_0 - T_{platen}}{T_i - T_{platen}} \cdot \frac{Sin(\lambda_1)}{\lambda_1} \quad \text{(Eq. 3-3)}$$

Where Q_{platen} is the thermal energy from the platen through the sample by conduction, m is the mass of the sample and C_p is the specific heat capacity of the sample, calculated using the rule of mixtures with a wire volume fraction of 1.18%.

Resistive heating occurs when running an electrical power through a resistive material. NiCr wire was chosen for its high electrical resistance of 66.6 Ω/ft [42], allowing for self heating of the sample. Ohm's law gives the electrical power through the wire by

$$P_{RH} = \frac{V^2}{R} \quad \text{(Eq. 3-4)}$$

where P_{RH} is the electrical power supplied to the wire for resistive heating, V is the supplied voltage and R is the measured wire resistance of the samples.

The consolidation procedure developed in this study aimed to decrease the time required to heat the sample through the centre by applying equal thermal energy externally from the heated platens and internally through resistive heating. Given the Q_{platen} found in (Eq. 3-3), the time required for samples to heat to 65°C was calculated using

$$t = \frac{Q_{platen}}{P_{RH}} = \frac{Q_{platen} \cdot R}{V^2} \qquad \text{(Eq. 3-5)}$$

the average measured wire resistance of the samples was R = 1456 ± 2.8 Ω.

Bare T-Type thermocouple wires (COCO-005, Omega Engineering Inc., Connecticut, United States) were embedded in the fourth layer of nine samples, with the junction placed in the centre (Figure 3-6) to test the validity of the 1D transient conduction model, the resistive heating model, and the developed consolidation procedure. The results from the thermal analysis were used to determine the time required for proper consolidation.

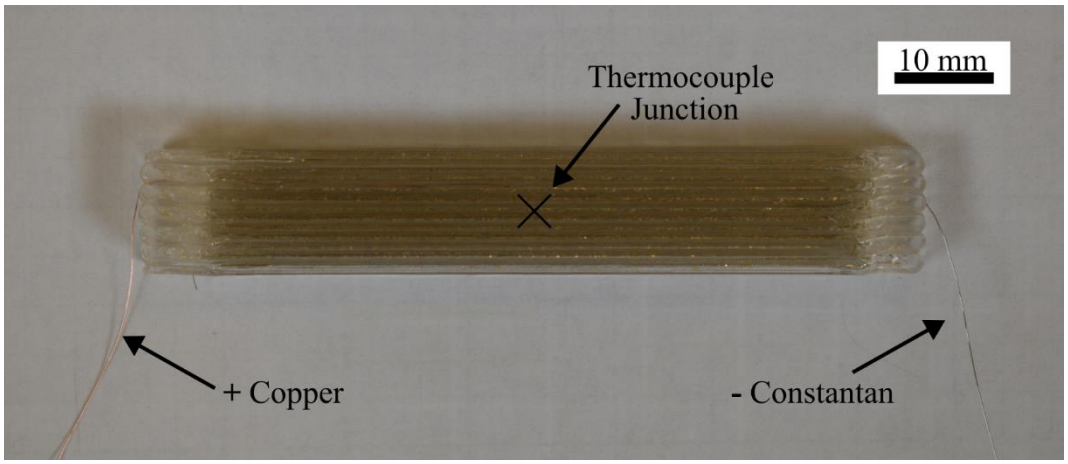

Figure 3-6: CWPC sample with T-type thermocouple embedded in middle layer, in the centre of the sample

3.2.4. Optical Microscopy & Image Processing

Samples were cut and mounted in clear epoxy (West Systems 105 Epoxy Resin, West Systems, Michigan, United States). The samples were sequentially ground using 120, 400, 600, 800, and 1200 grit sandpaper discs. Next, they were polished using 1.0 μm followed by 0.05 μm alumina powder. After grinding and polishing, optical microscopy with 2.5x magnification was performed on the samples to view the cross-section of the samples (ZEISS Axio Imager 2, Zeiss Group, Baden-Württemberg, Germany). Cross-section microscope images of samples were stitched together with a 25% overlap using image processing software (ImageJ, National Institutes of Health, Maryland, United States). The image processing steps for sample type A are shown in Figure 3-7.

The paintbrush tool in ImageJ was used to fill in voids which were not contrasted in the background of the images or were filled with the alumina powder. The background of the stitched images were painted black for the wire analysis, then inverted to white for the void image analysis to remove the noise caused by the light reflection on the epoxy.

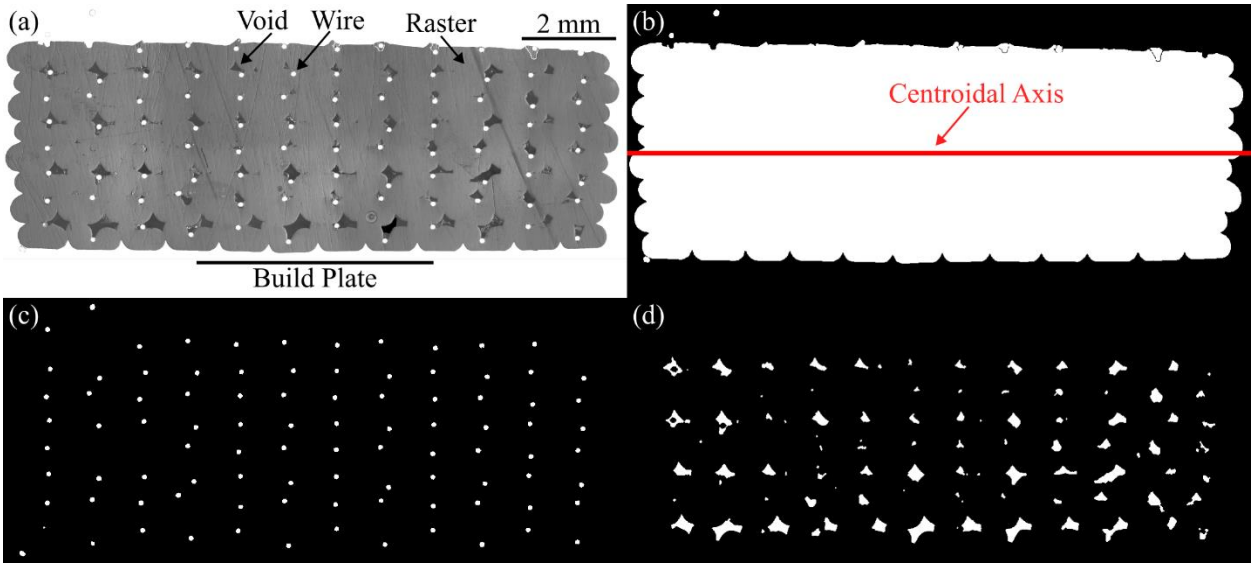

Figure 3-7: Image processing steps: (a) optical microscope image of unprocessed sample with white background for image processing with subsequent (b) cross-section of sample with centroidal axis highlighted for image processing, (c) segmented image of wires, and (d) segmented image of voids

A MATLAB image processing code (MATLAB R2023b, The MathWorks Inc., Massachusetts, United States) was written to determine the wire volume fraction (W_{vf}) and void volume fraction (V_{vf}). Thresholding, binarization, and morphological operations were performed to isolate wires and voids in images for processing. Histogram equalization and a median filter were applied to void images as necessary to enhance contrast between the voids and rasters, enabling more effective processing. The cross-section of the sample was isolated by thresholding, and the centroidal axis for the samples were found using the *regionprops* function in MATLAB (Figure 3-7b).

The *regionprops* function in MATLAB was used to determine the areas of the wires (Figure 3-7c) and voids (Figure 3-7d) to calculate the W_{vf} and V_{vf}, respectively. The location of the centroid of each wire and void relative to the centroidal axis of the sample was found using regionprops to determine the effect of the consolidation procedure on the size of the voids

relative to their location. The image processing steps for sample type B and sample type C can be seen in Figure 3-8 and Figure 3-9, respectively.

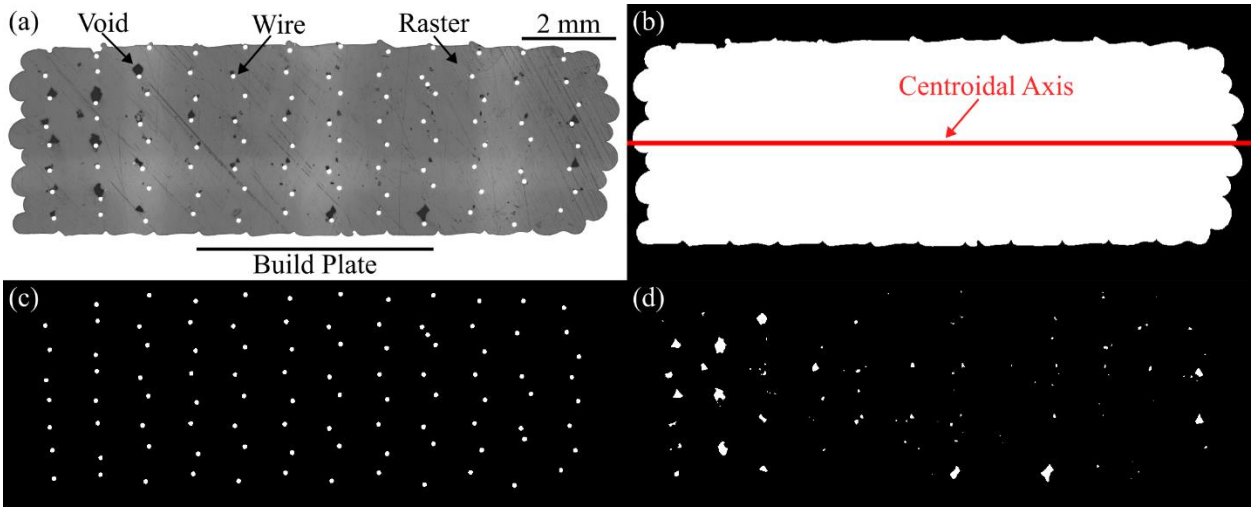

Figure 3-8: Image processing steps: (a) optical microscope image of hot-pressed sample with white background for image processing with subsequent (b) cross-section of sample with centroidal axis highlighted for image processing, (c) segmented image of wires, and (d) segmented image of voids

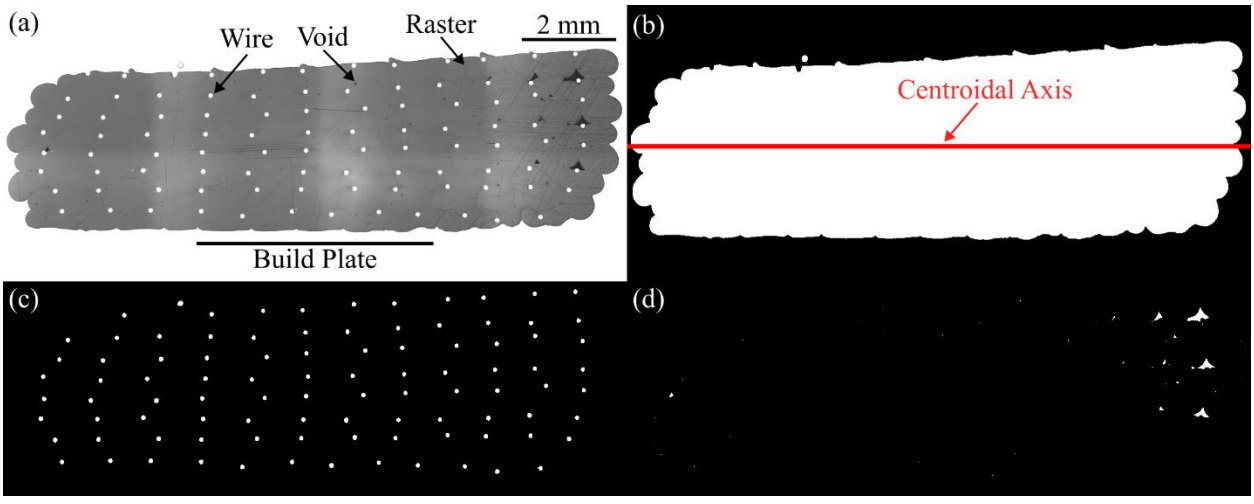

Figure 3-9: Image processing steps: (a) optical microscope image of consolidated sample with white background for image processing with subsequent (b) cross-section of sample with centroidal axis highlighted for image processing, (c) segmented image of wires, and (d) segmented image of voids

The W_{vf} and V_{vf} are given by

$$W_{vf} = \frac{A_w l_w}{n_w A_s l_s} \times 100\% \quad \text{(Eq. 3-6)}$$

$$V_{vf} = \frac{A_v l_s}{A_s l_s} \times 100\% \quad \text{(Eq. 3-7)}$$

where A_w is the total cross-sectional area of the wires from the microscope images, l_w is the length of the wire based on the average wire resistance and resistivity of the wire, n_w is the number of wires in the cross-section, A_s is the cross-sectional area of the sample from the microscope images, l_s is the nominal length of the sample from the standard, and A_v is the total cross-sectional area of the voids from the microscope images. The voids are assumed to be through the length of the sample because the rasters were printed unidirectionally, and no walls were printed along the perimeters of the samples.

3.2.5. Three-Point Flexural Testing

Three-point flexural tests were performed according to ASTM D7264 to obtain the flexural stress–strain graph and determine the flexural strength and stiffness of samples. A support span-to-thickness ratio of 16:1 was used instead of the typical 32:1 [38] to keep the samples within the dimensions of the compacting aluminum plates. Given the sample thickness of 4 mm, the support span was set to 64 mm. The length of the samples was 80 mm, which was approximately 20% longer than the support span length. The samples were placed on the three-point bend fixture and the same UTM (UTM; ElectroPuls E3000, Instron, Massachusetts, United States) was used for consolidation, with a loading rate of 1 mm/min (Figure 3-10).

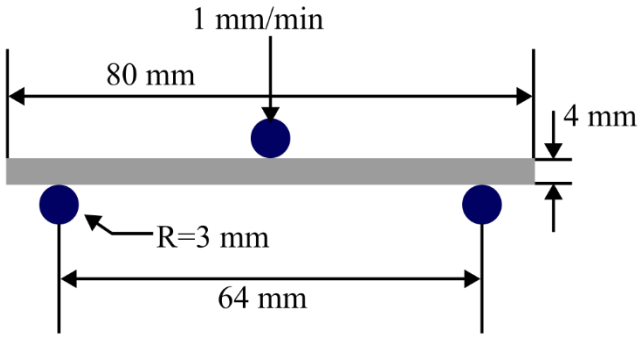

Figure 3-10: Schematic of three-point flexural test setup

The geometric area moment of inertia was calculated for each sample, and the stress was calculated using the flexure formula. The face of the loading nose was painted a flat black, then speckled with white paint by an airbrush. A digital image correlation (DIC) setup was used to track the displacement of the loading nose and was used as the mid-span deflection (Figure 3-15). A LaVision camera (Imager M-Lite 5M, LaVision, Göttingen, Germany) equipped with a 50 mm lens (MVL50M23 50 mm, Navitar, New York, USA) captured images of the flexural test at a frame rate of 5 fps. A working distance of 300 mm between the camera and the loading nose was necessary to yield a 50 mm x 38 mm field of view to capture the loading nose at the beginning and end of the test. LaVision's Davis 10.2.1 software was used to track the location of the speckles on the roller with a subset window and subset size of 29 px and 10 px, respectively.

Assuming the unidirectional samples are orthotropic, the flexural stress and strain were calculated using the homogenous beam theory formulae from ASTM D7264 [38] given by

$$\sigma = \frac{My}{I} \qquad \text{(Eq. 3-8)}$$

$$\epsilon = \frac{6\delta h}{L^2} \qquad \text{(Eq. 3-9)}$$

where M is the bending moment, I is the area moment of inertia, and y is the distance to the neutral axis. For flexural strain, δ is the displacement of the point of maximum deflection, h is the height of the samples, and L is the support span. The DIC results from the displacement of the loading nose was used for δ. The average height and width of each sample type was estimated to be the average minor and major axis lengths of their corresponding sample types given by the regionprops function during the microscope image analysis (Figure 3-7b).

3.3. Results & Discussion

3.3.1. Thermal Model Validation

Due to the one-term approximation relationship used, the analytical model was plotted for Fourier numbers 0.2 and greater, which, for the sample thickness in this study, starts at time t = 15.5 s [40]. Figure 3-11 shows the plot of the analytical model with the experimental results for (a) the 1D conduction thermal model, (b) the resistive heating experimental results, and (c) the consolidation procedure experimental results.

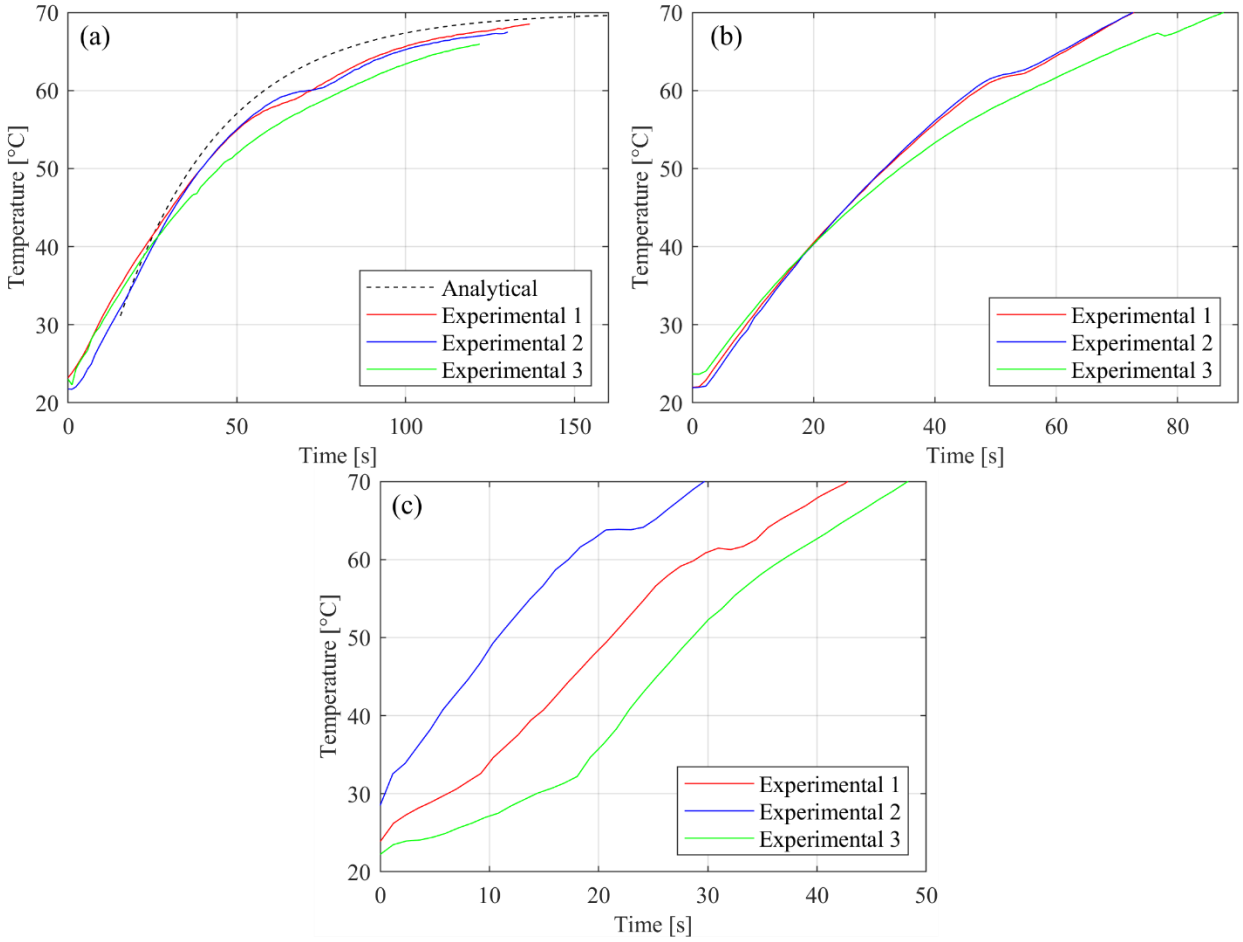

Figure 3-11: (a) 1D conduction analytical model compared with experimental results, (b) resistive heating temperature profile experimental results, and (c) consolidation temperature profile experimental results

The theoretical times for the 1D transient conduction and resistive heating models to reach 65°C were 79.9 s and 76.1 s, respectively. The model for transient conduction underpredicted the results, on average requiring 101.9 s ± 8.9 s. A chi-squared goodness-of-fit test was used to calculate an average root mean squared error of 8.8 s between the analytical and experimental results of the transient conduction model [43]. The discrepancy in the analytical model is due to the assumption that all sample surfaces are held at 70°C from $t = 0$ s. In the experimental setup, 73.7% of the surface area was in contact with the heated platens during the procedure. The time required for resistive heating was shorter than expected, with an average of 63.8 s ± 4.8 s. This

discrepancy is due to the fact that the model applied equal thermal energy in joules from both the 1D transient conduction and resistive heating processes. While the time to heat the samples was assumed to be the same, the temperature response from the resistive heating was more linear and theoretically infinite, as opposed to that of the 1D conduction model, which is asymptotic at the temperature of the platen, 70°C. This means the temperature response, and therefore the time required to reach 65°C, was shorter than the resistive heating model anticipated. The time for the consolidation procedure, using both the 1D transient conduction and resistive heating to heat the sample resulted in a significantly decreased processing time, at an average of 34.7 s ± 8.9 s.

The one-term approximation used to determine the heat transfer by 1D conduction by (Eq. 3-1) assumes all surfaces of the sample are held at a specific temperature from $t = 0$ s. As previously stated, the sides of the sample are not in contact with the plates, causing a discrepancy in the analytical model. The average thickness of samples tested was 4.24 mm. Thinner samples should have higher accuracy compared to the 1D conduction thermal model. Molds where each surface of the sample is heated simultaneously could also be used to increase the accuracy of the 1D conduction thermal model.

3.3.2. Optical Microscopy & Image Processing

To view the images of the cross-sections of different sample types alongside their respective void segmentation, Figure 3-12 displays the images of the different sample types from the optical microscopy at 2.5x magnification. This is to see the difference in void content between sample types more clearly.

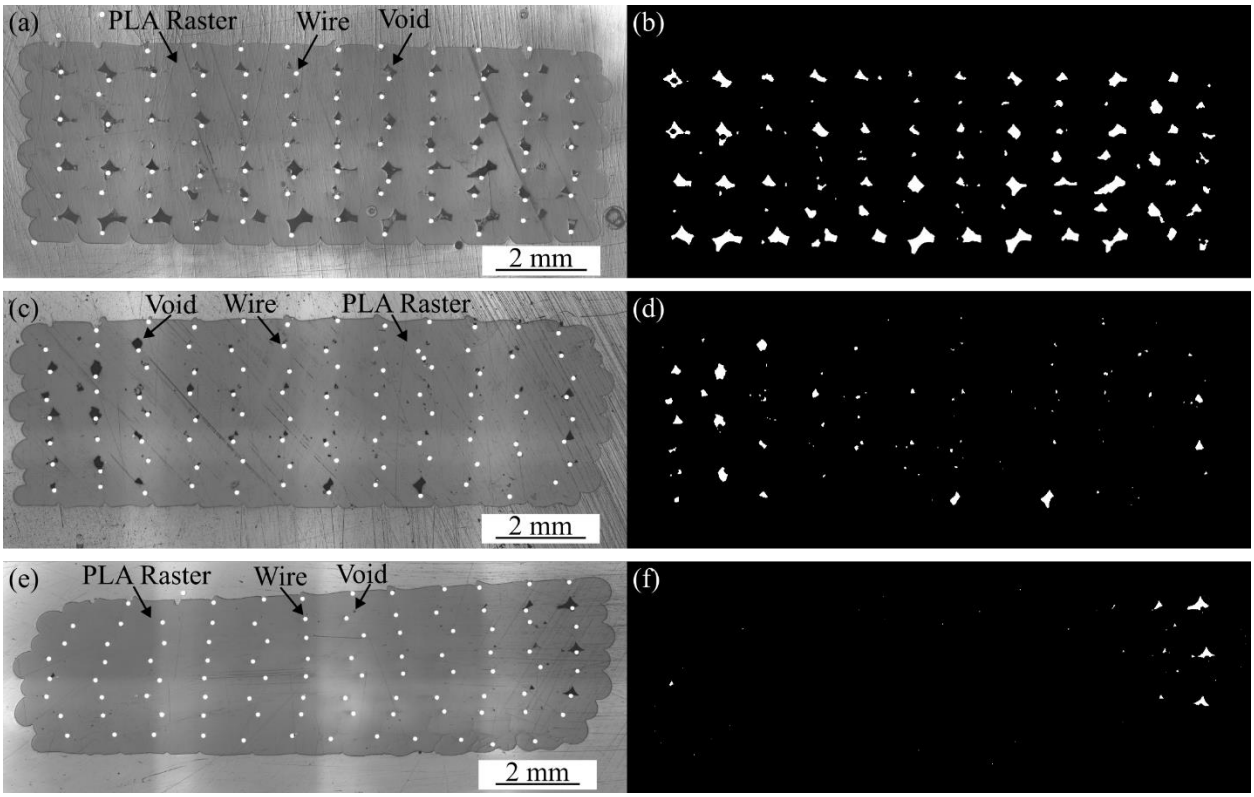

Figure 3-12: Cross-sectional microscope images at 2.5x magnification of samples identifying wires, voids, and polymer rasters: (a) unprocessed sample, (b) unprocessed sample segmented voids, (c) hot-pressed sample, (d) hot-pressed sample segmented voids, (e) consolidated sample, and (f) consolidated sample segmented voids

As seen in Figure 3-12a and Figure 3-12e, the wires shift from being uniformly distributed to shifting in a more random pattern after being subjected to the consolidation procedure because the polymer rasters are in a viscous state. The sample's cross-section is also observed to be non-horizontal due to platen misalignment. These cause an uneven distribution of the load-bearing of a sample with a small wire volume fraction. This low wire volume fraction shows the load is being carried more by the matrix material, and random wire distribution transfers more load distribution to the matrix than a more evenly distributed wire pattern, which can cause lower strength and stiffness. Molds or other lateral confinement tools could prevent the wires from shifting by keeping the viscous polymer raster in place to maintain the cross-sectional geometry, while improving the platen alignment using linear rails to maintain a consistent pressure across

the top of the sample would improve the mechanical properties by providing an even surface for even load distribution across the width of the sample during flexural testing.

The values for the wire volume and void volume were calculated from the MATLAB image processing results. These were divided by the volume of the composite, based on the measured dimensions of the samples, to find the average W_{vf} and V_{vf} of the three microscope samples per sample type.

Table 3-3: Average volume fractions with standard deviation of CWPC samples

Sample Type	W_{vf} **(%)**	V_{vf} **(%)**
A (Unprocessed)	1.18 ± 0.17	5.24 ± 2.67
B (Hot-Pressed)	1.17 ± 0.09	1.89 ± 1.57
C (Consolidated)	1.25 ± 0.01	0.44 ± 0.12

The cross-sectional areas of the samples were reduced by 2.1% and 5.0% after the hot-pressing and consolidation, respectively. Table 3-3 shows that the void volume fraction is decreased on average by 63.9% and 91.6% because of the hot-pressing and consolidation, respectively. Different examples in the literature show a V_{vf} of between 2.01% and 24% [16], [19], [20], [22]. The V_{vf} of the unprocessed samples in this study was found to be 5.24%. Hot-pressing of the samples yielded a lower V_{vf} of 1.89%. However, the consolidation procedure developed in this study decreased the V_{vf} to 0.44% while requiring less cycle time than hot-pressing.

To quantify the void change and the size of the voids through the thickness of the sample, the centroidal axis was used as a reference point, as shown in Figure 3-7b. Regionprops was used to determine the coordinates of the centroid of each void. The y-coordinate of the void centroid was subtracted from the centroidal axis y-coordinate to determine the distance between the two;

negative values indicate voids below the centroidal axis. Figure 3-13 shows the results of the cross-sectional areas of the voids relative to their distance from the centroidal axis of the sample.

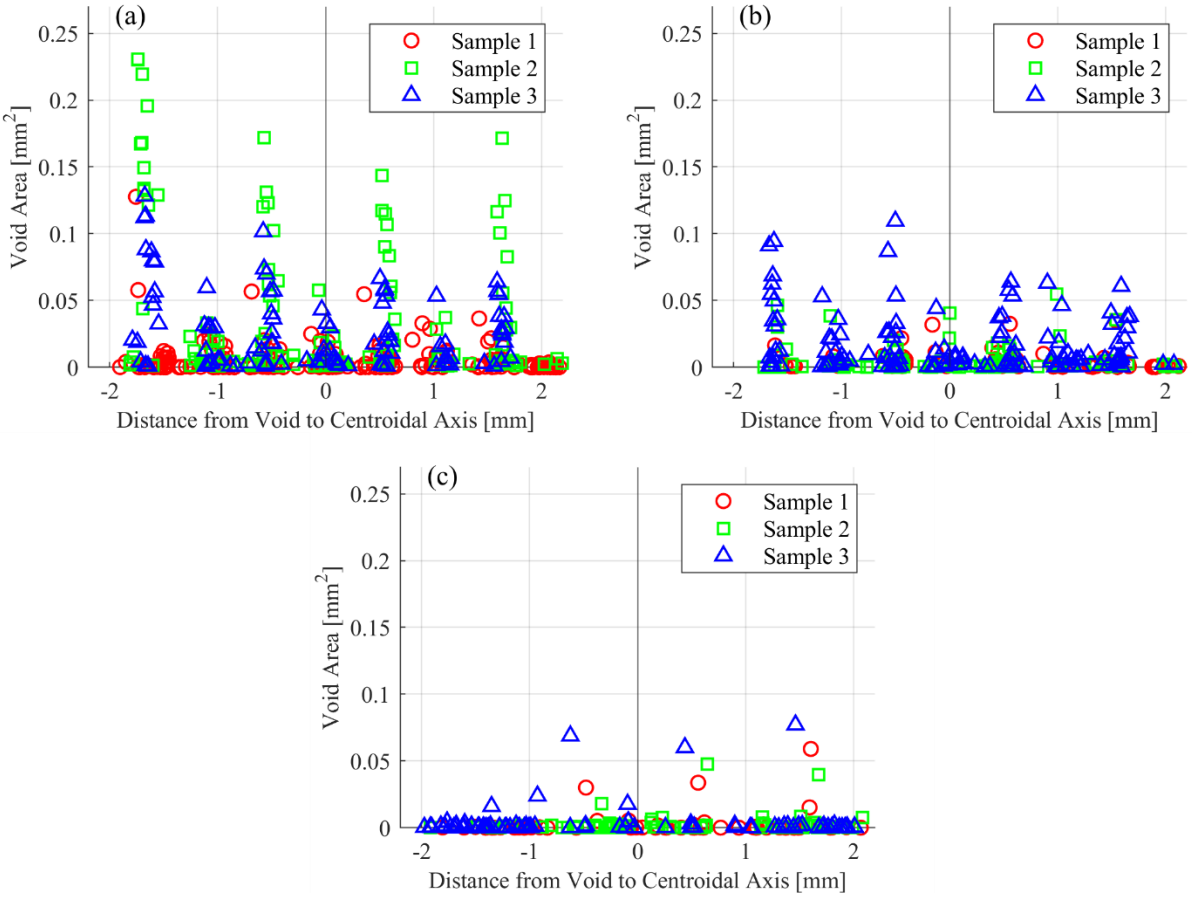

Figure 3-13: Void area vs the distance from the centroidal axis for: (a) unprocessed samples, (b) hot-pressed samples, and (c) consolidated samples

Figure 3-13 shows that the voids drastically decrease in size after hot-pressing and consolidation; the largest decrease is after consolidation where most voids are below 0.01 mm^2. Unprocessed samples contained the highest void content with the highest standard deviation, with an average void size of 0.021 mm^2 ± 0.016 mm^2. Hot-pressing decreases voids to be more uniform, with an average size of 0.011 mm^2 ± 0.006 mm^2, while consolidation showed the lowest average void size and standard deviations of 0.004 mm^2 ± 0.002 mm^2. On average, the largest voids in unprocessed samples are seen in the first layer, between 1.5 mm and 2 mm below the centroidal

axis, with a weighted average size of 0.059 mm^2 ± 0.049 mm^2. Hot-pressed samples have the highest void content in the first layer on average as well, with a weighted average of 0.025 mm^2 ± 0.024 mm^2, while the average largest voids in consolidated samples are in the third layer, between 0.5 mm and 1 mm below the centroidal axis, with a weighted average of 0.007 mm^2 ± 0.021 mm^2.

Table 3-4: Weighted mean of void area [mm^2], relative to layer number with standard deviation

Layer #	Sample Type A Void Area [mm^2]	Sample Type B Void Area [mm^2]	Sample Type C Void Area [mm^2]
1	0.059 ± 0.049	0.025 ± 0.024	0.001 ± 0.001
2	0.010 ± 0.011	0.009 ± 0.013	0.001 ± 0.003
3	0.021 ± 0.030	0.012 ± 0.021	0.007 ± 0.021
4	0.014 ± 0.018	0.009 ± 0.013	0.003 ± 0.007
5	0.007 ± 0.010	0.008 ± 0.011	0.005 ± 0.020
6	0.027 ± 0.026	0.012 ± 0.019	0.005 ± 0.003
7	0.006 ± 0.011	0.006 ± 0.010	0.003 ± 0.019
8	0.024 ± 0.022	0.010 ± 0.014	0.004 ± 0.004

In the literature, void volume fraction can vary depending on factors such as nozzle diameter, flow rate, and the diameter of reinforcement wire, with different studies achieving a V_{vf} of between 2.01% and 24%. Figure 3-14 shows the V_{vf} for unprocessed, hot-pressed, and consolidated samples compared with those found in the literature.

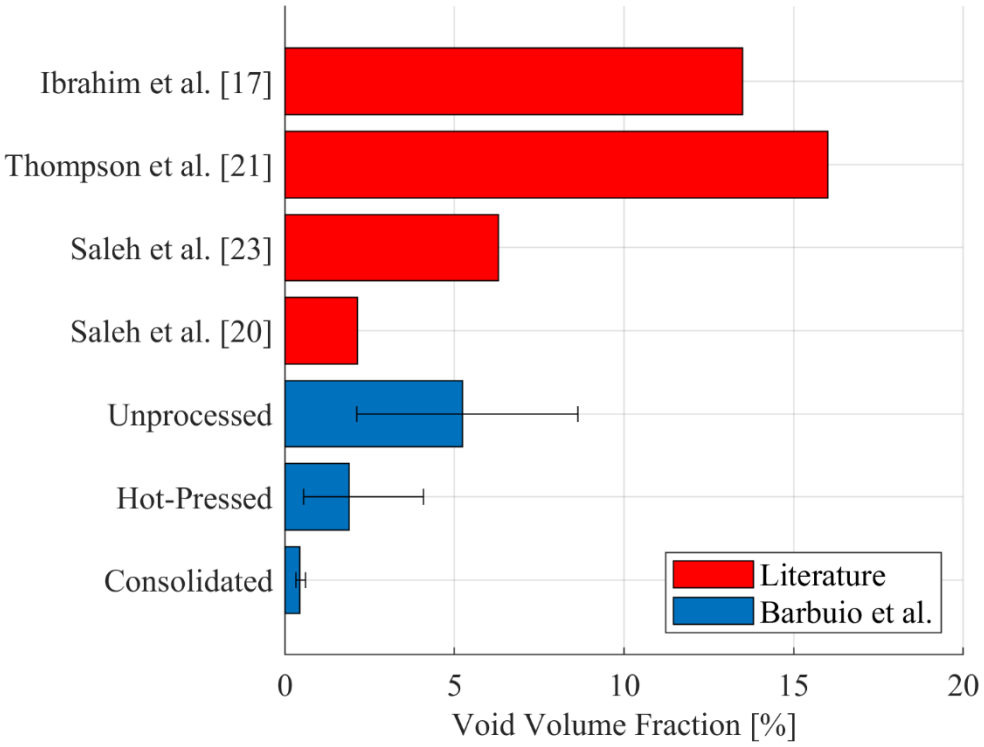

Figure 3-14: Comparison of V_{vf} % from different sample types to V_{vf} % in literature

Figure 3-14 demonstrates the stark difference in V_{vf} as a result of the consolidation procedure. The V_{vf} was found to be 0.44%. It is observed that the consolidation procedure also yields lower variation in V_{vf} compared to hot-pressing, which can result in a temperature gradient through the thickness of the sample due to being heated externally, which is mitigated during consolidation due to the uniform internal heating. This shows results comparable to other thermoplastic composite manufacturing techniques such as AFP and compression molding [44], [45].

3.3.3. Three-Point Flexural Testing

The load-displacement results were obtained from the DIC analysis. The displacement of the point of maximum deflection was determined using the displacement of the loading nose (Figure 3-15).

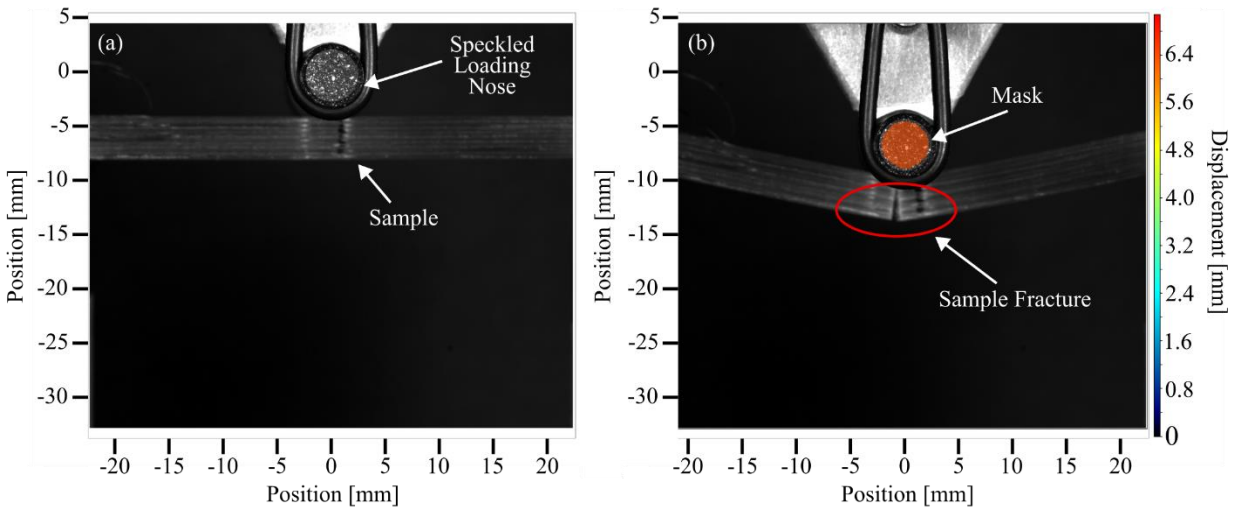

Figure 3-15: DIC analysis used to obtain displacement of load roller: (a) speckled loading nose and sample before flexural testing and (b) fractured sample and coloured displacement

Figure 3-16 displays the flexural stress–strain curves for the unprocessed, hot-pressed, and consolidated samples.

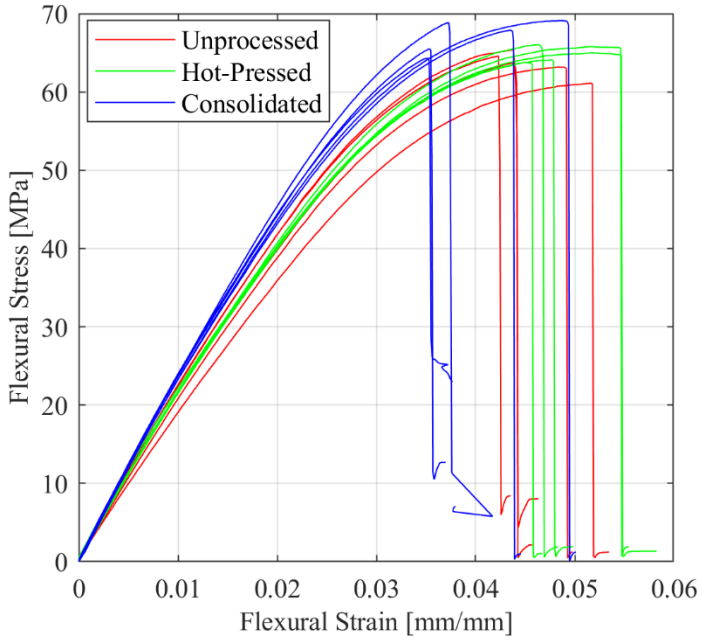

Figure 3-16: Flexural stress-strain curves for unprocessed, hot-pressed, and consolidated samples

The consolidated samples displayed the largest increase in flexural strength and stiffness compared with the unprocessed samples. ASTM D7264 recommends the flexural chord modulus

be taken as the slope of the linear portion of the graph, between the strain ranges 0.001 mm/mm and 0.003 mm/mm. The flexural strength was determined to be the maximum of the plot for each sample. From Figure 3-16, it can be seen that the consolidated samples are stiffer and fail at a higher stress but a lower strain value, while hot-pressed and unprocessed samples have lower strength and stiffness and fail at higher strains. Table 3-5 shows the results for the flexural modulus and flexural strength.

Table 3-5: Average three-point flexural test results with standard deviation based on sample type

Sample Type	**Average Flexural Modulus [GPa]**	**Average Flexural Strength [MPa]**
A (Unprocessed)	2.20 ± 0.18	64 ± 1
B (Hot-Pressed)	2.26 ± 0.07	65 ± 1
C (Consolidated)	2.47 ± 0.02	67 ± 2

Samples that were subjected to the consolidation procedure had an average flexural strength of 67 MPa and flexural modulus of 2.47 GPa, a 5% and a 12% increase from unprocessed samples in flexural strength and stiffness, respectively. The bending stiffness, *EI*, of the CWPCs were also observed to be 7.4% and 16.2% lower for hot-pressed and consolidated samples, respectively, compared to unprocessed samples. As previously discussed, the non-uniformity of the wire distribution in the cross-section in hot-pressed and consolidated samples (Figure 3-12) also decrease the flexural strength and stiffness by causing uneven distribution of the load-bearing to the polymer matrix, which can cause premature failure as the wires are supporting less loading than if they were uniform throughout the cross-section of the hot-pressed and consolidated specimens. The non-horizontal surface of consolidated specimens as a result of platen misalignment could have also caused an underprediction in flexural results, as the loading nose applied uneven load to the sample surface during flexural testing.

A one-way analysis of variance (ANOVA) test was performed to determine the statistical significance of flexural properties between sample types with a 95% confidence interval [43]. A *P* -value less than 0.05 states that the null hypothesis (H_0) is false. For this test, H_0 states that there is no statistically significant difference between the average flexural modulus and strength values between sample types. The results show a *P* -value less than 0.05 for both flexural strength and flexural modulus with *P* -values of 0.0127 and 0.0164, respectively. These results reject the null hypothesis, meaning there is a statistically significant difference between the flexural modulus and flexural strength after processing. Subsequent tests were performed using the Tukey–Kramer method of multiple comparisons to determine the statistical significance in flexural properties between each sample type, with a 95% confidence interval. The flexural modulus and flexural strength statistical results can be seen in Table 3-6.

Table 3-6: Results of Tukey-Kramer method of multiple comparisons—flexural modulus and flexural strength results

Flexural Property	**Sample 1**	**Sample 2**	**Lower Limit**	**A-B**	**Upper Limit**	***P* -value**
Flexural Modulus	Unprocessed	Hot-Pressed	-0.2708	-0.0626	0.1457	0.7090
	Unprocessed	Consolidated	-0.4756	-0.2674	-0.0592	**0.0129**
	Hot-Pressed	Consolidated	-0.4131	-0.2048	0.0034	0.0540
Flexural Strength	Unprocessed	Hot-Pressed	-4.1402	-1.3557	1.4288	0.4223
	Unprocessed	Consolidated	-6.3394	-3.5549	-0.7705	**0.0134**
	Hot-Pressed	Consolidated	-4.9837	-2.1993	0.5852	0.1300

The results from the multiple comparison tests showed a statistically significant increase in flexural strength by 5% and 12% increase in flexural modulus due to the consolidation procedure. Further, there is no statistically significant difference between the results of the unprocessed and hot-pressed samples or the hot-pressed and consolidated samples. In other

words, hot-pressing does not have a statistically significant effect on the flexural strength and stiffness of the samples, but consolidation statistically significantly improves the flexural strength and stiffness of the samples by 5% and 12%.

The increase in flexural properties is due to the decrease in V_{vf}, leading to an improved bonding between the reinforcement wires and the PLA matrix, consistent with other studies [33], [37-39]. The W_{vf} remains consistent and relatively low, indicating the PLA matrix still carries the majority of the load. A study on the crystallinity of the PLA matrix was carried out in a DSC machine (Discovery DSC 250, TA Instruments, Delaware, United States) by applying a heating cycle according to ASTM D3418-21 [39]. A 5 mg sample was cut off from microscopy samples of each sample type (A, B and C). The DSC samples were heated from 26 °C to 215 °C at a rate of 10 °C/min in a nitrogen atmosphere. The crystallinity of the polymer matrix was calculated as done by van de Werken *et al.* [35] using

$$X_C(\%) = \frac{\Delta H_m - \Delta H_{cc}}{\Delta H^\circ_f (1 - W_f)} \times 100 \qquad \text{(Eq. 3-10)}$$

where ΔH_m is the enthalpy of melting, ΔH_{cc} is the enthalpy of cold crystallization, both found in the TRIOS software using peak to peak integration of the melting and cold crystallization peaks. ΔH°_f is the theoretical enthalpy of fusion for 100% crystalline PLA (93.7 J/g) [46] and W_f is the weight fraction of the wire reinforcement. The crystallinity of the unprocessed sample, hot-pressed sample, and consolidated sample were 9%, 15% and 18%, respectively. Post-processing treatment increased the crystallinity of the PLA matrix, which reduced ductility and toughness of the PLA matrix. This agrees with a study performed by Ghasemkhani *et al.* [46], where the effects of the annealing were observed to display similar behaviour.

The flexural strength results from this study are lower in comparison with the results from Ibrahim *et al.* [16] (Figure 3-17). Their results showed a 90 MPa and 70 MPa ultimate flexural strength for samples with W_{vf} values of 1.7% and 0.68%, respectively. However, it is difficult to compare these results directly, because the two studies were performed according to different ASTM standards, for polymer matrix composites and unreinforced and reinforced plastics, respectively. (The current study used ASTM D7264, and Ibrahim *et al.* [16] used ASTM D790.) The two studies used different support span ratios, with the latter calculating flexural stress based on a large support span ratio.

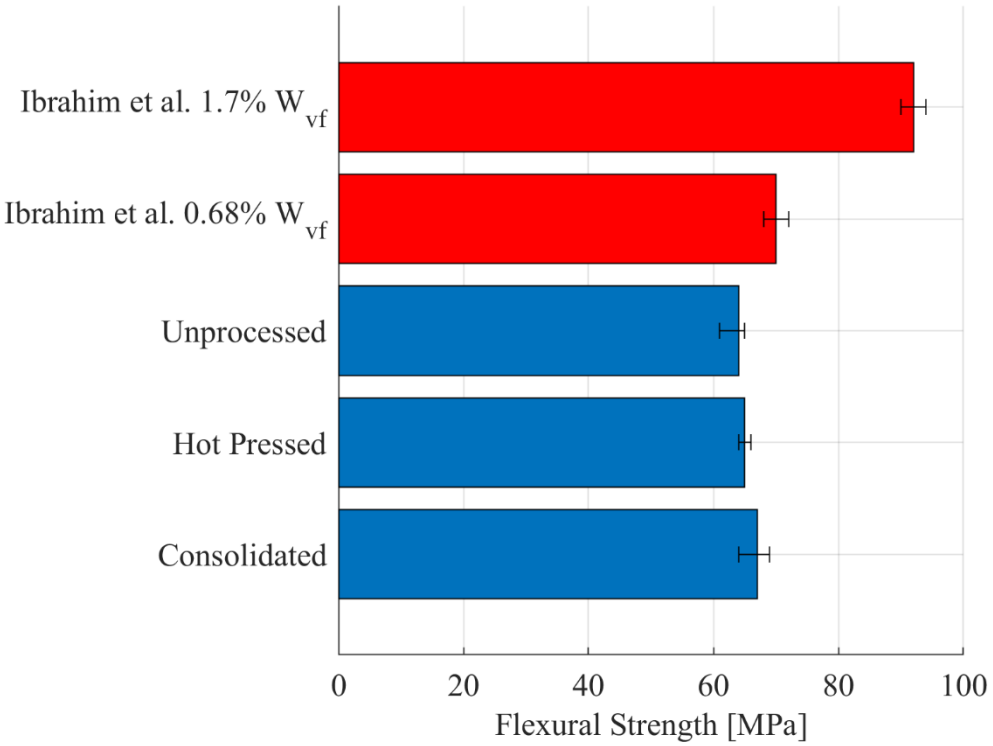

Figure 3-17: Flexural strength comparison between the current study and results from Ibrahim et al. [16]

3.4. Conclusion

This study developed a consolidation procedure which utilized resistive heating and hot-pressing for composite manufacturing for the reduction of voids in CWPC samples. Thermal models were created and validated to estimate the consolidation procedure parameters. Testing of samples with embedded thermocouples showed the modelling was close to the experimental results. Three-point flexural tests were performed to determine the flexural strength and stiffness. Samples were 3D printed with a continuous nickel–chromium wire, with a 1.18% wire volume fraction. Microscope image analysis showed a significant decrease in void volume fraction, 63.9% and 91.6%, after hot-pressing and consolidation, respectively. This study shows the consolidation procedure drastically reduces void content, yielding void volume fractions in the 3D-printed specimens of 0.44%. The consolidated samples displayed the most significant increase in flexural properties, with a 5% and 12% increase in flexural strength and modulus, respectively. Statistical analysis showed the consolidation procedure has a statistically significant positive impact on the flexural properties of the samples. This study focused on NiCr resistive wire as the reinforcement material with a relatively low wire volume fraction. Multidirectional 3D-printed composite laminates are at higher risk of premature failure when subjected to loads due to the anisotropy of the reinforcement material. The consolidation procedure could be used to reduce the crack initiation sites within CWPC laminates to increase the potential for more than just unidirectional printing. Composite 3D printing has a wide range of applications including structural health monitoring and other sensing applications. The consolidation procedure increases the wire-polymer adhesion and could result in higher accuracy when used for in-part sensing, including for wearable sensors which experience combined loading. Future work could also focus on the consolidation of continuous reinforcement in 3D-printed composites for

reinforcement materials with high electrical resistance such as other metal wires or synthetic fibres such as carbon and aramid, with larger fibre volume fractions, leading to a larger increase in mechanical properties after the consolidation procedure.

3.5. References

[1] B. Tyagi, · Rajkumar Velu, and A. Raj, “Failure analysis and statistical validation of fused filament fabricated PETG composite for transtibial prosthetics,” Progress in Additive Manufacturing 2025, pp. 1–26, May 2025, doi: 10.1007/S40964-025-01113-5.

[2] K. Yadav and V. Tiwari, “Effects of voids on mechanical response and failure behaviour of additively manufactured Onyx,” Progress in Additive Manufacturing, pp. 1–30, May 2025, doi: 10.1007/S40964-025-01139-9/FIGURES/21.

[3] P. Wang et al., “Preparation of short CF/GF reinforced PEEK composite filaments and their comprehensive properties evaluation for FDM-3D printing,” Compos B Eng, vol. 198, p. 108175, Oct. 2020, doi: 10.1016/J.COMPOSITESB.2020.108175.

[4] “Industrial Additive Manufacturing Platform | Markforged.” Accessed: Jan. 22, 2025. [Online]. Available: https://markforged.com/

[5] “9T Labs - Make your products strong, lightweight and sustainable like never before.” Accessed: Jan. 22, 2025. [Online]. Available: https://www.9tlabs.com/

[6] “Anisoprint - Continuous fiber 3D printing for manufacturing of optimal composites.” Accessed: Jan. 22, 2025. [Online]. Available: https://anisoprint.com/

[7] M. Araya-Calvo et al., “Evaluation of compressive and flexural properties of continuous fiber fabrication additive manufacturing technology,” Addit Manuf, vol. 22, pp. 157–164, Aug. 2018, doi: 10.1016/J.ADDMA.2018.05.007.

[8] G. W. Melenka, B. K. O. Cheung, J. S. Schofield, M. R. Dawson, and J. P. Carey, “Evaluation and prediction of the tensile properties of continuous fiber-reinforced 3D printed structures,” Compos Struct, 2016, doi: 10.1016/j.compstruct.2016.07.018.

[9] M. A. Saleh, S. Olcun, M. Karam, R. Kempers, and G. W. Melenka, “High stiffness 3D-printed continuous pitch carbon fiber reinforced polymer composites,” J Compos Mater, vol. 58, no. 16, pp. 1873–1886, Jul. 2024, doi: 10.1177/00219983241249526.

[10] Y. Chen, A. Klingler, K. Fu, and L. Ye, “3D printing and modelling of continuous carbon fibre reinforced composite grids with enhanced shear modulus,” Eng Struct, vol. 286, Jul. 2023, doi: 10.1016/j.engstruct.2023.116165.

[11] F. Liu, E. Ferraris, and J. Ivens, “Mechanical investigation and microstructure performance of a two-matrix continuous carbon fibre composite fabricated by 3D printing,” J Manuf Process, vol. 79, pp. 383–393, Jul. 2022, doi: 10.1016/J.JMAPRO.2022.04.050.

[12] S. S. Kumar, J. S. Akmal, and M. Salmi, “4D printing of shape memory polymer with continuous carbon fiber,” Progress in Additive Manufacturing, vol. 9, no. 6, pp. 1985–1995, Dec. 2023, doi: 10.1007/S40964-023-00553-1/TABLES/2.

[13] M. K. Idris, P. Naderi, G. W. Melenka, and G. Grau, “Damage location sensing in carbon fiber composites using extrusion printed electronics,” Functional Composites and Structures, vol. 3, no. 4, Dec. 2021, doi: 10.1088/2631-6331/AC3731.

[14] S. Olcun, A. Elkholy, and R. Kempers, “High thermal conductivity continuous pitch carbon fiber 3D printed using a 6-axis robot arm,” Progress in Additive Manufacturing, vol. 9, no. 6, pp. 2189–2198, Dec. 2024, doi: 10.1007/S40964-024-00568-2/FIGURES/7.

[15] Y. Ibrahim, G. W. Melenka, and R. Kempers, “Additive manufacturing of Continuous Wire Polymer Composites,” Manuf Lett, vol. 16, pp. 49–51, Apr. 2018, doi: 10.1016/J.MFGLET.2018.04.001.

[16] Y. Ibrahim, G. W. Melenka, and R. Kempers, “Flexural properties of three-dimensional printed continuous wire polymer composites,” Materials Science and Technology (United Kingdom), vol. 35, no. 12, pp. 1471–1482, Aug. 2019, doi: 10.1080/02670836.2019.1630085.

[17] Y. Ibrahim, R. Kempers, and A. Amirfazli, “3D printed electro-thermal anti-or de-icing system for composite panels,” Cold Reg Sci Technol, 2019, doi: 10.1016/j.coldregions.2019.102844.

[18] Y. Ibrahim and R. Kempers, “Effective thermal conductivity of 3D-printed continuous wire polymer composites,” Progress in Additive Manufacturing, vol. 7, no. 4, pp. 699–712, Aug. 2022, doi: 10.1007/S40964-021-00256-5/FIGURES/12.

[19] M. A. Saleh, R. Kempers, and G. W. Melenka, “3D printed continuous wire polymer composites strain sensors for structural health monitoring,” Smart Mater Struct, 2019, doi: 10.1088/1361-665X/aafdef.

[20] C. Thompson, C. González, and J. LLorca, “Material extrusion fabrication of continuous metal wire-reinforced polymer–matrix composites,” Composites Communications, vol. 50, p. 102024, Oct. 2024, doi: 10.1016/J.COCO.2024.102024.

[21] B. Akhoundi, “An evaluation of the shape-memory behavior and mechanical properties of polylactic acid/Ni80Cr20 continuous wire composite produced by extrusion-based additive manufacturing and in-melt simultaneous impregnation method,” Journal of Reinforced Plastics and Composites, vol. 43, no. 13–14, pp. 783–797, Jul. 2024, doi: 10.1177/07316844231197036.

[22] M. A. Saleh, R. Kempers, and G. W. Melenka, “A comparative study on the electromechanical properties of 3D-Printed rigid and flexible continuous wire polymer composites for structural health monitoring,” Sensors and Actuators A, vol. 328, p. 112764, 2021, doi: 10.1016/j.sna.2021.112764.

[23] M. Mehdikhani, L. Gorbatikh, I. Verpoest, and S. V. Lomov, “Voids in fiber-reinforced polymer composites: A review on their formation, characteristics, and effects on mechanical performance,” J Compos Mater, vol. 53, no. 12, pp. 1579–1669, May 2019, doi: 10.1177/0021998318772152/ASSET/IMAGES/LARGE/10.1177_0021998318772152-FIG20.JPEG.

[24] H. J. O’Connor and D. P. Dowling, “Low-pressure additive manufacturing of continuous fiber-reinforced polymer composites,” Polym Compos, vol. 40, no. 11, pp. 4329–4339, Nov. 2019, doi: 10.1002/PC.25294;REQUESTEDJOURNAL:JOURNAL:15480569;WGROUP:STRING:PUBLICATION.

[25] A. Uşun, B. B. Vatandaş, and R. Gümrük, “Enhanced mechanical properties of continuous carbon fiber reinforced polyether-ether-ketone composites via infrared preheating and high fiber volume fraction,” Addit Manuf, vol. 89, p. 104289, Jun. 2024, doi: 10.1016/J.ADDMA.2024.104289.

[26] Z. Tang, L. Guo, Z. Li, K. Huang, T. Zheng, and R. Sun, “A comparative study of void characteristics on the mechanical response of unidirectional composites,” Mechanics of Materials, vol. 174, p. 104456, Nov. 2022, doi: 10.1016/J.MECHMAT.2022.104456.

[27] K. Rodzeń, E. Harkin-Jones, M. Wegrzyn, P. K. Sharma, and A. Zhigunov, “Improvement of the layer-layer adhesion in FFF 3D printed PEEK/carbon fibre composites,” Compos Part A Appl Sci Manuf, vol. 149, p. 106532, Oct. 2021, doi: 10.1016/J.COMPOSITESA.2021.106532.

[28] J. Xiang et al., “Effect of heat-treatment on compressive response of 3D printed continuous carbon fiber reinforced composites under different loading directions,” J Appl Polym Sci, vol. 140, no. 3, p. e53330, Jan. 2023, doi: 10.1002/APP.53330.

[29] M. Y. Ali, G. K. M. Rao, and B. A. Prasad, “Experimental investigation of influence of post-processing variables on mechanical strength and surface quality of 3D printed carbon fiber reinforced polylactic acid samples,” Progress in Additive Manufacturing 2025, pp. 1–13, Feb. 2025, doi: 10.1007/S40964-025-01023-6.

[30] S. Valvez, P. N. B. Reis, and J. A. M. Ferreira, “Effect of annealing treatment on mechanical properties of 3D-Printed composites,” Journal of Materials Research and Technology, vol. 23, pp. 2101–2115, Mar. 2023, doi: 10.1016/J.JMRT.2023.01.097.

[31] X. Sun, M. Mazur, and C.-T. Cheng, “An interlaced toolpath strategy for void reduction in material extrusion additive manufacturing,” Progress in Additive Manufacturing 2025, pp. 1–17, May 2025, doi: 10.1007/S40964-025-01163-9.

[32] Z. Ouyang, L. Yang, Z. Pi, Z. Wang, C. Yan, and Y. Shi, “Robot-assisted laser additive manufacturing for high-strength/low-porosity continuous fiber-reinforced thermoplastic composites,” Compos Sci Technol, vol. 247, p. 110397, Mar. 2024, doi: 10.1016/J.COMPSCITECH.2023.110397.

[33] T. Yiwen, T. Yuegang, Z. Fan, and Z. Jun, “Laser assisted rapid 3D printing of continuous carbon fiber reinforced plastics: Simulation, characterization, and properties,” Polym Compos, vol. 44, no. 6, pp. 3084–3094, Jun. 2023, doi: DOI:10.1002/pc.27303.

[34] Y. Asano, M. Ueda, M. Yamawaki, R. Matsuzaki, A. Le Duigou, and M. Castro, “Layer-wise compaction 3D printing: void reduction and interfacial enhancement for continuous carbon fiber–reinforced thermoplastics,” Advanced Composite Materials, pp. 1–15, Feb. 2025, doi: 10.1080/09243046.2025.2459672.

[35] N. van de Werken, P. Koirala, J. Ghorbani, D. Doyle, and M. Tehrani, “Investigating the hot isostatic pressing of an additively manufactured continuous carbon fiber reinforced PEEK composite,” Addit Manuf, vol. 37, p. 101634, 2021, doi: 10.1016/j.addma.2020.101634.

[36] M. Kashfi and M. Tehrani, “Effects of void content on flexural properties of additively manufactured polymer composites,” Composites Part C: Open Access, Jul. 2021, doi: 10.1016/j.jcomc.2021.100173.

[37] A. Gleadall, “FullControl GCode Designer: Open-source software for unconstrained design in additive manufacturing,” Addit Manuf, vol. 46, p. 102109, Oct. 2021, doi: 10.1016/J.ADDMA.2021.102109.

[38] ASTM International, “Standard Test Method for Flexural Properties of Polymer Matrix Composite Materials,” 2007, ASTM D 7264/D 7264M-07, \: add. doi: 10.1520/D7264_D7264M-21.

[39] ASTM International, “Standard Test Method for Transition Temperatures and Enthalpies of Fusion and Crystallization of Polymers by Differential Scanning Calorimetry,” 2024, ASTM D3418-21. doi: 10.1520/D3418-21.

[40] Y. A. Çengel and A. J. Ghajar, Heat and Mass Transfer Fundamentals & Applications, 6th ed. McGraw-Hill Education, 2020.

[41] O. Zmeskal, L. Marackova, T. Lapcikova, P. Mencik, and R. Prikryl, “Thermal properties of samples prepared from polylactic acid by 3D printing,” AIP Conf Proc, vol. 2305, no. 1, Nov. 2020, doi: 10.1063/5.0033857/740039.

[42] “EVANOHM ALLOY S Filing Code: Nickel Alloy.”

[43] W. Navidi, Statistics for Engineers and Scientists. New York, NY: McGraw Hill, 2006.

[44] M. John and R. V. Prakash, “Void content measurement in fiber reinforced plastic composites by X-ray computed tomography,” Materials Science Forum, vol. 928 MSF, pp. 38–44, 2018, doi: 10.4028/WWW.SCIENTIFIC.NET/MSF.928.38.

[45] E. Oromiehie, B. Gangadhara Prusty, P. Compston, and G. Rajan, “Automated fibre placement based composite structures: Review on the defects, impacts and inspections techniques,” Compos Struct, 2019, doi: 10.1016/j.compstruct.2019.110987.

[46] A. Ghasemkhani, G. Pircheraghi, N. Rashidi Mehrabadi, and A. Eshraghi, “Effects of heat treatment on the mechanical properties of 3D-printed polylactic acid: Study of competition between crystallization and interlayer bonding,” Mater Today Commun, vol. 39, p. 109266, Jun. 2024, doi: 10.1016/J.MTCOMM.2024.109266.

Chapter 4 - Mechanical Properties of Cross-Ply and Unidirectional 3D-Printed Continuous Wire Polymer Composites

4.1. Introduction

Fused filament fabrication (FFF) 3D printing has seen a widespread use in the rapid prototyping industry, as it can manufacture geometrically complex plastic parts quickly, and with less material waste than subtractive machining methods. However, it is still mainly used for the prototyping of functional parts, as FFF 3D-printed parts have low strength. This lack of strength is a result of the printing process, which deposits a molten polymer raster layer-by-layer to form the required shape [1]. The nature of the raster deposition process during FFF 3D printing causes the presence of voids between rasters in the 3D-printed parts [2]. Printing parameters that directly effect the raster size and pattern cause decreased bonding between rasters, altering the mechanical properties of 3D-printed parts [1], [3], [4]. Namely, the raster orientation of FFF 3D-printed parts plays a significant role in their mechanical properties such as transverse strength and interlaminar shear strength and causes 3D-printed samples to behave anisotropically [5-7]. The anisotropy of 3D-printed materials has been studied extensively to better understand the limitations of FFF 3D-printed parts. A study by Allum *et al.* [8] compared the bulk material strength of 3D-printed polylactic acid (PLA) samples with 3D-printed longitudinal (rasters parallel to loading) and transverse (rasters perpendicular to loading) specimens and compared their experimental results with the mechanical properties of the bulk PLA material. They found that insufficient bonding between transverse layers resulted in lower strength compared with

longitudinally oriented rasters and a noticeable difference between the strength of the printed sample and the bulk material strength. For samples printed in the transverse direction, the material decreases strength due to the incomplete bonding of the rasters. Fayazbakhsh *et al.* [9] performed a study on 3D-printed PLA samples according to ASTM D638-14 and determined longitudinal samples had a 60.8%, 7.6%, and 52.1% higher tensile strength, modulus and strain at failure than transverse samples.

The 3D printing of continuous fibre polymer composites (CFRPCs), is effective in depositing the continuous fibre reinforcement material in a pre-determined pattern to increase the strength in multiple loading directions [10-12]. While synthetic fibres are a commonly researched material in 3D printing, they can be expensive and difficult to print without commercial 3D printers. Continuous wire polymer composites (CWPCs) have been used in recent studies, using customized low-cost desktop 3D printers, either by co-extruding through one nozzle, or using a multi-nozzle extrusion system to choose the layers which are reinforced with a metallic wire. CWPCs have shown a significant increase in strength and stiffness, as opposed to a 3D-printed polymer part [13], [14]. The continuity of the metal reinforcement wire has allowed these CWPCs to be used in sensing applications for structural health monitoring and shape memory characteristics. Saleh *et al.* [15-17] used unidirectional continuous copper wire as reinforcement in polylactic acid (PLA) and thermoplastic polyurethane (TPU). The change in the resistance of the continuous copper wire was monitored during electro-mechanical testing, which allowed the CWPCs to be used for structural health monitoring. However, most studies on CWPCs have only printed the reinforcement wire in the longitudinal direction. Few instances in the literature have shown the multidirectional printing of CPWC laminates [18], [19]. Recently, García de la Camacha *et al.* [19] studied longitudinal, transverse, $[\pm 45°]_S$ and quasi isotropic $[0°/90°/\pm 45°]_S$

aluminum wire-reinforced 3D-printed composites and found unidirectional CWPCs with the aluminum wires oriented in the longitudinal orientation were stronger, as expected. Their results showed low adhesion between the PLA matrix and aluminum wire, which caused early failure when the wires were not oriented in the loading direction.

In CWPCs, several studies in literature take note of voids and refer to high void volume fraction (V_{vf}) as a source of potential premature failure and namely point out decreased wire-raster adhesion as an issue [13-17], [19-21]. Void reduction in polymer composites with continuous fibre or wire reinforcement can be achieved in-situ, or in post-processing. In-situ methods typically require custom 3D printing equipment. For example, studies have used consolidation rollers to compact the sample during printing, lasers, or infrared heating of the rasters as they print [22-26]. Elderfield *et al.* [27] performed discrete in-situ consolidation (DISC) of continuous carbon fibre-reinforced samples, which used a custom consolidation tool that followed the printer nozzle as the material was deposited. They found that samples not printed using the DISC process had void content of 40.4%, while after DISC, void content was 3.8%. In-situ methods are shown to be quite effective; however, it requires custom equipment and specific part geometry in order to perform the layer-by-layer consolidation process. Post-processing techniques, such as compaction using heated platens, also referred to as hot pressing, has been used to reduce voids in various thermoplastic composite samples, including short and continuous fibre composites [28-30]. One such study by van de Werken *et al.* [31] found that using hot isostatic pressing (HIP) of 3D-printed continuous carbon fibre/polyetheretherketone (PEEK) composites could increase the flexural strength by 46% with a 52% decrease in void content.

Joule heating, a phenomenon that occurs when an electric current is supplied to a resistive element, producing heat. When used in practice, it is commonly referred to as resistive heating

[32]. Resistive heating has been used in composite materials with electrically resistive reinforcement materials such as nickel-chromium (NiCr) wire and carbon fibre, to reduce porosity in samples during manufacturing, part heating, or to induce shape memory characteristics [33-35]. Resistive heating has been used in CWPCs for the same purposes, with the reinforcement wire also acting as the heating element. A study by Akhoundi [20] applied varying voltages to the reinforcement wire of 3D-printed unidirectional NiCr/PLA CPWCs and achieved up to 75.9% shape recovery. Ibrahim *et al.* [36] used resistive heating on 3D-printed NiCr/PLA CWPCs for composite de-icing panels.

The 3D printing of continuous wire-reinforced composites presents a unique opportunity for research and industrial applications by allowing for the manufacturing of geometrically complex parts with relatively inexpensive equipment and materials. Previous studies have used CWPCs as strain sensors by measuring the gauge factor under loading. However, the research to this point is mostly limited to unidirectional samples with high void content. CWPCs can be 3D printed with alternating wire reinforcement or lamina directions when the samples undergo combined loading. This alternate reinforcement orientation of the lamina can also be applied to sensing applications, where the structure applies loads in multiple directions to the CWPC sensor. Future design and implementation work of CWPCs requires an understanding of alternate layups to increase their use cases. This work studies the mechanical properties of longitudinal and transverse unidirectional, and cross-ply samples under uniaxial tension with reduced void content to better understand their applications. Uniaxial tensile tests paired with digital image correlation (DIC) are performed on CWPCs to better understand the difference in mechanical strength and stiffness between samples. A consolidation procedure is performed to reduce the void content of the CWPC samples through resistive heating and hot-pressing. The experimental results for the

elastic modulus are compared to classical laminate plate theory (CLPT) calculations of the mechanical properties of the samples.

4.2. Materials & Methodology

4.2.1. Materials and Sample Manufacturing

Continuous wire polymer composite samples were 3D printed using a modified FFF 3D printer (Prusa i3 MK2, Prusa Research, Prague, Czech Republic). A 1 mm diameter nozzle with a hardened-steel tip was used to co-extrude the polymer matrix and the reinforcement wire. The matrix material used was PLA filament (1.75 mm Transparent PLA, Eryone, China). The continuous wire reinforcement was pre-measured and re-spooled 0.09 mm diameter ML polyamide enamel coated nickel-chromium (NiCr) high-precision resistance wire with a resistivity value of 65.8 Ω/ft (39 AWG Evanohm Alloy S Wire, Carpenter Technology Corporation, Pennsylvania, United States) [37]. The print head was equipped with a fan to cool the samples, positioned perpendicular to the Y direction on the print bed to cool the rasters for wire adhesion (see Figure 4-1).

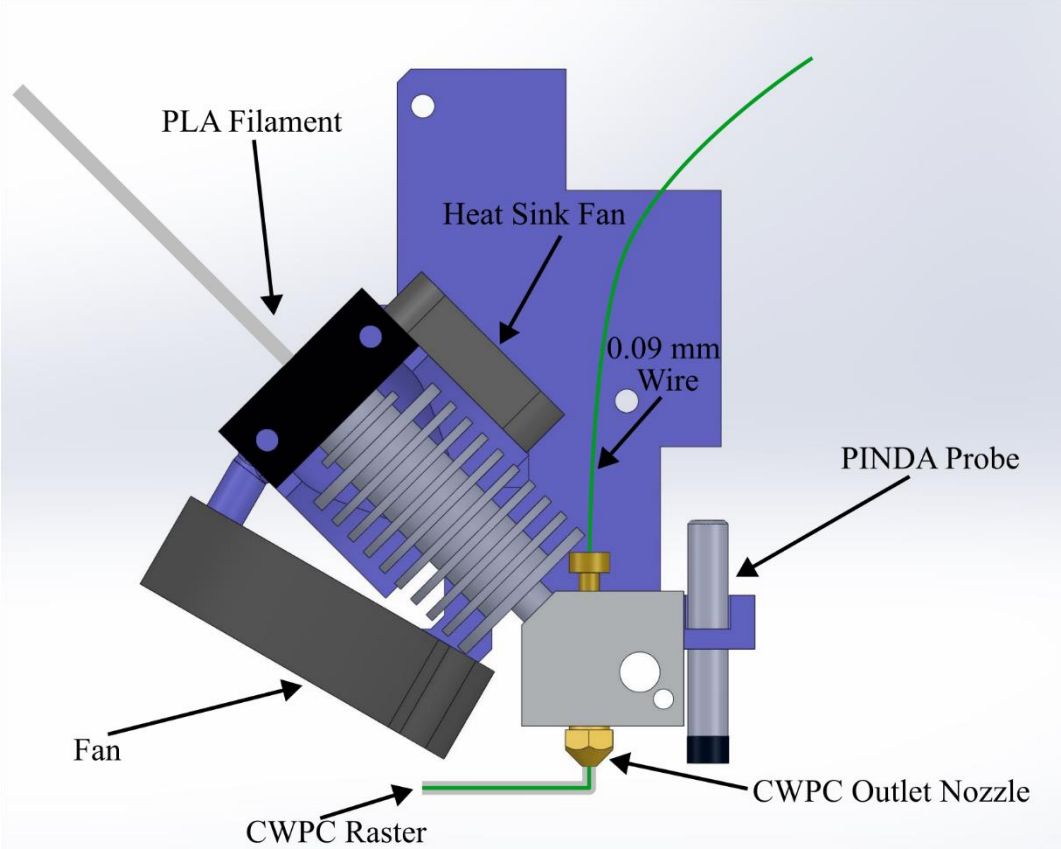

Figure 4-1: Modified print head showing filament extruded into the heat block on a 45° angle, and continuous wire reinforcement from the top, showing the fan for raster cooling

The printing parameters used were based on the previous study with some modifications to produce consistent samples with a larger geometry and different raster orientations. A custom GCode with the printing parameters seen in Table 4-1 was generated using an open-source GCode design program (FullControl GCode Designer, Loughborough, England) [38]. The GCode was designed to print samples according to ASTM D3039-17 with nominal dimensions of 200 mm long x 25 mm wide x 2.5 mm thick [39].

Table 4-1: Sample printing parameters

Nozzle Temperature	200°C
Bed Temperature	55°C
Printing Speed	3 mm/s
Fan Speed	65%
Flow Rate	90%
Extrusion Width	1.0 mm
Extrusion Height	0.5 mm
Number of Layers	5
Nozzle Diameter	1 mm
Wire Diameter	0.09 mm

4.2.2. CWPC Laminate Layup Design

When the majority of loading is known to be in one direction, fibres can be laid unidirectionally. However, composite materials are often used in combined loading applications. Therefore, composite material design often employs laminate layups in order to maintain strength in multiple directions. Cross-plies, which consist of 0° (longitudinal) and 90° (transverse) plies, are used frequently in composite materials to maintain strength in more than one direction. Baharlou *et al.* [40] found cross-plies provided the highest increase in yield strength, 7.49%, when comparing short carbon-fibre reinforced PLA compared with neat PLA 3D-printed samples. Komal *et al.* [41] found cross-ply 3D-printed CFRPCs to have better fatigue life compared to unidirectional CFRPC samples with fibres in the direction of loading. Cross-plies also present alternate functionalities, as observed by Kumar *et al.* [42], who 3D printed continuous carbon fibre-reinforced samples with a shape memory polymer. Applying heat to deformed CFRPC samples to induce the shape memory behaviour demonstrated that cross-ply laminates demonstrated comparable shape memory recovery and a better ability to retain the deformed shape, than samples reinforced longitudinally.

Cross-ply CWPC laminates were 3D printed to determine their mechanical properties in comparison to both longitudinal and transverse unidirectional samples. Three 3D-printed CWPC sample laminate layups were used in this study: 0° UD, 90° UD, and cross-ply samples with a $[90/0/\overline{90}]_S$ laminate layup (Figure 4-2). Where the 0° and 90° directions are the longitudinal and transverse directions during loading, respectively. Each were printed with 5 layers, or lamina to prevent significant warpage when taken off the print bed or during consolidation. Layers were printed with a 0.5 mm layer height, resulting in a nominal sample thickness of 2.5 mm.

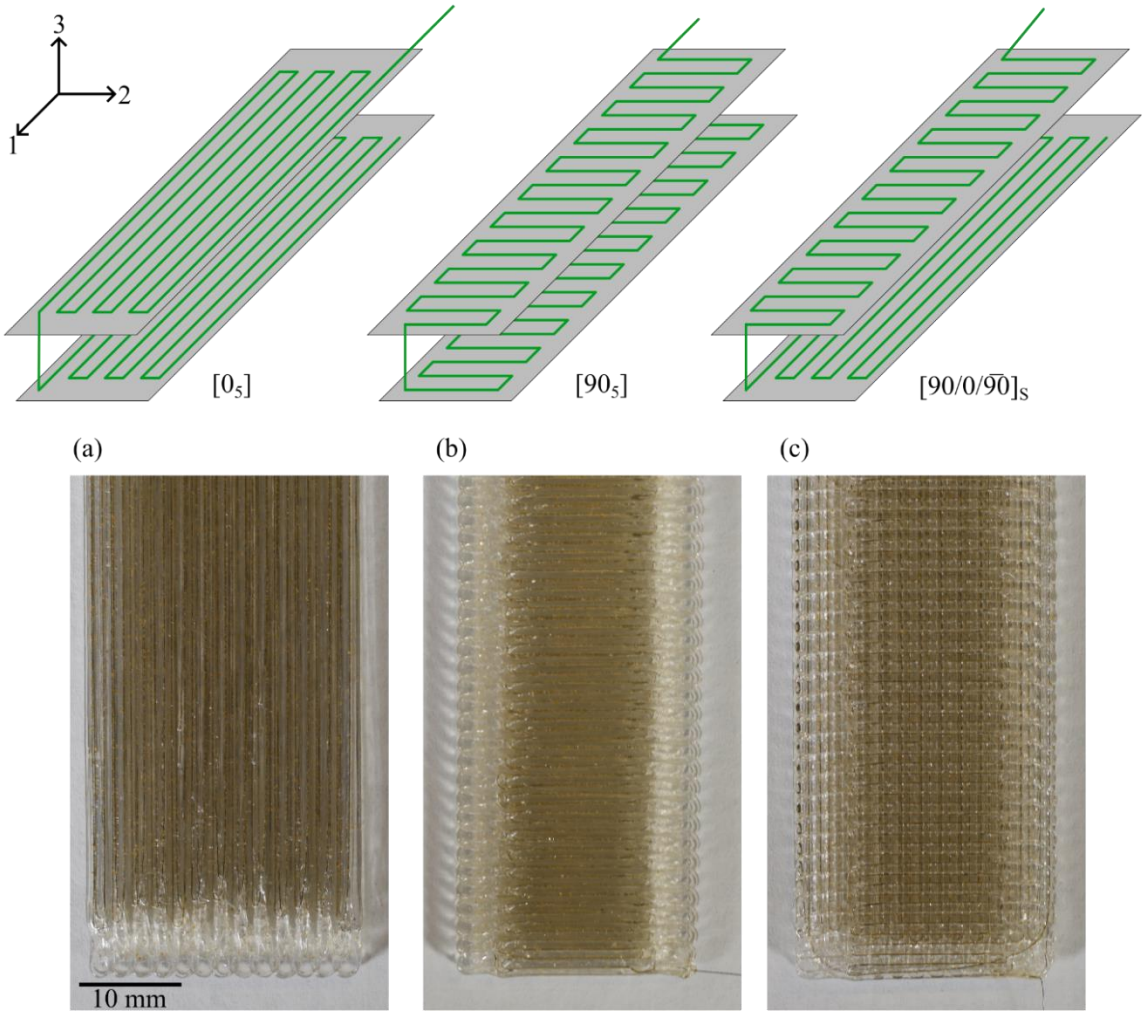

Figure 4-2: Illustrative figure showing two layers of each sample type with reinforcements relative ot the local composite coordinate [1, 2, 3] system for CWPC sample laminate layups showing the fourth and fifth layers of (a) UD-0°, (b) UD-90°, and (c) cross-ply samples

The GCode that instructs the print head movement controls the path of the centre of the print head, which typically results in larger final dimensions. The nozzle diameter dictates the tolerance of the final dimensions of 3D-printed parts; due to the large nozzle diameter used to co-extrude the continuous metal wire, the final printed samples were wider than the nominal dimensions. The printed sample dimensions were measured using vernier calipers (0-150MM, 0.01MM Absolute Digital Caliper, Asimeto, China) and a digital micrometer (3732XFL-1 Electronic Micrometer, Starrett Co., China) for the width and thickness, respectively. Three measurements along the gage length of each were measured and the average of the three measurements were taken as the dimensions of the sample, according to ASTM D3039-17 [39]. The measured sample dimensions and wire resistance measured using a digital multimeter (NTK028, Neoteck, China) can be seen in Table 4-2. The measured values of each sample was used in data analysis rather than the nominal dimensions.

Table 4-2: Average measured sample width and thickness, and reinforcement wire resistance after printing with standard deviation

Sample Type	Width [mm]	Thickness [mm]	Resistance [Ω]
UD-0°	26.72 ± 0.12	2.774 ± 0.100	5291 ± 48
UD-90°	26.46 ± 0.16	2.863 ± 0.162	3685 ± 94
Cross-Ply	26.52 ± 018	2.864 ± 0.140	4424 ± 59

The electrical resistance was used to calculate the wire length, given the resistivity value of 65.8 Ω/ft from the wire spool. The wire volume fraction (W_{vf}) is given by

$$W_{vf}(\%) = \frac{\left(D_w \cdot \frac{\pi}{4}\right) \cdot l_w}{l \cdot w \cdot t} \times 100\% \qquad \text{(Eq. 4-1)}$$

Where D_w is the wire diameter (0.09 mm), l_w is the wire length, calculated from the measured resistance and the resistivity and converted to mm, l is the nominal sample length of 200 mm, w is the measured width of each sample, and t is the measured thickness of each sample.

The end tab procedure followed the guide from the Office of Aviation Research [43]. End tabs with dimensions of 60 mm long x 26.5 mm wide x 2 mm thick with a 6.7° taper angle at 100% infill were FFF 3D printed (Bambu Lab A1, Bambu Lab, Shenzhen, China). The end tabs (Figure 4-3) were bonded to the samples using epoxy resin (System 2000 Epoxy Laminating Resin, Fibre Glast Developments Corporation, Ohio, United States) and hardener (20 Minute Epoxy Cure 2020, Fibre Glast Developments Corporation, Ohio, United States) with a ratio of 100 parts epoxy to 23 parts hardener by weight.

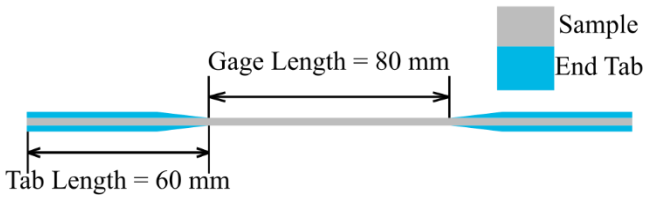

Figure 4-3: Tensile sample geometry showing gage and tab lengths

4.2.3. Sample Consolidation

A consolidation setup was made by mounting aluminum (Al 6061) 10” x 2” x 1” platens to a 3 kN load cell universal testing machine (UTM; Electropuls E3000, Instron, Massachusetts, United States), guided by 12 mm alignment shafts for proper platen alignment during consolidation. The platens were heated by five embedded 250 W cartridge heaters (0.25” diameter, 2” length), and one 1/16” diameter T-type thermocouple was placed in each platen for temperature monitoring. PID temperature controllers (DTB 4824RR, Delta Electronics, Taoyuan, Taiwan) were used to control the temperature of the platens with feedback from the thermocouple (see Figure 4-4).

The approach to choosing the consolidation procedure steps was based on the analytical model from the previous study. Figure 4-4 shows a schematic of the consolidation setup outlining the cartridge heaters to heat the platens and the thermocouple inputs for the PID controllers to control the power supplied to the cartridge heaters. While the sample was heated externally from the heated aluminum platens, a 120 V power supply (6655 A, Hewlett Packard, California, United States) was used to apply resistive heating to the CWPC samples to uniformly heat the samples in each layer.

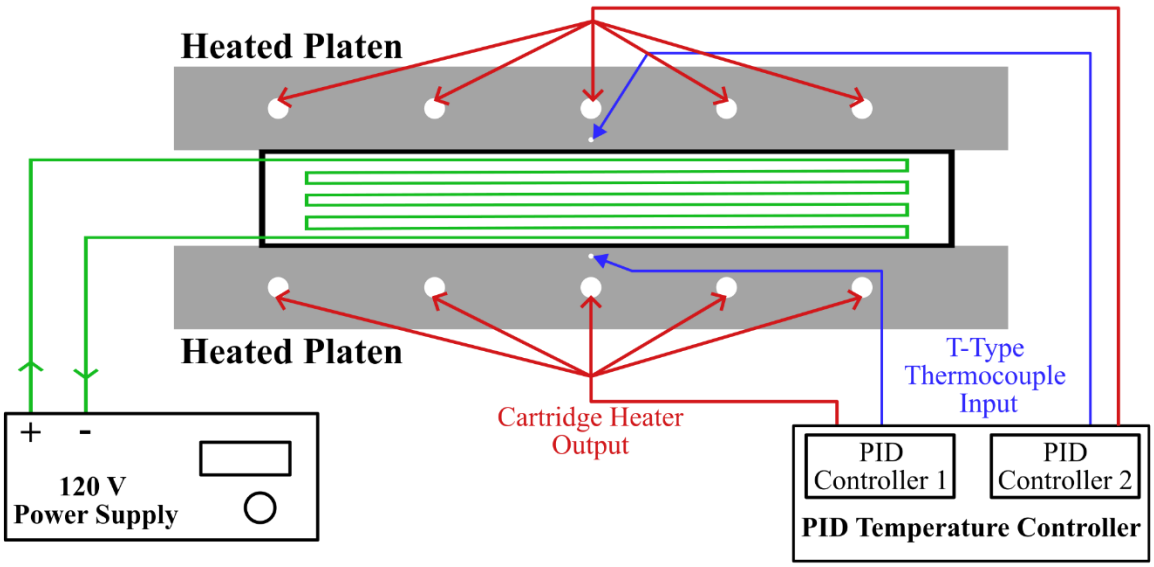

Figure 4-4: Schematic of the consolidation setup showing the heated platens machined for embedded cartridge heaters, which are controlled by the PID temperature controller with feedback from T-type thermocouple inputs while a 120 V power supply is used for resistive heating of the sample

The platens were preheated to 70°C, then the sample was placed with the build plate side facing up, so it would contact the top platen when under consolidation. The top platen was then lowered to make contact with the sample and was held at -10 N for 50 s to heat the PLA matrix to 65°C, just above its glass transition temperature (T_g). After 50 s, 0.5 MPa of compaction pressure was applied and held for 15 s, after which the top platen was lifted, and the sample was removed. To

mitigate warpage of the composite induced due to the heating process, a T-slot aluminum stock with weight on top was placed on top of the sample when it was taken out of the platens. A photograph of the consolidation setup mounted to the UTM can be seen in Figure 4-5.

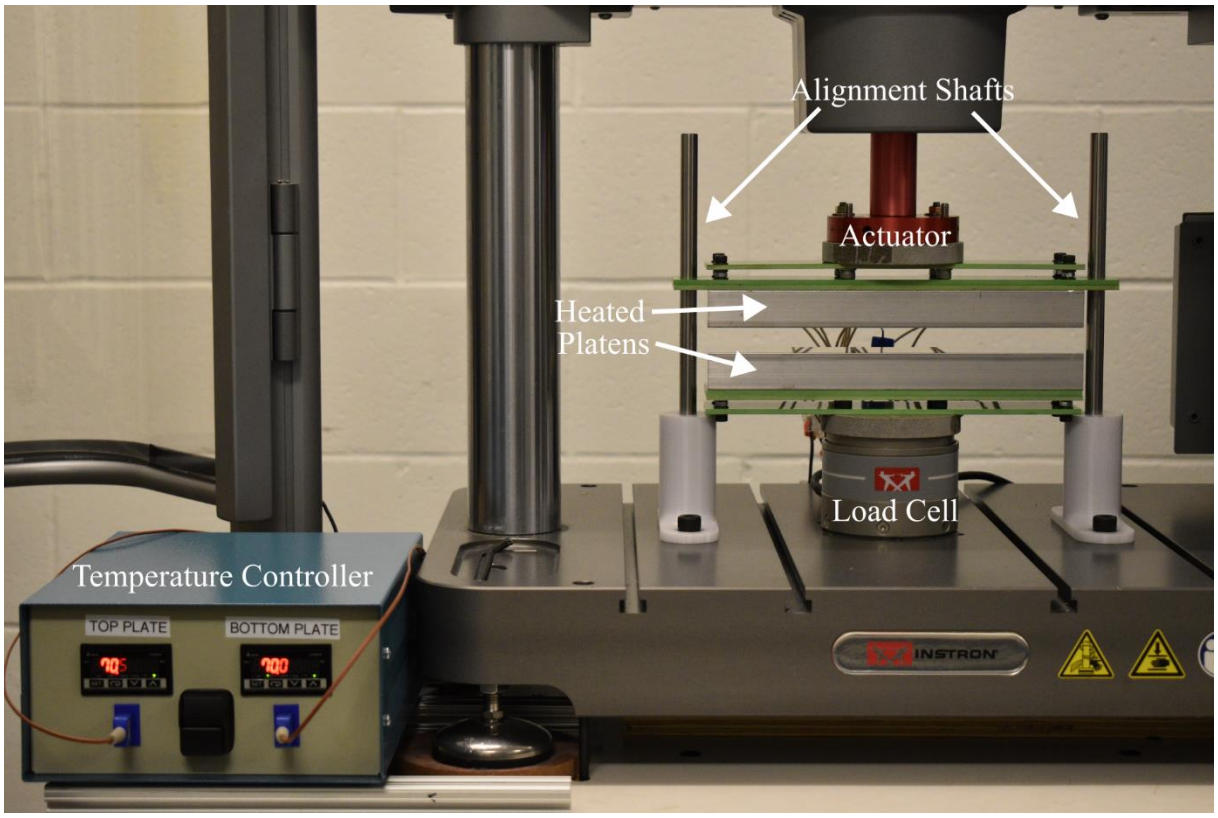

Figure 4-5: Consolidation setup showing the heated platens mounted to the load cell and actuator of the UTM, with alignment shafts used to maintain platen alignment, and the temperature controller used for maintaining a stable platen temperature

To compare the ultimate tensile strength (UTS) of each CWPC laminate layup, 12 samples of each layup configuration were 3D printed, six of each were consolidated. The dimensions of the samples that underwent consolidation were re-measured, using the same method as mentioned previously. The average measurements of all samples are listed in Table 4-3.

Table 4-3: Average measured sample dimensions of non-consolidated and consolidated samples with standard deviation

Sample Type	Width [mm]	Thickness [mm]
UD-0°	26.73 ± 0.13	2.758 ± 0.097
UD-0° (Consolidated)	26.60 ± 0.10	2.781 ± 0.076
UD-90°	26.43 ± 0.20	2.920 ± 0.117
UD-90° (Consolidated)	26.36 ± 0.20	2.866 ± 0.093
Cross-Ply	26.45 ± 0.18	2.943 ± 0.106
Cross-Ply (Consolidated)	26.33 ± 0.15	2.839 ± 0.079

4.2.4. Tensile Testing and Digital Image Correlation

Tensile testing was performed according to ASTM D3039-17 using a universal testing machine (UTM), (MTS 809 Axial/Torsional Test System, MTS Systems, Minnesota, United States) at a constant crosshead rate of 2 mm/min. The UTM had hydraulic grips, and samples were held at 1000 psi clamping pressure. Five samples per sample type was used for tensile testing, resulting in 30 total samples tested. Digital image correlation (DIC), a full-field strain measurement technique was used to capture images during the test. DIC uses a camera to track a speckled pattern on the face of the sample under loading. The images are then processed to obtain the strain fields of the sample surface during testing. DIC is commonly performed on composite materials which are difficult to measure strain using physical measurement tools such as strain gauges or extensometers, due to the size or geometry of the samples [44], [45]. Samples were first painted with a flat black paint (Painter's Touch Flat Black, Rust-Oleum, Ontario, Canada) for a base layer, then white paint mixed with reducer (5212 Opaque White/4012 High Performance Reducer, Createx Colors, Connecticut, United States) was airbrushed (Paasche Airbrush H-3MH set, Paasche Airbrush Co., Illinois, United States) to speckle the samples. The white speckles are airbrushed to provide random placement and good contrast to the black paint

for the DIC imaging software to track the displacement of the speckles. Figure 4-6 shows an example of high contrast shown by the peaks and valleys of the image intensity count with the speckled sample before testing started.

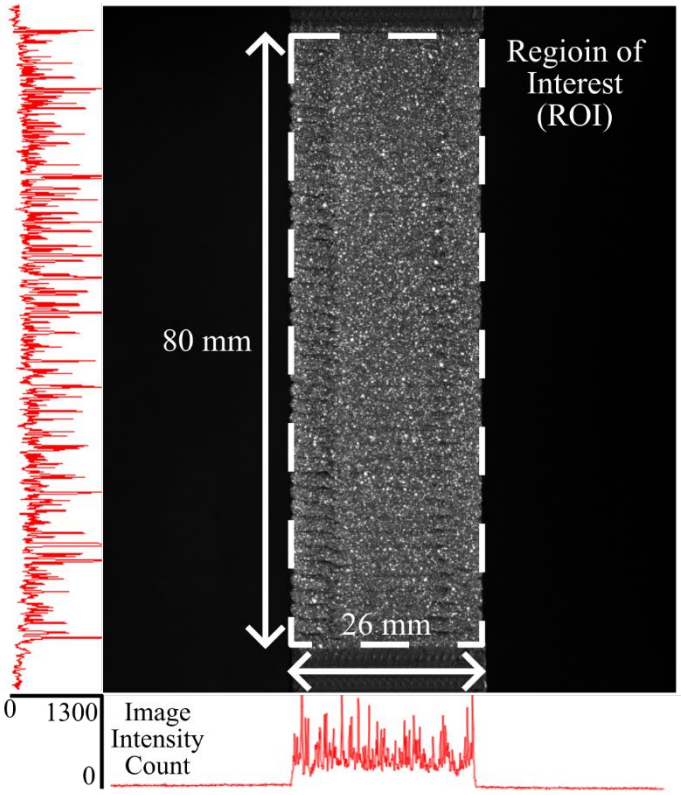

Figure 4-6: Sample image of high contrast in speckling within the region of interest (ROI) by high peaks and valleys in the image intensity plots in red

Two-dimensional digital image correlation (2D DIC) was used to calculate the strain maps of the top face of the samples. The DIC setup and processing parameters can be seen in Table 4-4. A 5 megapixel camera (Imager M-lite 5M, LaVision, Göttingen, Germany) was equipped with a 50 mm focal length lens (MVL50M23, Navitar Inc., New York, United States) to capture images at an acquisition rate of 10 frames per second (fps). For effective DIC processing, a camera working distance of 600 mm was used to yield a 76 mm x 92 mm field of view, which allows the sample to take up roughly 1/3 of the horizontal field of view [46]. Images were processed using the DIC software package (DaVis 10.2.1 Strainmaster, LaVision, Göttingen, Germany) using the

relative to first method. Two 50 mm long digital extensometers were placed 6 mm away from the centre of the sample for analyzing the average strain during testing.

Table 4-4: Digital image correlation setup and processing parameters

DIC Parameter	Value
Camera Working Distance	600 mm
Field of View (FOV)	76 mm x 92 mm
Region of Interest (ROI)	26 mm x 80 mm
Image Acquisition Rate	10 Frames Per Second
Image Scale Factor	26 pixels/mm
Correlation Subset Window Size	21 x 21 px
Correlation Step Size	7 px

4.2.5. CWPC Characterization by Classical Laminate Plate Theory

A program called *The Laminator* was used to determine the apparent laminate elastic modulus in the loading direction for comparison with the experimental elastic modulus results. The elastic modulus in the loading direction was determined from the program based on the laminate layup, assuming 0.5 mm layer thickness as per the GCode, and the lamina orientations for all three sample layup configurations. The values used for the elastic moduli of PLA (3.60 GPa) and the NiCr reinforcement wire (200 GPa) were based on a similar study performed by Ibrahim *et al.* [13]. Since CLPT assumes the composites are void free, it is expected that consolidated experimental results will be closer to the results found by CLPT and the rule of mixture.

4.2.6. Optical Microscopy

Samples were cut along the width using a manual cut-off machine (Mecatome T260, PRESI, Hungary). The cut samples were then mounted in a clear epoxy (West Systems 105 Epoxy Resin/207 Special Clear Hardener, West Systems, Michigan, United States). The samples were

sequentially ground using 180, 400, 600, 800, and 1200 grit sandpaper discs on a grinding machine at a speed of 300 rpm (StarGrind 200-2 V, Micro Star 2000 Inc., Ontario, Canada). After sanding they were polished using 1.0 µm and 0.05 µm alumina powder. An optical microscope was used to obtain images of the cross-section of samples that did not undergo tensile testing for each layup configuration and sample type (ZEISS Axio Imager 2, Zeiss Group, Baden-Württemberg, Germany).

4.3. Results & Discussion

4.3.1. Tensile Testing and Digital Image Correlation

DIC analysis was used to find the stress-strain distribution across different sample types. The stress was calculated using the measured dimensions of the individual samples and the load output from the UTM, and the strain was calculated using the two digital extensometers as previously mentioned. The stress-strain curves can be seen in Figure 4-7.

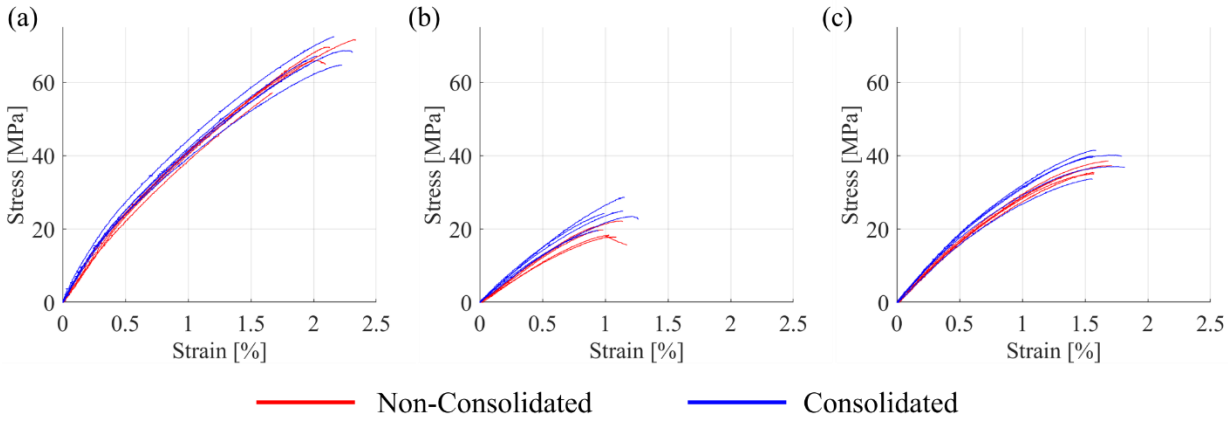

Figure 4-7: Stress-strain curves of (a) UD-0°, (b) UD-90°, (c) cross-ply samples showing both non-consolidated and consolidated results

The stress-strain curves outline that the three laminate layup configurations have similar elastic regions, though they have significantly different failure points. The samples experienced

progressive failure, with an initial brittle failure of the PLA matrix. To better understand the difference in ultimate tensile strength of the different sample types, a box and whisker plot to show the mean ultimate tensile strength, 25th and 75th quartiles, and most extreme variations from the means can be seen in Figure 4-8, while the mean and standard deviation of the ultimate tensile strength and the elastic modulus can be seen in Table 4-5.

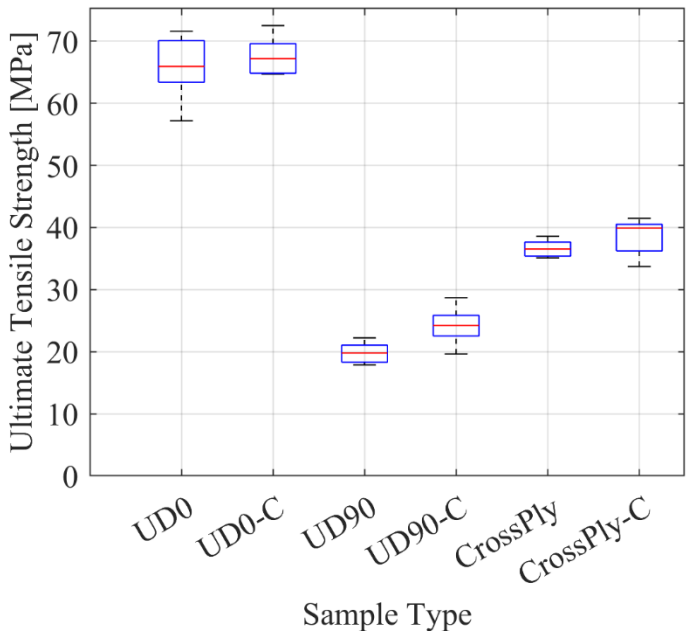

Figure 4-8: Box and whisker plot showing the ultimate tensile strength of different non-consolidated and consolidated sample layup configurations

There is a noticeably higher standard deviation in consolidated UD-90° and cross-ply samples compared to their non-consolidated counterparts. While this was unexpected, it is likely due to the variability in the printing process. Increasing the sample size for testing would provide a more true understanding of the standard deviation in the ultimate tensile strength results for the consolidated samples.

Table 4-5: Average ultimate tensile strength and elastic modulus with standard deviation for each sample type

Sample Type	Ultimate Tensile Strength [MPa]	Elastic Modulus [GPa]
UD-0°	65.95 ± 5.53	4.96 ± 0.14
UD-0° (Consolidated)	67.58 ± 3.21	5.30 ± 0.22
UD-90°	19.79 ± 1.74	2.47 ± 0.19
UD-90° (Consolidated)	24.19 ± 3.24	2.87 ± 0.17
Cross-Ply	36.60 ± 1.41	3.51 ± 0.10
Cross-Ply (Consolidated)	38.47 ± 3.11	3.67 ± 0.27

The majority of the UD-0° samples failed at the end tab taper, with one sample fracturing part of the end tab because the PLA was thin. Future testing should use either a larger taper angle, or lower clamping pressure to prevent this. For the non-consolidated sample properties, the UD-0°, UD-90° and cross-ply samples displayed ultimate tensile strengths of 65.95 MPa, 19.79 MPa, and 36.60 MPa, respectively. As expected, the UD-0° samples had the strongest mechanical properties of because the fibres were all parallel to the direction of loading and the UD-90° samples were the weakest as they were perpendicular. While the cross-ply samples show mechanical properties between those of UD-0° and UD-90°, it is possible that if the cross-ply layup was $[0/90/\overline{0}]_S$ rather than $[90/0/\overline{90}]_S$, as was used in this study, the mechanical properties could potentially be increased due to there being a higher number of layers with reinforcement wires parallel to the loading direction rather than perpendicular to it. It is worth noting that overall, the largest increase in ultimate tensile strength and elastic modulus as a result of the consolidation procedure were of the UD-90° samples. Because the wires were perpendicular to the loading direction, more stress was distributed to the PLA matrix. The consolidation procedure increased the bond between individual rasters, which increased the strength of the CWPCs, similar to the results found by Allum *et al.* [8] which found that the weak bond between transverse rasters causes decreased mechanical properties of 3D-printed samples.

To determine the effects the consolidation procedure has on each laminate layup, an independent *t*-test was conducted with a confidence interval of 95%, where a *P* -value less than 0.05 shows that the increase in ultimate tensile strength or elastic modulus due to the void reduction from the consolidation procedure is statistically significant. The results of the *t*-test can be seen in Table 4-6.

Table 4-6: Independent t-test resulting P -value to determine the statistical significance the consolidation procedure has on the ultimate tensile strength and elastic modulus for each laminate layup configuration

Mechanical Property	**Sample**	***P* -value**
Ultimate Tensile Strength [MPa]	UD-0°	0.5890
	UD-90°	**0.0361**
	Cross-Ply	0.2708
Elastic Modulus [GPa]	UD-0°	**0.0252**
	UD-90°	**0.0090**
	Cross-Ply	0.2273

The UD-90° samples showed a statistically significant increase in both ultimate tensile strength and elastic modulus, while the UD-0° sample only showed a statistically significant increase in elastic modulus. The mechanical properties of the cross-ply samples did not significantly increase after the consolidation procedure. While there appears to similar increase in ultimate tensile strength for the cross-ply samples, the large standard deviation results in a larger *P* -value because the true mean is less certain. A higher sample size would result in higher certainty in the true mean and could affect the statistical analysis. García de la Camacha *et al.* [19] noted that the adhesion between the continuous wire and polymer matrix caused decreased strength in samples where the reinforcement wire was not in the direction of loading. In the current study, the ultimate tensile strength and elastic modulus of the consolidated UD-90° samples were 20.0% and 15.0% higher than the non-consolidated UD-90° samples, respectively.

To highlight the changes of the strain fields for the different sample types, three sample images were taken for each non-consolidated and consolidated laminate layup. The strain field when the sample experienced a 500 N load, which is in the elastic region, the load at failure, and the average of the two loads are presented in Figure 4-9. The strain maps highlight where there are high strain regions within the sample during loading, often showing where failure is initiated. While the strain fields of the UD-0° samples are uniform across the whole ROI, the UD-90° and cross-ply samples, which both have 90° ply outer layers, there are clear stress concentrations at the bond interface between rasters. Consolidated samples show a more uniform distribution because the bond is increased after consolidation, though there is still a noticeable interface visible to the eye. The DIC performed was 2D and only showed the strain fields on the top surface of the samples. However, future work could potentially benefit from performing 2D DIC with two cameras, one for the top surface and the other for the build plate side of the samples to better understand where crack propagation first occurs.

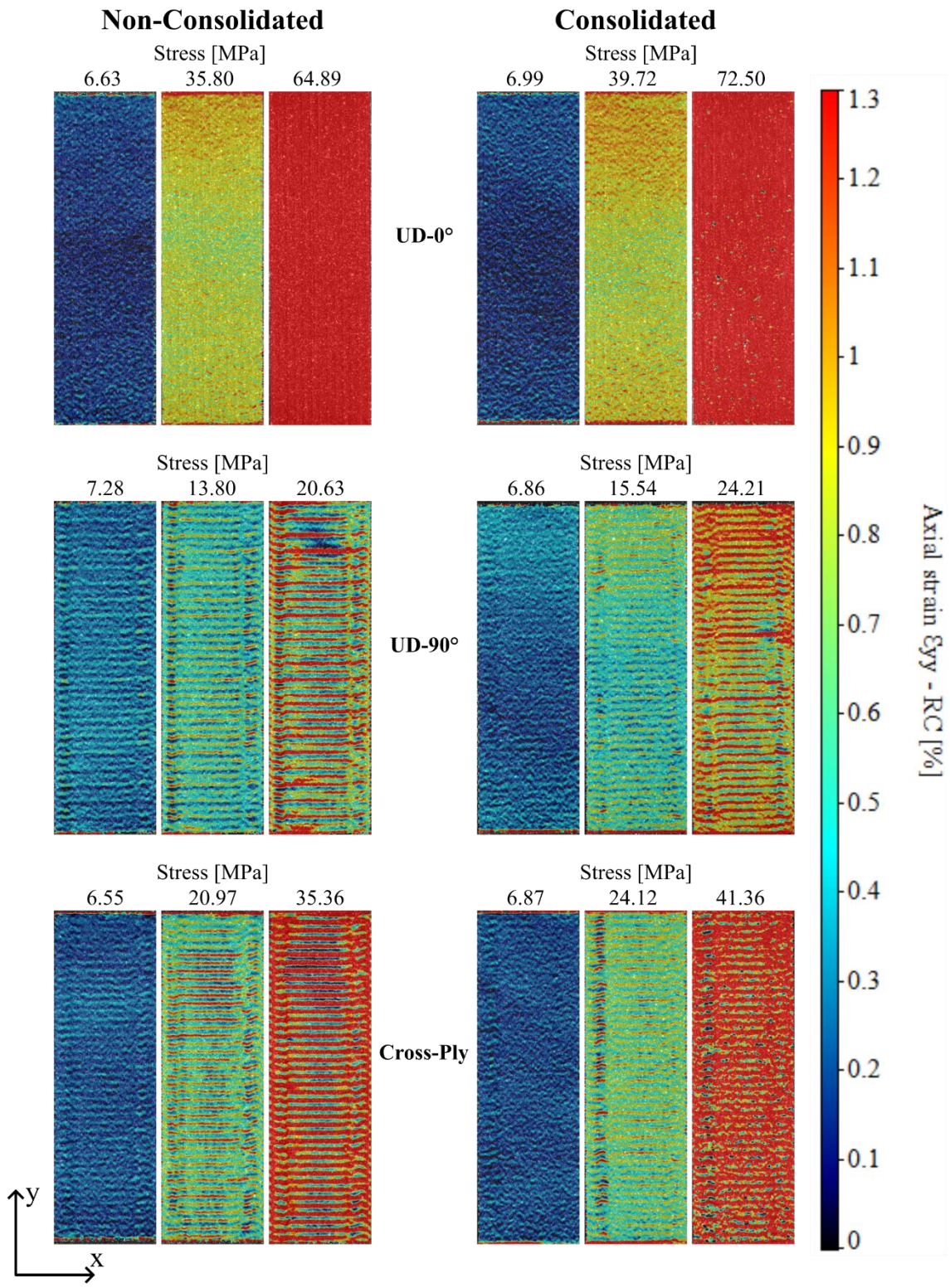

Figure 4-9: DIC strain fields showing each sample configuration (non-consolidated and consolidated) within the elastic region, plastic region, and failure stress

One test of each sample type both non-consolidated and consolidated were tested beyond the initial matrix failure (see Figure 4-10). The force-displacement curves show that the peak force at matrix failure is reached by the sample, followed by a large decrease in load, then a small rise again before slowly approaching failure. It is observed that the load maintained by the wires after matrix failure stays consistent while it is continued to be pulled apart.

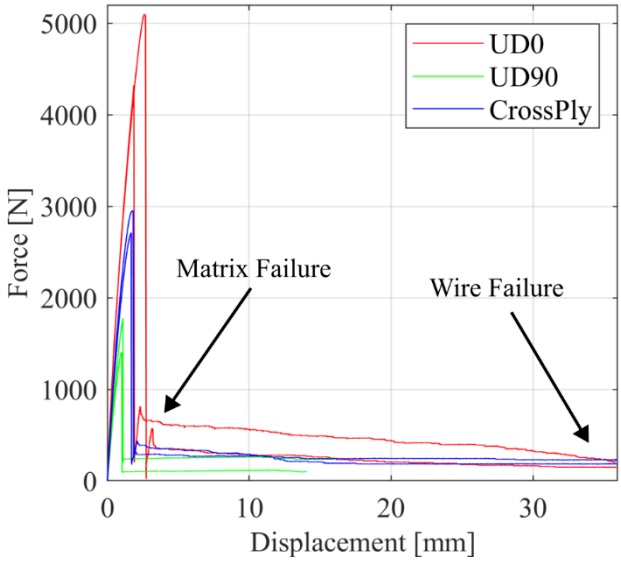

Figure 4-10: Complete failure of CWPCs for all laminate layups, both non-consolidated and consolidated

4.3.2. CWPC Characterization by Classical Laminate Plate Theory

The goal of using CLPT to calculate the apparent laminate stiffness was to view how close the samples performed to an analytical prediction. CLPT assumes that there are no voids in the samples, both the experimental elastic modulus for consolidated and non-consolidated samples are compared to the apparent laminate stiffness in Table 4-7.

Table 4-7: Average elastic modulus with standard deviation for each sample type compared to the apparent laminate stiffness calculated by CLPT for the three sample laminate layups with the percent difference between the experimental elastic modulus and apparent laminate stiffness results

Sample Type	Experimental Elastic Modulus [GPa]	Apparent Laminate Stiffness [GPa]	% Difference
UD-0°	4.96 ± 0.14	5.67 ± 0.09	13.4%
UD-0° (Consolidated)	5.30 ± 0.22		6.7%
UD-90°	2.47 ± 0.19	3.67 ± 0.00	39.1%
UD-90° (Consolidated)	2.87 ± 0.17		24.5%
Cross-Ply	3.51 ± 0.10	4.32 ± 0.05	20.7%
Cross-Ply (Consolidated)	3.67 ± 0.27		16.3%

Both the non-consolidated and consolidated UD-0° samples were closer to the apparent laminate stiffness than UD-90° and cross-ply samples. As expected, the apparent laminate stiffness calculated using *The Laminator* showed a smaller difference between consolidated samples, which contain lower void content than their non-consolidated counterparts, with the most significant difference being the UD-90° samples with a 14.6% increase in percent difference between the consolidated and non-consolidated samples compared to the apparent laminate stiffness. While the consolidated samples show a smaller difference between the apparent laminate stiffness and the experimental elastic modulus, the experimental results still underperform the expected calculations significantly. This is because *The Laminator* relies on the rule of mixtures, which can be less effective for lower fibre volume fractions, as the samples in this study are ≤ 1%. The rule of mixtures is also less useful for predicting the properties of transverse plies, which causes the larger percent difference in the UD-90° and cross-ply CWPC laminates.

4.3.3. Optical Microscopy

Figure 4-11 displays the cross-section microscopy of the samples at 2.5x magnification, where consolidated samples show there are fewer voids than in samples that were not consolidated.

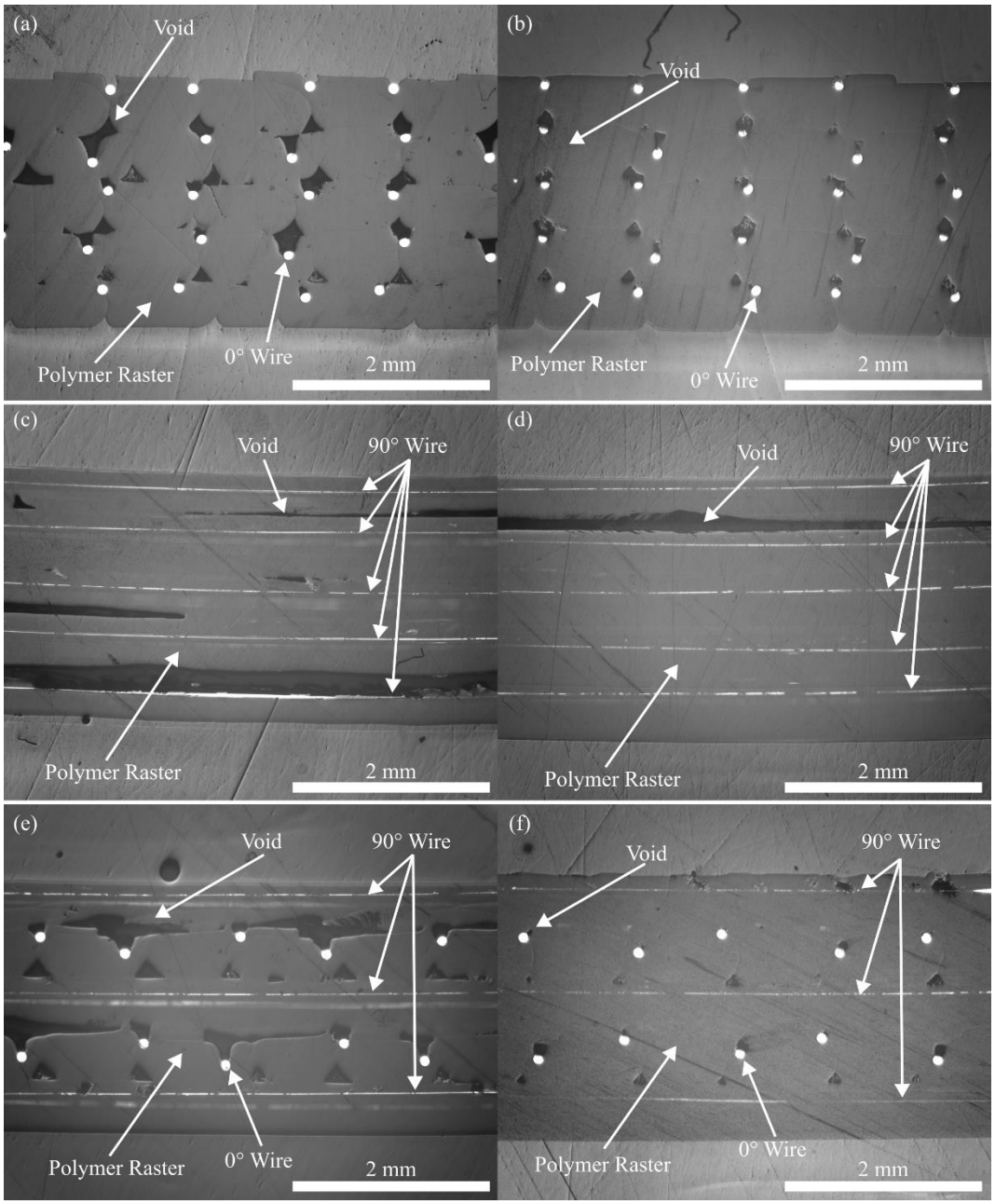

Figure 4-11: Optical microscope images showing the wire reinforcements, voids, and polymer rasters for (a) UD-0°, (b) UD-0° (consolidated), (c) UD-90°, (d) UD-90° (consolidated), (e) cross-ply, (f) cross-ply (consolidated)

Curvature of the cross section is observed in the figures above, specifically for the consolidated UD-90° and cross-ply samples which both have transverse reinforcement. This is likely from the warpage after being removed from the platens after consolidation. This warpage occurred because the NiCr alloy, which is known to display shape memory behaviour will warp along the wire. The transverse reinforcement causes curvature along the width, where the cross-section was cut. When the CWPC samples are removed from the platens, they instantly begin to cool below the T_g. The effects of this warpage were mitigated by using T-slotted aluminum to attempt to flatten the samples, however, allowing the aluminum platens to cool while the sample remains put could potentially be a more suitable alternative to prevent this warpage.

4.4. Conclusion

This study aimed to investigate the tensile properties of unidirectional reinforcement either parallel (UD-0°) and perpendicular (UD-90°) to the loading direction and cross-ply samples, where each layer alternates between 0° and 90° plies. The application of the cross-ply CWPC laminate layup allows for a wider application of uses as it reinforces the CWPC in more than one direction, increasing the stresses it can withstand when under combined loading. A consolidation procedure developed in a previous study by the authors was performed to reduce the void content of the CWPC samples, and the results between non-consolidated and consolidated samples were compared. DIC was used to analyze the strain fields on the outer top face of the sample, rather than the build plate. Non-consolidated UD-0°, UD-90° and cross-ply samples showed ultimate tensile strengths of 65.95 MPa, 19.79 MPa, and 36.60 MPa, while consolidated samples showed ultimate tensile strengths of 67.58 MPa, 24.19 MPa, and 38.47 MPa. Independent *t*-tests determined that the ultimate tensile strength and elastic modulus of UD-90° samples were statistically significantly improved due to consolidation, with improvements of 20.0% and

15.0%, respectively. The elastic modulus of the UD-0° samples were also statistically significantly improved by the consolidation procedure, with a 6.6% increase in elastic modulus. The experimental results for the elastic modulus were compared to classical laminate plate theory (CLPT) calculations of the mechanical properties of the samples. Future work could include further laminate layups including quasi-isotropic CWPC laminates. Void quantification was not performed in this study specifically, but optical measurement techniques such as computed tomography could be used to determine the void content in the samples and quantify the relation between the void reduction and the increase in mechanical properties.

4.5. References

[1] Y. Tao et al., “A review on voids of 3D printed parts by fused filament fabrication,” Journal of Materials Research and Technology, vol. 15, pp. 4860–4879, Nov. 2021, doi: 10.1016/J.JMRT.2021.10.108.

[2] M. E. Mackay, “The importance of rheological behavior in the additive manufacturing technique material extrusion,” J Rheol (N Y N Y), vol. 62, no. 6, pp. 1549–1561, Nov. 2018, doi: 10.1122/1.5037687.

[3] M. Somireddy, C. V. Singh, and A. Czekanski, “Analysis of the material Behavior of 3D printed laminates via FFF,” Exp Mech, vol. 59, no. 6, pp. 871–881, Jul. 2019, doi: 10.1007/S11340-019-00511-5/FIGURES/9.

[4] J. M. Chacón, M. A. Caminero, E. García-Plaza, and P. J. Núñez, “Additive manufacturing of PLA structures using fused deposition modelling: Effect of process parameters on mechanical properties and their optimal selection,” Mater Des, vol. 124, pp. 143–157, Jun. 2017, doi: 10.1016/J.MATDES.2017.03.065.

[5] K. A. Hamzah et al., “Effect of the Printing Orientation on the Mechanical Properties and Thermal and Electrical Conductivity of ABS-ZnFe2O4 Composites,” J Mater Eng Perform, vol. 28, no. 9, pp. 5860–5868, Sep. 2019, doi: 10.1007/S11665-019-04313-7/FIGURES/16.

[6] J. M. Chacón, M. A. Caminero, P. J. Núñez, E. García-Plaza, I. García-Moreno, and J. M. Reverte, “Additive manufacturing of continuous fibre reinforced thermoplastic composites using fused deposition modelling: Effect of process parameters on mechanical properties,” Compos Sci Technol, vol. 181, Sep. 2019, doi: 10.1016/j.compscitech.2019.107688.

[7] M. Iragi, C. Pascual-González, A. Esnaola, C. S. Lopes, and L. Aretxabaleta, “Ply and interlaminar behaviours of 3D printed continuous carbon fibre-reinforced thermoplastic laminates; effects of processing conditions and microstructure,” Addit Manuf, vol. 30, p. 100884, Dec. 2019, doi: 10.1016/J.ADDMA.2019.100884.

[8] J. Allum, A. Moetazedian, A. Gleadall, and V. V. Silberschmidt, “Interlayer bonding has bulk-material strength in extrusion additive manufacturing: New understanding of anisotropy,” Addit Manuf, vol. 34, p. 101297, Aug. 2020, doi: 10.1016/J.ADDMA.2020.101297.

[9] K. Fayazbakhsh, M. Movahedi, and J. Kalman, “The impact of defects on tensile properties of 3D printed parts manufactured by fused filament fabrication,” Mater Today Commun, vol. 18, pp. 140–148, Mar. 2019, doi: 10.1016/J.MTCOMM.2018.12.003.

[10] G. W. Melenka, B. K. O. Cheung, J. S. Schofield, M. R. Dawson, and J. P. Carey, “Evaluation and prediction of the tensile properties of continuous fiber-reinforced 3D printed structures,” Compos Struct, 2016, doi: 10.1016/j.compstruct.2016.07.018.

[11] T. Heitkamp et al., “Stress-adapted fiber orientation along the principal stress directions for continuous fiber-reinforced material extrusion,” Progress in Additive Manufacturing, vol. 8, pp. 541–559, 2023, doi: 10.1007/s40964-022-00347-x.

[12] G. Feng, C. Xiao, H. Wang, H. Zhang, B. Liu, and C. Wang, “Enhancing mechanical properties of 3D-printed continuous carbon fibre-reinforced composites via bio-inspired design,” Thin-Walled Structures, vol. 207, p. 112737, Feb. 2025, doi: 10.1016/J.TWS.2024.112737.

[13] Y. Ibrahim, G. W. Melenka, and R. Kempers, “Fabrication and tensile testing of 3D printed continuous wire polymer composites,” Rapid Prototyp J, vol. 24, no. 7, pp. 1131–1141, Oct. 2018, doi: 10.1108/RPJ-11-2017-0222.

[14] C. Thompson, C. González, and J. LLorca, “Material extrusion fabrication of continuous metal wire-reinforced polymer–matrix composites,” Composites Communications, vol. 50, p. 102024, Oct. 2024, doi: 10.1016/J.COCO.2024.102024.

[15] M. A. Saleh, R. Kempers, and G. W. Melenka, “3D printed continuous wire polymer composites strain sensors for structural health monitoring,” Smart Mater Struct, 2019, doi: 10.1088/1361-665X/aafdef.

[16] M. A. Saleh, R. Kempers, and G. W. Melenka, “A comparative study on the electromechanical properties of 3D-Printed rigid and flexible continuous wire polymer

composites for structural health monitoring," Sensors and Actuators A, vol. 328, p. 112764, 2021, doi: 10.1016/j.sna.2021.112764.

[17] M. A. Saleh, R. Kempers, and G. W. Melenka, "Fatigue behavior and electromechanical properties of additively manufactured continuous wire polymer composites for structural health monitoring," Fatigue Fract Eng Mater Struct, vol. 45, no. 9, pp. 2630–2645, Sep. 2022, doi: 10.1111/ffe.13778.

[18] Y. Ibrahim and R. Kempers, "Effective thermal conductivity of 3D-printed continuous wire polymer composites," Progress in Additive Manufacturing, vol. 7, no. 4, pp. 699–712, Aug. 2022, doi: 10.1007/S40964-021-00256-5/FIGURES/12.

[19] Á. García de la Camacha, J. Sánchez del Río, and J. LLorca, "Additive manufacturing of quasi-isotropic wire-reinforced metal-polymer composite laminates," Rapid Prototyp J, vol. 31, no. 7, pp. 1449–1460, 2025, doi: 10.1108/RPJ-11-2024-0467.

[20] B. Akhoundi, "An evaluation of the shape-memory behavior and mechanical properties of polylactic acid/Ni80Cr20 continuous wire composite produced by extrusion-based additive manufacturing and in-melt simultaneous impregnation method," Journal of Reinforced Plastics and Composites, vol. 43, no. 13–14, pp. 783–797, Jul. 2024, doi: 10.1177/07316844231197036.

[21] Y. Ibrahim, G. W. Melenka, and R. Kempers, "Flexural properties of three-dimensional printed continuous wire polymer composites," Materials Science and Technology (United Kingdom), vol. 35, no. 12, pp. 1471–1482, Aug. 2019, doi: 10.1080/02670836.2019.1630085.

[22] M. Ueda et al., "3D compaction printing of a continuous carbon fiber reinforced thermoplastic," Compos Part A Appl Sci Manuf, vol. 137, Oct. 2020, doi: 10.1016/j.compositesa.2020.105985.

[23] Y. Asano, M. Ueda, M. Yamawaki, R. Matsuzaki, A. Le Duigou, and M. Castro, "Layer-wise compaction 3D printing: void reduction and interfacial enhancement for continuous carbon fiber–reinforced thermoplastics," Advanced Composite Materials, pp. 1–15, Feb. 2025, doi: 10.1080/09243046.2025.2459672.

[24] T. Yiwen, T. Yuegang, Z. Fan, and Z. Jun, “Laser assisted rapid 3D printing of continuous carbon fiber reinforced plastics: Simulation, characterization, and properties,” Polym Compos, vol. 44, no. 6, pp. 3084–3094, Jun. 2023, doi: DOI:10.1002/pc.27303.

[25] Z. Ouyang, L. Yang, Z. Pi, Z. Wang, C. Yan, and Y. Shi, “Robot-assisted laser additive manufacturing for high-strength/low-porosity continuous fiber-reinforced thermoplastic composites,” Compos Sci Technol, vol. 247, p. 110397, Mar. 2024, doi: 10.1016/J.COMPSCITECH.2023.110397.

[26] A. Uşun, B. B. Vatandaş, and R. Gümrük, “Enhanced mechanical properties of continuous carbon fiber reinforced polyether-ether-ketone composites via infrared preheating and high fiber volume fraction,” Addit Manuf, vol. 89, p. 104289, Jun. 2024, doi: 10.1016/J.ADDMA.2024.104289.

[27] N. Elderfield and J. C. H. Wong, “Discrete in-situ consolidation of additively manufactured continuous fiber-reinforced polymer composites,” Compos Part A Appl Sci Manuf, vol. 171, Aug. 2023, doi: 10.1016/j.compositesa.2023.107562.

[28] A. Levy and P. Hubert, “Interstrand void content evolution in compression moulding of randomly oriented strands (ROS) of thermoplastic composites,” Compos Part A Appl Sci Manuf, vol. 70, pp. 121–131, Mar. 2015, doi: 10.1016/J.COMPOSITESA.2014.11.017.

[29] M. A. Valverde, J. P. H. Belnoue, R. Kupfer, L. F. Kawashita, M. Gude, and S. R. Hallett, “Compaction behaviour of continuous fibre-reinforced thermoplastic composites under rapid processing conditions,” Compos Part A Appl Sci Manuf, vol. 149, Oct. 2021, doi: 10.1016/j.compositesa.2021.106549.

[30] H. Mei, Z. Ali, Y. Yan, I. Ali, and L. Cheng, “Influence of mixed isotropic fiber angles and hot press on the mechanical properties of 3D printed composites,” Addit Manuf, vol. 27, pp. 150–158, May 2019, doi: 10.1016/J.ADDMA.2019.03.008.

[31] N. van de Werken, P. Koirala, J. Ghorbani, D. Doyle, and M. Tehrani, “Investigating the hot isostatic pressing of an additively manufactured continuous carbon fiber reinforced PEEK composite,” Addit Manuf, vol. 37, p. 101634, 2021, doi: 10.1016/j.addma.2020.101634.

[32] H. Jouhara et al., “Thermoelectric generator (TEG) technologies and applications,” International Journal of Thermofluids, vol. 9, p. 100063, Feb. 2021, doi: 10.1016/J.IJFT.2021.100063.

[33] J. Reese, M. Vorhof, G. Hoffmann, K. Böhme, and C. Cherif, “Joule heating of dry textiles made of recycled carbon fibers and PA6 for the series production of thermoplastic composites,” J Eng Fiber Fabr, vol. 15, 2020, doi: 10.1177/1558925020905828.

[34] A. Cortés, A. Esperanza, J. Gómez-Sánchez, X. F. Sanchez-Romate, S. G. Prolongo, and A. Jiménez-Suárez, “Combining de-icing and self-healing for wind blades through an innovative multilayer coating approach,” Polym Compos, Apr. 2024, doi: 10.1002/PC.29252.

[35] C. Zeng, L. Liu, W. Bian, Y. Liu, and J. Leng, “4D printed electro-induced continuous carbon fiber reinforced shape memory polymer composites with excellent bending resistance,” Compos B Eng, vol. 194, p. 108034, Aug. 2020, doi: 10.1016/J.COMPOSITESB.2020.108034.

[36] Y. Ibrahim, R. Kempers, and A. Amirfazli, “3D printed electro-thermal anti-or de-icing system for composite panels,” Cold Reg Sci Technol, 2019, doi: 10.1016/j.coldregions.2019.102844.

[37] “EVANOHM ALLOY S Filing Code: Nickel Alloy.”

[38] A. Gleadall, “FullControl GCode Designer: Open-source software for unconstrained design in additive manufacturing,” Addit Manuf, vol. 46, p. 102109, Oct. 2021, doi: 10.1016/J.ADDMA.2021.102109.

[39] ASTM International, “Standard Test Method for Tensile Properties of Polymer Matrix Composite Materials,” Oct. 15, 2017, ASTM International, West Conshohocken, PA. doi: 10.1520/D3039_D3039M-17.

[40] E. Baharlou and J. Ma, “Effect of raster orientation on large-scale robotic 3D printing of short carbon fiber-reinforced PLA composites,” Additive Manufacturing Letters, vol. 13, p. 100276, Apr. 2025, doi: 10.1016/J.ADDLET.2025.100276.

[41] U. K. Komal, A. H. Siddiqui, and A. Tewari, “Investigation of the structural performance and failure mechanisms of 3D printed continuous carbon fiber-based composites,” Polym Compos, vol. 46, no. 9, pp. 8597–8613, Jun. 2025, doi: 10.1002/PC.29512.

[42] S. S. Kumar, J. S. Akmal, and M. Salmi, “4D printing of shape memory polymer with continuous carbon fiber,” Progress in Additive Manufacturing, vol. 9, no. 6, pp. 1985–1995, Dec. 2023, doi: 10.1007/S40964-023-00553-1/TABLES/2.

[43] D. O. Adams and D. F. Adams, “Tabbing Guide for Composite Test Specimens,” Oct. 2002.

[44] S. Pahari and G. W. Melenka, “Analysis of the interface properties of multi-material fused filament fabricated (FFF) printed polymer composite structures,” Int J Adhes Adhes, vol. 142, p. 104074, Sep. 2025, doi: 10.1016/J.IJADHADH.2025.104074.

[45] C. Unlusoy and G. W. Melenka, “Flexural testing of cellulose fiber braided composites using three dimensional digital image correlation,” Compos Struct, vol. 230, p. 111538, Dec. 2019, doi: 10.1016/J.COMPSTRUCT.2019.111538.

[46] International Digital Image Correlation Society, E. M. C. Jones, and M. A. Iadicola, A Good Practices Guide for Digital Image Correlation. 2018. doi: https://doi.org/10.32720/idics/gpg.ed1/print.format.

Chapter 5 - Conclusion

5.1. Conclusions

This thesis aimed to determine the mechanical properties of 3D-printed continuous wire polymer composites (CWPCs) with decreased void volume fraction and with varying laminate layups. Previous work in 3D-printed CWPCs have significantly improved the strength and stiffness and allows for in-part sensing. However, literature shows significant void content in CWPC samples due to the nature of the 3D printing, and studies have mainly focused on unidirectional reinforcement. These gaps limit the application of composite materials. This work aimed to develop a consolidation procedure combining hot-pressing and resistive heating to determine the effectiveness void reduction can have on mechanical properties, and test multidirectional CWPC laminates for characterization for future use. A comprehensive literature review was done to cover the background on 3D printing, the traditional manufacturing of composite materials, and how the two fields can be applied together. This knowledge, along with an overview of different void reduction techniques was then applied to the studies that make up this thesis.

The first study aimed to develop a consolidation procedure to perform the void reduction on unidirectional 3D-printed CWPCs. A 3D printer with a custom single nozzle co-extrusion print head was used to manufacture CWPC samples with PLA as the matrix and nichrome as the reinforcement wire, with a 1.18% wire volume fraction (W_{vf}). The consolidation procedure applied hot-pressing with aluminum platens mounted to a universal testing machine and resistive heating of the internal reinforcement wire to reduce the void content in the samples. Samples printed with embedded T-type thermocouple wires were used to determine the accuracy of 1D transient conduction and resistive heating analytical models to predict the time required for

heating the sample to the glass transition temperature of the PLA matrix, allowing the PLA to be remolded. Microscope image analysis was performed on the cross-sections of unprocessed, hot-pressed, and consolidated samples and showed a 91.6% decrease in void volume fraction due to the full consolidation procedure, reducing the void volume fraction from 5.24% to 0.44%. This showed the value of the addition of the resistive heating in reducing the void volume fraction and increasing the adhesion between the PLA raster and the embedded reinforcement wire. Three-point flexural tests were conducted on all three sample types, and the flexural strength and modulus results were compared using one-way analysis of variance (ANOVA) statistical tests. The ANOVA showed that consolidation had a statistically significant improvement on the flexural properties. The flexural strength and flexural modulus were increased by 5% and 12%, respectively.

The second study aimed to characterize the mechanical properties of unidirectional and multidirectional CWPC laminates. UD-0°, UD-90°, and cross-ply samples with laminate codes $[0_5]$, $[90_5]$, $[90/0/\overline{90}]_S$, respectively, were 3D printed using the same printer and materials for tensile testing. Samples were consolidated in order to determine if the reduction of void content would affect the mechanical properties of the 3D-printed CWPC laminates. The samples experienced a progressive failure mode, where the PLA matrix cracked and failed first, with the reinforcement wires still carrying some load after matrix breakage. Digital image correlation was used to analyze the strain fields on the top side of the samples under loading. Non-consolidated UD-0°, UD-90°, and cross-ply samples showed ultimate tensile strengths of 65.95 MPa, 19.79 MPa, and 36.60 MPa, and elastic moduli of 4.96 GPa, 2.47 GPa, and 3.51 GPa, respectively. The consolidated counterparts of these samples showed ultimate tensile strengths of 67.58 MPa, 24.19 MPa, and 38.47 MPa and elastic moduli of 5.30 GPa, 2.87 GPa, and 3.67 GPa. Due to the

transverse wire reinforcement resulting in the PLA matrix carrying more of the load, UD-90° samples showed the largest increase in mechanical properties after consolidation because the consolidation procedure increased the bond between rasters. The apparent laminate stiffness was calculated using classical laminate plate theory (CLPT) and compared to the elastic moduli. All consolidated samples showed a closer elastic modulus to the apparent laminate stiffness, since CLPT assumes there is no void content. This along with microscope images of the cross-sections of each sample type helped to illustrate the consolidation procedure was effective in decreasing void content.

5.2. Future Work

The development and implementation of the consolidation procedure is one of the main highlights in this work. The samples in both studies were limited to wire volume fractions around 1% due to the configuration of the print head, which had a 1 mm diameter nozzle, which limited the wire diameter [1]. Alternative printing equipment, including larger, custom print heads and nozzles could provide the opportunity to experiment with larger wire diameters. If larger wire diameters can be chosen, this could increase the W_{vf}, which in turn increases the mechanical properties. The 3D printing of a CWPC with a larger wire diameter is likely to result in higher void content in the final product. If the W_{vf} could be increased significantly, for example show the difference between 1%, 5% and 10%, this could show the effectiveness of the consolidation procedure, potentially yielding an exponential increase in mechanical properties with void reduction in higher wire volume fraction samples.

Different material choices could be used as well to increase the use cases. PLA is a relatively low-strength 3D printing polymer. Engineering materials such as polyetheretherketone (PEEK),

or nylon have higher strength and stiffness, as well as higher glass transition temperatures (T_g). Resistive heating of the internal reinforcement material allows for uniform heating, which may prove useful for such materials. The reinforcement materials can be changed as well, since the main requirement for the samples to undergo the consolidation procedure is the reinforcement material should be electrically resistive, meaning it will heat up significantly when a current is applied. Therefore, a material such as copper may not be suitable, but nickel-chromium, stainless steel, carbon fibre, or glass fibre could be.

Finally, the implementation of consolidated multidirectional laminates for different applications can be studied. Some studies have shown promising work using unidirectional CWPCs for structural health monitoring [2], [3]. Consolidation of unidirectional or multidirectional CWPC laminates provides increased adhesion between the polymer matrix and the reinforcement wire, allowing for more accurate sensing measurements. In the case of wearable sensors, the CWPC is likely to experience some form of combined loading, which is why composite materials often consist of alternating lamina orientations to form the laminate, to reinforce composite panels in multiple directions. The use of multi directional laminates, such as the cross-plies printed in the second study of this work, or quasi-isotropic layup configurations, could improve the lifespan of CWPC wearable sensors.

5.3. References

[1] Y. Ibrahim, G. W. Melenka, and R. Kempers, “Additive manufacturing of Continuous Wire Polymer Composites,” Manuf Lett, vol. 16, pp. 49–51, Apr. 2018, doi: 10.1016/J.MFGLET.2018.04.001.

[2] M. A. Saleh, R. Kempers, and G. W. Melenka, “Fatigue behavior and electromechanical properties of additively manufactured continuous wire polymer composites for structural health monitoring,” Fatigue Fract Eng Mater Struct, vol. 45, no. 9, pp. 2630–2645, Sep. 2022, doi: 10.1111/ffe.13778.

[3] M. A. Saleh, R. Kempers, and G. W. Melenka, “A comparative study on the electromechanical properties of 3D-Printed rigid and flexible continuous wire polymer composites for structural health monitoring,” Sensors and Actuators A, vol. 328, p. 112764, 2021, doi: 10.1016/j.sna.2021.112764.

Appendix – Compaction Platen Design

A.1. Introduction

This appendix outlines the design process of the compaction setup, including the technical drawings and material choice for the platens, the setup for mounting the platens to the universal testing frame, and the working principles of the temperature controller.

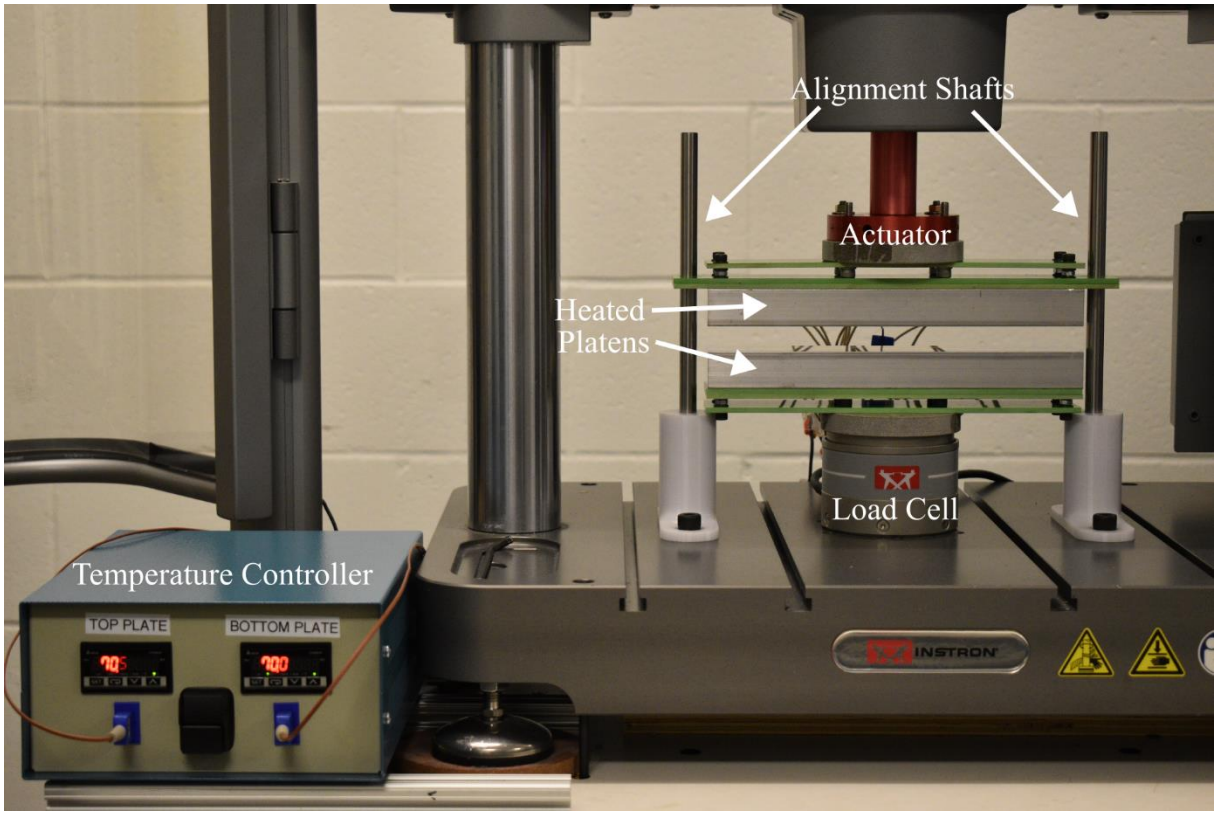

A.2. Platen Design

The platens were machined out of 6061 aluminum stock with dimensions 10 in. x 2 in. x 1 in. This was done to fit the dimensions of the test standard used (ASTM D3039).

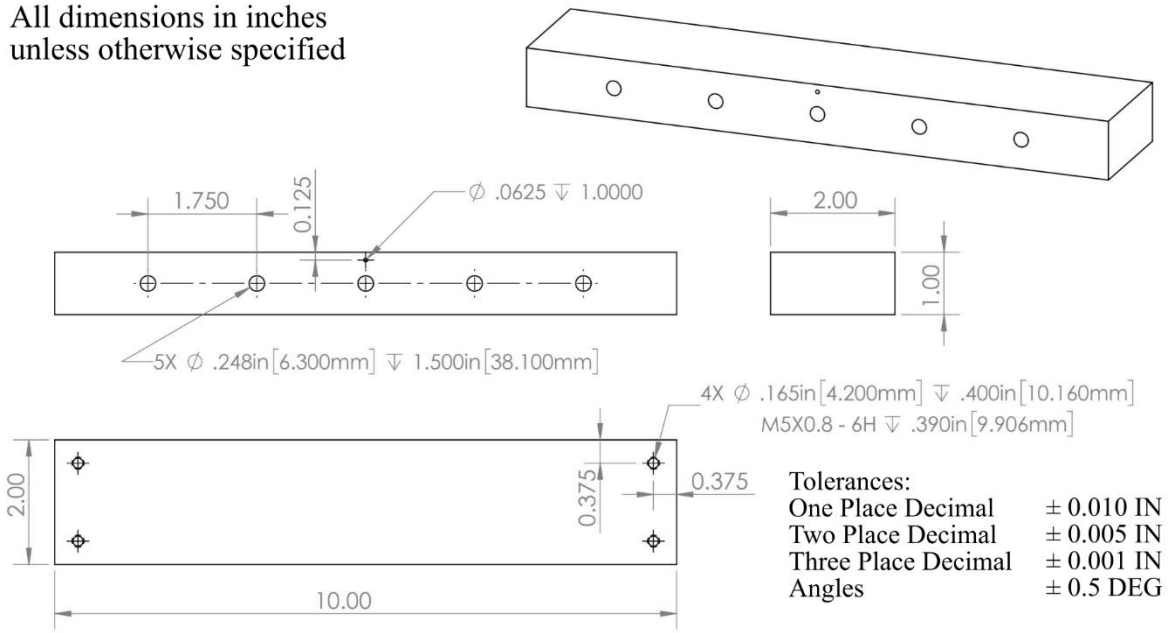

The holes for the five cartridge heaters used to evenly heat the platens were drilled evenly in the centre of the thickness of the Al platens. A hole for a 1/16 in. diameter T-type sheathed thermocouple was drilled 1 in. in depth through the width of the platen, 0.125 in. from the surface that would be in contact with the sample. This was done to provide reliable feedback to the PID temperature controllers to allow for the consistent temperature readings of the surface in contact with the sample to quickly account for any heat losses that may have occurred when the room temperature sample came in contact with the pre-heated platens.

A.3. Platen Alignment

To ensure the platens were aligned, 12 mm diameter, 250 mm long 1566 carbon steel linear shafts were press-fit in 3D-printed brackets, which were screwed to the universal test frame.

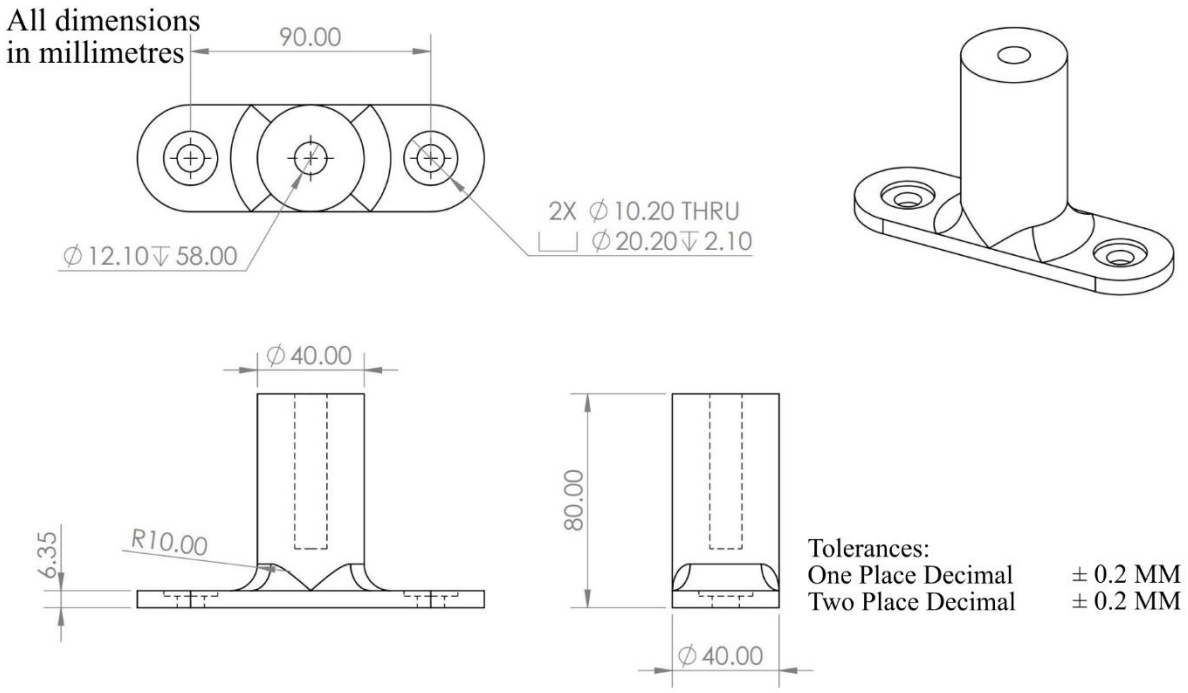

A.4. Platen Mounting Test Frame

To mount the platens to the universal testing machine (UTM), screws were used to mount 1/8” thick sheets of G10 garolite to actuator and load cell, then these pieces of garolite were fastened to the tapped holes on the corners of the platens. Garolite is an insulating material made of fibreglass, so it is used as a method of fastening the platen directly to the load cell and actuator while also providing the necessary temperature insulation between the heated platen and the UTM.

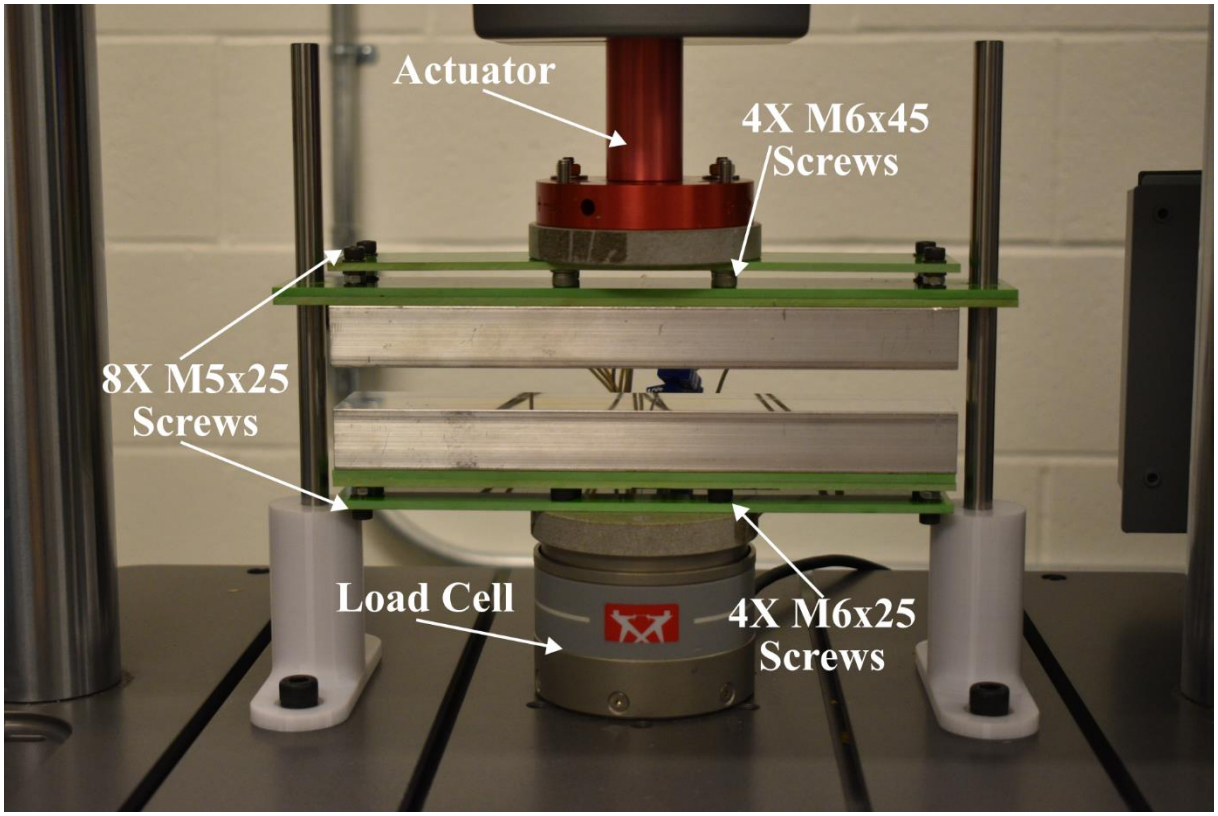

The first sheet of garolite is attached to the actuator and load cell using the M6 x 45 screws and M6 x 25 screws, respectively. The next two sheets of garolite are then used to screw the aluminum platens to the first garolite sheets using M5 x 25 screws. The full list of hardware can be seen below.

Fastener	Quantity
M5 x 25 Screw	8
M5 Washer	28
M5 Nut	8
M6 x 45 Screw	4
M6 x 25 Screw	4
M6 Washer	4
M6 Nut	2

A.5. PID Temperature Controller Parts List

Part Name	Quantity
Delta DTB 4824 RR Temperature Controller	2
ASR-SI480A25RY-LV Solid State Relay	2
Heat Sink/Thermal Pad for SSRs	2
Omega Engineering T-Type Thermocouple/Thermocouple Jacks	2
SPDT Rocker Switch	1
Fuse/Fuse Holder	1
20A Power Cable	1